Spring 5-15-2015

Interfacial Chemistry of Trace Elements at Mineral Surfaces in Engineered Water Systems

Lin Wang
Washington University in St. Louis

WASHINGTON UNIVERSITY IN ST. LOUIS

School of Engineering and Applied Science
Department of Energy, Environmental and Chemical Engineering

Dissertation Examination Committee:
Daniel E. Giammar, Chair
John D. Fortner, Co-Chair
Richard L. Axelbaum
Jeffrey G. Catalano
Phillip A. Skemer
Jay R. Turner

Interfacial Chemistry of Trace Elements at Mineral Surfaces in Engineered Water Systems

by

Lin Wang

A dissertation presented to the
Graduate School of Arts & Sciences
of Washington University in
partial fulfillment of the
requirements for the degree
of Doctor of Philosophy

May 2015
St. Louis, Missouri

Table of Contents

List of Figures

List of Tables

Acknowledgments

While writing these words, I am realizing that this is the easiest part of the entire thesis because these words flow naturally from my heart instead of my brain.

I am extremely thankful to both of my co-advisors, Dr. Daniel Giammar and Dr. John Fortner, for their constructive guidance, powerful motivation, and broad expertise. I am very fortunate to have received constant support and encouragement from two great mentors with complementary personalities and working styles. Their intellectual curiosity about the unknown and incessant dedication to high quality research have always been a source of inspiration to me. From them, I have learned the artistry of critical thinking and rigorous reasoning. Due to their leadership, I gained the benefits of working in two collaborative research groups. I remain indebted to both of my advisors because their mentorship has helped me become a better person.

I am appreciative of Dr. Jeff Catalano, Dr. Phil Skemer, Dr. Jay Turner and Dr. Richard Axelbaum for agreeing to serve on my thesis committee. Each of them, with expertise in their own field, has provided me with novel perspectives and insightful suggestions. I have benefited greatly from the individual and committee meetings with my committee members because their input helped me identify key research questions, tailor research approaches, and stay focused on the most critical objectives.

I could not have completed my work so smoothly without the assistance from a group of highly responsible and warm-hearted people. My sincere thanks go to Patty Wurm, Jennifer Houghton, Sanmathi Chavalmane, Paul Carpenter and Haesung Jung for their time in training me on and assisting me with the analytical instruments. I am appreciative of the great staff inside and outside our department: Tim McHugh for always providing solutions to my IT-related problems, Rose Baxter for her constant patience with my questions, and Beth Mehringer, Trisha

Sutton, and Lynn Zaltsman for making my graduate student life so much easier. Portions of my work were performed when I was a visiting student research collaborator in the Department of Civil and Environmental Engineering at Princeton University. I appreciate Dr. Catherine Peters, Dr. Jeffrey Fitts, Dr. Peter Jaffe and Dr. Satish Myneni for providing input on my research projects. I would also like to acknowledge Joseph Vocaturo, Lori Tunstall, John Higgins and Elizabeth Lundstrom for their assistance with my experiments and analyses.

Over the course of the past four years, I have increasingly realized the importance and benefits of working in a collaborative rather than competitive environment. I have had the fortune to do so, owing to a group of great colleagues. The Aquatic Chemistry Laboratory (ACL) is an enjoyable place to work and study, where I have grown from a novice to a competent researcher. The members in the group that were senior to me, including Yin Wang, Zimeng Wang and Fei Wang, all helped in leading me towards the right track of research. Vrajesh Mehta, a role model for me in both work and life, was always available and ready to assist me. Wei Xiong, Chao Pan, Zezhen Pan and Peng Liao, never hesitated to help me out. My special gratitude goes to Dr. Jose Cerrato, who not only gave me constructive advice on my research but also shared with me his insightful ideas about life. Jiewei Wu, Yi Jiang, Wenlu Li and Dr. Seung Soo Lee in Dr. John Fortner's group have also offered me tremendous help. I am very grateful to Begum Karakocak, a former visiting student and a current PhD student in our department, for collaborating with me to initiate my second project. Jessica Ray and Jake Meyer were more than willing to answer my questions whenever I had any. I also had the opportunity to work with two very bright and hardworking undergraduate students, Xiaochen Zuo and Scott Burns, who made important contribution to my projects. I enjoyed this mentoring experience very much because through them I saw myself growing and developing.

I am thankful for my caring and supportive friends that always stand by me regardless of the circumstances. I will always treasure the memory of growing up with like-minded friends, including Linjia Mu, Dongrui Li, Dongjin Cui and Yang Zhang. I will never forget the summer of 2010 when Lian He, Zhaobang Liu and myself flew half way around the world and settled down in St. Louis. I am indebted to the people who have served as my mentors in some way, such as Jiuqing Zhao, Xiao Dong, Xiao Sun, and Xiaolong Liu. I am grateful for Karen Davis, Kathy Orchen, and Amy Doll for hosting me in their house/apartment and providing me with the best living conditions possible. My thanks go to Le You, Yaping Zhang, Jia Luo, Guannan He, Ruiye Ni, Xiaonan Yu, Yuwen Wang, Hao Yang, Guoxi Xu, Jianqing Li, Liang Gao, Yu Wang, Chi Zhang and many, many others.

Thanks to my advisor Daniel Giammar, I had the chance to be a visiting student research collaborator at Princeton University in the academic year of 2012-2013. I cherished this rewarding experience because of the amazing people I got to know during that time. Bin Guo, Hang Deng, Qi Li, Ping Lu and Sili Deng have supported me through my ups and downs. Dan Li and Maofeng Liu were always ready to help me. My heartfelt gratitude goes to Peng Zhao, who inspired me to become a better and stronger person.

In addition to my research, I have had the privilege to work with a group of brilliant and enthusiastic student leaders on a variety of events and projects, including Maggie Majors, Junchen Gu, Shelina Remnarine, Ervin Malakaj, Nick Miller, Trung Tran, Mike De Wit and many others. I appreciate the mentorship from the Graduate School Associate Dean Elaine Berland and the Assistant Dean Kimberly Curtis. Learning from them, I have greatly broadened my horizons and improved my communication skills.

This work was supported by research funding from The International Center for Advanced Renewable Energy and Sustainability (I-CARES) and the McDonnell Academy Global Energy and Environmental Partnership (MAGEEP). Both organizations were established in the global context of sustainable development, and I am beholden for their financial support that allowed me to work on two interesting research projects.

Finally, I owe it all to my endearing parents who have loved me unconditionally and supported me unreservedly. My generation of only children in China has often become the target of criticism from the mass media. People may think that I don't have the "Little Emperor Syndrome", and I attribute it all to my parents that have shaped me into the person I am today. They have doted on me without spoiling me, disciplined me without controlling me, and advised me without pressurizing me. Because of their open-mindedness, I feel that my parents and I have grown up together, so in the years to come, I will care for them as they grow older the way they once did to raise me.

Lin Wang

Washington University in St. Louis

May 2015

Dedicated to my parents.

ABSTRACT OF THE DISSERTATION

Interfacial Chemistry of Trace Elements

at Mineral Surfaces in Engineered Water Systems

by

Lin Wang

Doctor of Philosophy in Energy, Environmental and Chemical Engineering

School of Engineering and Applied Science

Washington University in St. Louis, 2015

Professor Daniel Giammar, Chair

Professor John Fortner, Co-Chair

This thesis research consists of two independent research projects that both studied interfacial chemical processes affecting trace elements at mineral surfaces.

The objectives of Project 1 were to 1) quantify the impact of water chemistry on As(III) adsorption on lepidocrocite, 2) develop a surface complexation model to describe equilibrium As(III) and As(V) adsorption to lepidocrocite and 3) elucidate the mechanism of Fe(II)-mediated As(III) oxidation at the lepidocrocite-water interface. Arsenic is a regulated element that can be found at high concentrations in groundwater resources that are used as drinking water sources. Iron (oxyhydr)oxides are one of the most abundant groups of minerals in soils and aquifers, and their presence can significantly affect the behavior of arsenic. Iron (oxyhydr)oxides are also commonly used as adsorbents in engineered system to remove arsenic from drinking water. In addition to adsorbing arsenic, Fe(III) minerals can participate in As(III) oxidation to As(V), which can reduce arsenic's mobility and enhance its adsorption. Advances in the understanding

of the environmental chemistry of arsenic are important to the development of water treatment technologies.

The adsorption of arsenic to lepidocrocite strongly depends on water chemistry. Experiments that pursued objectives in Project 1 examined As(III) and As(V) adsorption to lepidocrocite as a function of pH, total As(III) concentration, iron loading, Fe(II) and competing adsorbate presence. For the arsenic concentrations and Fe loadings studied, As(V) adsorption decreases substantially with increasing pH, while As(III) adsorption is less sensitive to pH changes, characterized by a stable level of high adsorption between pH 6-9. For As(III), the presence of oxygen promoted the overall arsenic adsorption via partial As(III) oxidation. A surface complexation model, optimized for both adsorption isotherms and adsorption edges, was able to describe the adsorption of both As(III) and As(V) to lepidocrocite over a broad range of conditions.

The concentration and oxidation states of dissolved arsenic measured over the course of a reaction provided information on As(III) oxidation. When dissolved oxygen and Fe(II) were not present, As(III) was not oxidized by the Fe(III) in lepidocrocite. At both oxic and anoxic conditions, As(III) was oxidized to As(V) in systems that contained lepidocrocite together with Fe(II); this oxidation led to overall enhanced arsenic adsorption at near neutral pH. With oxygen, the pH-dependent generation of oxidants from the Fenton reaction drove the As(III) oxidation. In the absence of oxygen, the As(III) was probably oxidized by Fe(III) in lepidocrocite that had become more reactive upon reaction with Fe(II). The two reaction pathways could occur individually or in combination. Findings in Project 1 provide a deeper understanding of arsenic behavior in engineered water systems and are instrumental to manipulating the conditions under which arsenic is removed via adsorption.

The objectives of the second project were to 1) investigate the impact of water chemistry on trace element mobilization from shales during shale–fluid contact and 2) to identify the dominant mobilization pathways. The rapid development and expansion of hydraulic fracturing operations for enhanced energy recovery can affect water quality. The flowback and produced waters after injection of a fracking fluid could contain high total dissolved solids and trace elements mobilized from contact with shales. The concentrations of specific elements depend on the geochemistry of the formation, fluid composition, and time of shale–fluid contact. An understanding of shale-bound element mobilization will facilitate wastewater management associated with hydraulic fracturing practices.

Experiments in Project 2 were performed to evaluate trace element mobilization from shales over a range of fluid chemistries with core samples from the Eagle Ford and Bakken formations that are currently producing natural gas and oil via hydraulic fracturing. Samples were characterized with regard to their mineralogy, surface area and total carbon prior to experiments. The fluid chemistry was varied in pH, oxidant level, solid:water ratio, and temperature. Analytical results from experiments and chemical equilibrium modeling were integrated to identify dominant mobilization pathways.

The Eagle Ford samples used in this research were rich in carbonates and quartz with minor amounts of kaolinite, albite, pyrite and 5 wt % total organic carbon. The release of most elements strongly depended on pH, which was primarily controlled by carbonate dissolution. The introduction of oxygen and other oxidants (H_2O_2) significantly increased the amount of sulfate over time; the sulfate generated had a direct impact on Ba concentrations due to the formation of $BaSO_4$ as a secondary phase. For these Eagle Ford samples, trace elements (such as As and U) mobilized from rock-fluid contact had low concentrations in all the conditions studied.

Major mineral phases in the Bakken Formation samples included quartz, K-feldspar, illite, dolomite and pyrite. One sample with 18.7 wt % total organic carbon was naturally enriched in redox-sensitive trace elements (including regulated elements such as As and U). For all the water chemistry variables studied (pH, oxidant level, solid:water ratio, temperature, salinity and chemical additive presence), pH and the oxidant level were properties that dominated the behavior of most elements. The addition of chemical additives (HCl, citrate, and persulfate) affected element release mainly by altering system pH or redox conditions. The abundance of dolomite relative to pyrite determined the system pH when sufficient oxidants (such as oxygen and oxidizing chemical additives) were present. The lack of acid-neutralizing minerals, in case of sulfide mineral oxidation, may lead to a significant decrease in the pH. The knowledge gained in Project 2 provides insight on the key factors that dominant shale-bound element mobilization during rock-fluid interactions, and is helpful for understanding and managing produced and flowback water related issues associated with hydraulic fracturing.

Chapter 1: Introduction

1.1 Background and Motivation

This thesis consists of two independent research projects focusing on 1) interfacial chemistry between As(III) and lepidocrocite and 2) trace element mobilization during shale-fluid contact. Although distinct in their backgrounds, contexts, and funding sources, both projects are focused on similar interfacial chemical reactions and processes (such as adsorption and redox reactions).

The adsorption and redox transformation of arsenic at iron mineral surfaces may govern the distribution, mobility and fate of arsenic in natural and engineered systems. The interactions between arsenic and iron (oxyhydr)oxides are instrumental for arsenic removal with iron-based solids, in both concentrated water treatment facilities and point-of-use purification devices. Adsorption and redox reactions also affect the behavior of trace elements at shale-fluid interfaces for hydraulically fractured gas and oil production wells. Organic-rich shales are naturally enriched in redox sensitive elements. The introduction of oxygen and other oxidizing additives during hydraulic fracturing may mobilize elements that are more soluble in oxidative forms. The change of pH and presence of complexing agents in a fracturing fluid may also affect mineral dissolution and even adsorption properties of elements.

1.1.1 Project 1: Interfacial Chemistry Between As(III) and Lepidocrocite

Arsenic in Water

Arsenic is a toxic element that can be found at high concentrations in natural waters (Smedley and Kinniburgh, 2002). Sources of arsenic in aquatic systems are primarily natural soil

and rocks while human activities can influence hydrogeochemistry in ways that increase concentrations (Ferguson and Gavis, 1972; Harvey et al., 2006). The maximum contaminant level in the United States (U.S. EPA, 2009) and WHO guideline value (WHO, 2011) for arsenic in drinking water are both 10 μg/L. However, in some parts of south Asia, arsenic concentrations in groundwater can reach as high as 3000 μg/L and pose a severe threat to drinking water safety and public health (Chowdhury et al., 2000; Berg et al., 2001; Kinniburgh and Smedley, 2001; Fendorf et al., 2010; Kim et al., 2011; Jain and Singh, 2012).

Arsenic speciation in water is primarily governed by redox potential (pe) and pH (Figure 1.1). The most common forms of arsenic in water are inorganic oxyanions of As(III) and As(V), which can respectively be referred to as arsenite and arsenate (Jain and Ali, 2000). At circumneutral conditions, As(V) exists primarily as ionic forms ($H_2AsO_4^-$ and $HAsO_4^{2-}$), while As(III) exists predominantly as the neutral molecular form (H_3AsO_3), and thus is generally considered more mobile than As(V).

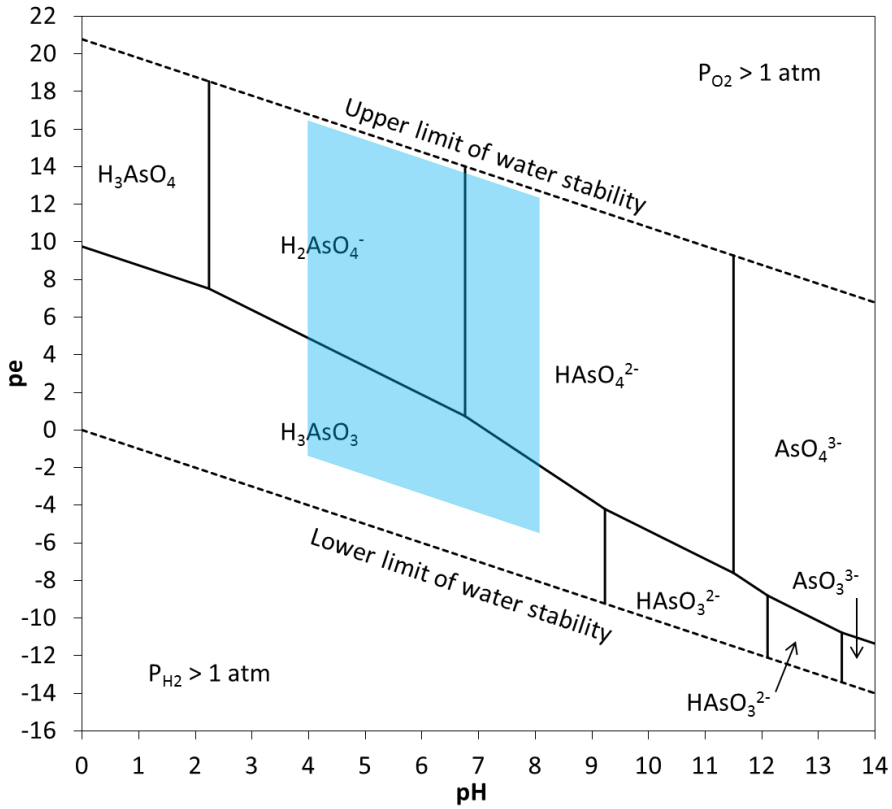

Figure 1.1 pe-pH diagram for predominant arsenic species in water at 25 ℃ and 1 bar total pressure with 10^{-6} M (75 μg/L) total arsenic concentration [adapted from (Cherry et al., 1979)]. The blue shaded area indicates the range of most natural waters.

Interaction between Arsenic and Iron (oxyhydr)oxides

Iron (oxyhydr)oxides are one of the most abundant minerals in natural systems and can strongly influence the fate and transport of arsenic (Cornell and Schwertmann, 2003). The adsorption and desorption of arsenic to iron (oxyhydr)oxides present in aquifers can often control the mobility of arsenic in natural waters (Ferguson and Gavis, 1972; Fendorf et al., 2010). Iron (oxyhydr)oxides are also effective chemicals that are widely used in engineered systems to remove both As(III) and As(V) from drinking water (Jekel, 1994; Hering et al., 1997; Fields et al., 2000; Mohan and Pittman, 2007; Balasubramanian et al., 2009; Neumann et al., 2013; Wenk et al., 2014). The association of arsenic with iron (oxyhydr)oxides is strongly affected by

water chemistry. The adsorption of As(V) substantially decreases with increasing pH (Jönsson and Sherman, 2008; Wan et al., 2011) and is influenced by competitive adsorption with other groundwater solutes (Wilkie and Hering, 1996; Zeng et al., 2008). While As(III) adsorption is less pH-dependent and generally weaker than As(V), it can still be affected by competing adsorbates (Wilkie and Hering, 1996; Dixit and Hering, 2003).

A surface complexation model is a research tool for interpreting and predicting adsorption at solid-water interfaces. The surface of the solid is assumed to consist of specific functional groups that react with dissolved solutes to form surface complexes. The equilibrium of surface complexation and ionization can be described via mass balance equations with correlation for variable electrostatic conditions (Davis and Kent, 1990). Surface complexation modeling (SCM) can often provide a good prediction of both As(III) and As(V) adsorption under varied conditions with regard to total arsenic concentration, type of iron oxide adsorbents, and the presence of competitive adsorbates (Wilkie and Hering, 1996; Manning et al., 1998; Gao and Mucci, 2001; Dixit and Hering, 2003; Fukushi and Sverjensky, 2007; Kanematsu et al., 2013).

Iron (oxyhydr)oxides can also participate in the oxidation of As(III) to As(V), which can potentially affect arsenic mobility and toxicity. Ferrihydrite was found to catalyze As(III) oxidation by oxygen on a time scale of several days to a week (Zhao et al., 2011). Photoinduced oxidation of As(III) was observed in the presence of goethite and ferrihydrite, and the iron(III) oxides were found to be oxidants in both cases (Bhandari et al., 2011; Bhandari et al., 2012). In addition, the oxidation of As(III) mediated by ferrous iron was observed in the co-presence of Fe(II) and Fe(III) (oxyhydr)oxides (Bisceglia et al., 2005; Ona-Nguema et al., 2010). Dissolved oxygen and soluble intermediates involved in Fe(II) oxidation may act as rate-enhancing species

in As(III) oxidation (Sahai et al., 2007). Previous studies have proposed pH-dependent generation of oxidants in Fenton reaction, where reactive oxygen species are produced at low pH while a less reactive but more selective oxidant [most likely Fe(IV)] forms at circumneutral pH (Hug and Leupin, 2003; Katsoyiannis et al., 2008). Further, an Fe(II)-activated Fe(III) intermediate species was also suggested to induce redox transformation of arsenic in strictly anoxic conditions (Amstaetter et al., 2010).

Motivation

This project was motivated by several knowledge gaps regarding arsenic behavior at lepidocrocite-water interfaces. Lepidocrocite is a common iron oxyhydroxide found in soils that actively participates in iron redox cycling (Cornell and Schwertmann, 2003). It is also the dominant product of iron electrocoagulation, which is an effective treatment technique to remove arsenic from water (Ratna Kumar et al., 2004; Parga et al., 2005; Gomes et al., 2007; Thella et al., 2008; Balasubramanian et al., 2009; Lakshmanan et al., 2010; Wan et al., 2011; Li et al., 2012; van Genuchten et al., 2012). While previous research has found lepidocrocite to be a strong adsorbent for As(V) (Wan et al., 2011), little was known about its potential for As(III) adsorption. Further, no surface complexation model had been developed to understand the interaction between arsenic and lepidocrocite although surface complexation modeling is widely used to describe arsenic adsorption to other iron (oxyhydr)oxides. Despite the potential importance of Fe(II)-mediated As(III) oxidation to groundwater systems and water treatment, the reaction mechanisms remained poorly understood. This project, with the focus on the chemical processes at the lepidocrocite-water interface, sought to fill these knowledge gaps, providing a deeper understanding of the environmental chemistry of arsenic that is critical to contaminant management and water treatment.

1.1.2 Project 2: Trace Element Mobilization during Shale-fluid Contact

Shale Oil and Shale Gas

Shale oil and shale gas considered as unconventional hydrocarbon resources that are essentially trapped within shale formations due to low permeability. This is in contrast to conventional natural gas and oil sources that generally exist in discrete, well-defined, permeable subsurface reservoirs (Moniz et al., 2010). Recent advances in energy recovery technologies, especially from low-porosity shale formations have substantially increased global estimates for recoverable natural gas and crude oil reserves (U.S. EIA, 2013). The United States has led the development of such technologies and thus shale oil and gas resources to date. Shale gas is predicted to be the largest contributor in the projected 56% increase of U.S. natural gas production from 2012 to 2040, growing from 9.7 tcf (trillion cubic feet) in 2012 to 19.8 tcf in 2040 (U.S. EIA, 2014). Inclusion of shale gas and shale oil accounts for a 38% and 35% increase in the U.S. natural gas and crude oil resources, respectively (U.S. EIA, 2013). Figure 1.2 is a map displaying major U.S. shale gas and shale oil plays as of May 2011.

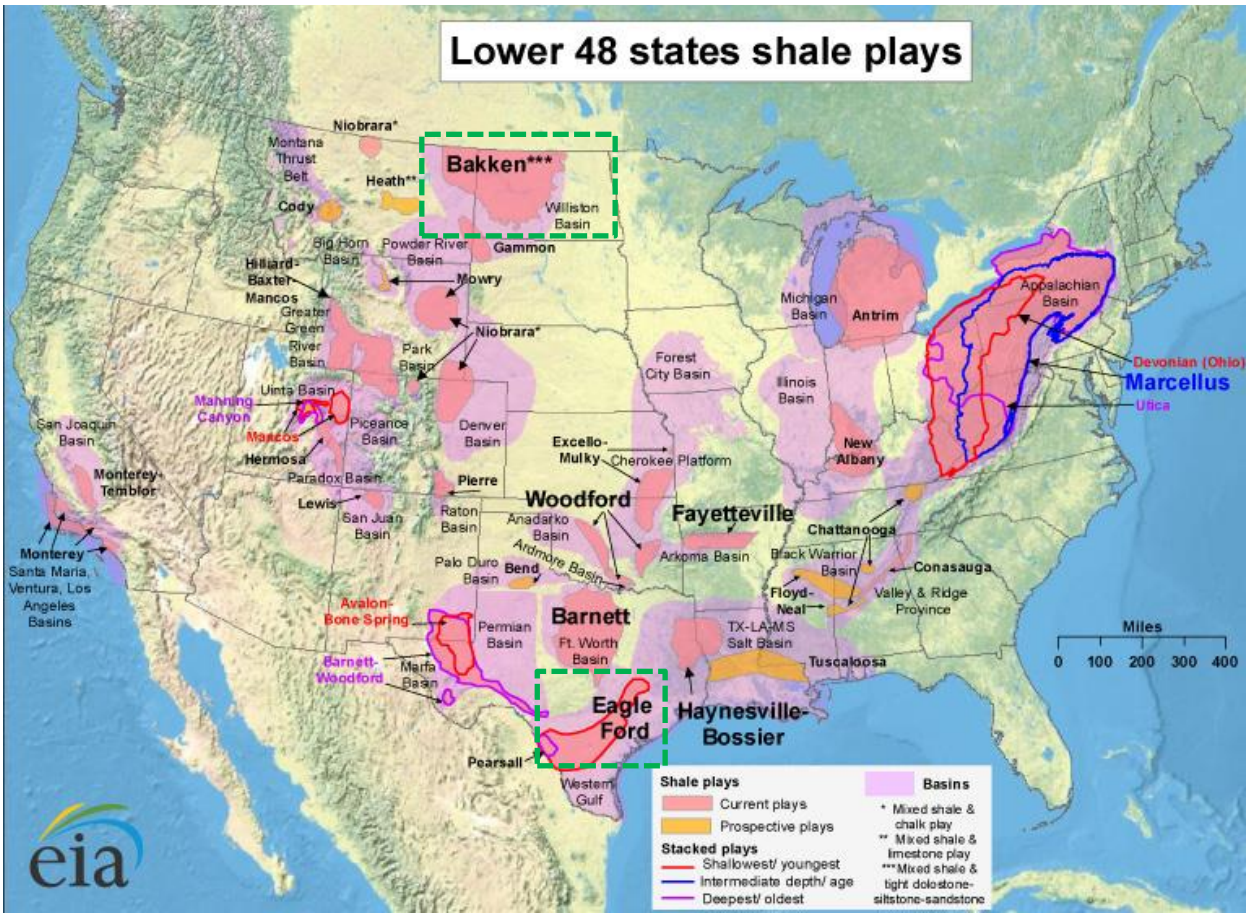

Figure 1.2 Map of U.S. shale gas and shale oil plays (U.S. EIA, 2011) with Eagle Ford Formation and Bakken Formation highlighted

Hydraulic Fracturing

Hydraulic fracturing is a well stimulation technique for enhanced hydrocarbon recovery. During the hydrofracking process (Figure 1.3), an engineered fluid mixture of water, proppants and chemical additives is injected into a horizontal well under high pressure to initiate small cracks in the shale formation (Ely, 1985). The induced fractures can then act as conduits in the rock formation,allowing for natural gas to flow more freely from the shale pores to the production well and surface (Arthur et al., 2009).

The fluid that returns to the surface after the pumping pressure is released is referred to as flowback or produced water and can contain both fracturing fluid and natural formation water.

There is no strict definitional boundary between flowback and produced waters, however, flowback waters are commonly considered to be fluids that flow out of a well within the first 2 weeks after stimulation by fracturing, whereas produced waters are the remaining fluid that flows from the well after the initial 2-week period (Haluszczak et al., 2013).

A number of water management issues are associated with hydraulic fracturing (Vidic et al., 2013; Vengosh et al., 2014). The first is the withdrawal of water required for well completion. Drilling of the vertical and horizontal components of a well may require 400–4000 m^3 (0.1 – 1 million gallons), and then 7000–18,000 m^3 (2 – 5 million gallons) of water are typically needed for hydraulic fracturing of each well (Nicot and Scanlon, 2012; Scanlon et al., 2014). The water utilized for hydraulic fracturing is represents a consumptive use because it leads to the loss of water from the source from which it was withdrawn. A second issue is the management of flowback and produced water, which can contain total dissolved solids as high as 200,000 mg/L (Hayes, 2009; Blondes et al., 2014). Wastewater containing such high dissolved solids can be challenging for fluid treatment and reuse. Much of the research to date on flowback water quality has focused on the Marcellus shale, where constituents of concern include bromide (risk of disinfection byproducts generation), barium, and naturally occurring radioactive materials such as Radium (Wilson and VanBriesen, 2012; Haluszczak et al., 2013).

The most common management options for flowback and produced waters from oil and gas production in the United States are reuse (requiring little treatment), recycle (with more involved treatment) and disposal via deep well injection (Nicot et al., 2014). Disposal approaches vary by play, depending on the quantity and quality of the wastewater, as well as the availability of treatment facilities and injection wells (Benko and Drewes, 2008). Transporting to centralized facilities for treatment and reuse is common in the Marcellus region (Wilson and VanBriesen,

2012) while deep injection wells are preferred management strategies in the Eagle Ford and Bakken formations (Stephen et al., 2010; Nicot et al., 2014).

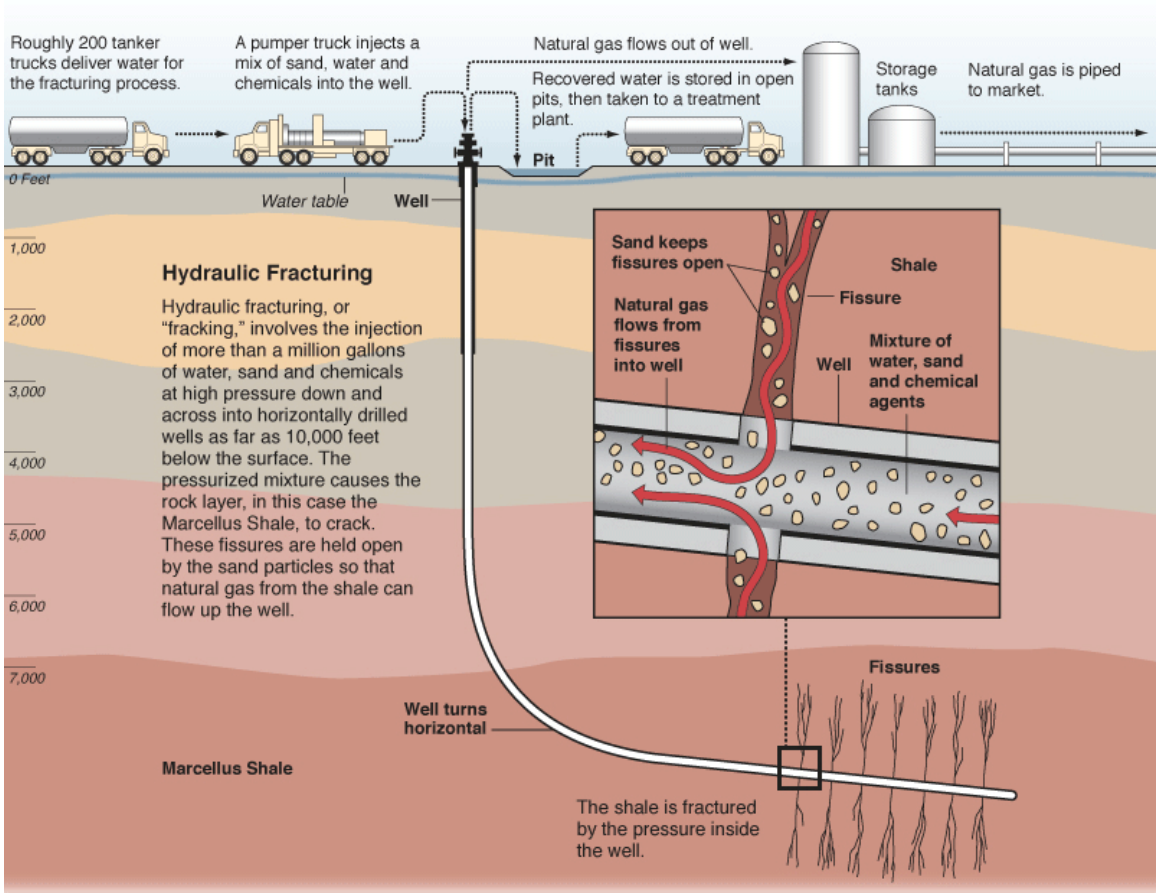

Figure 1.3 Illustration of a horizontal well showing the water lifecycle and natural gas flow during hydraulic fracturing (Schmidt, 2008)

Hydraulic Fracturing Fluids

The fracturing fluids used for shale stimulation primarily consist of water but also include a variety of chemical additives, depending on the specific conditions of the well to be fractured (properties of shale formation and associated water characteristics) (King, 2012). A typical fracture fluid carries 3 – 12 additives, each serving a different engineered purpose (Montgomery, 2013). A summary of some additives in a hydraulic fracturing fluid, their typical compounds and the reason the additive is used is provided in Table 1.1. Typically, hydrochloric acid (HCl) is the

single largest liquid component used in a fracturing fluid aside from water, and it is added to dissolve acid-soluble minerals in shales and to initiate cracks. EDTA and citrate used for iron control are both complexing agents that can bind strongly with metals [Mn(II), Cu(II), Fe(III), Pb (II) and Co(III)] (Huang et al., 1995).

Table 1.1 Volumetric composition and purposes of typical constituents of hydraulic fracturing fluid (Gregory et al., 2011)

Additive type	Volume fraction (%)	Example	Purpose
Water and sand	99.5	Sand suspension	"Proppant" sand grains hold microfractures open
Acid	0.123	Hydrochloric or muriatic acid	Dissolves minerals and initiates cracks in the rock
Fraction reducer	0.088	Polyacrylamide or mineral oil	Minimizes friction between the fluid and the pipe
Surfactant	0.085	Isopropanol	Increases the viscosity of the fracture fluid
Salt	0.06	Potassium chloride	Creates a brine carrier fluid
Scale inhibitor	0.043	Ethylene glycol	Prevents scale deposits in pipes
pH adjusting agent	0.011	Sodium or potassium carbonate	Maintains effectiveness of chemical additives
Iron control	0.004	Citric acid or EDTA	Prevents precipitation of metal oxides
Corrosion inhibitor	0.002	n,n-dimethyl formamide	Prevents pipe corrosion
Biocide	0.001	Glutaraldehyde	Minimizes growth of bacteria that produce corrosive and toxic by-products
Breaker	-	Ammonium persulfate	Allows a delayed break down of the gel polymer chains

Element Mobilization

Shale–fluid interactions have the potential to mobilize shale-bound metals (including regulated elements) through a variety of chemical reaction pathways (Figure 1.4). Dissolution of acid-reactive minerals (e.g. carbonates) can release trace elements hosted within them when acid (e.g. HCl) is used to initiate fractures. Metals originally attached (sorbed) to primary minerals are

likely to desorb due to changes in pH or the introduction of complexing agents (e.g. citrate). While shale formations are typically anaerobic, the oxygen in fracturing fluid and other oxidative additives (e.g. ammonium persulfate in Table 1.1) may trigger oxidative dissolution of trace elements that are more soluble under oxic conditions (such as uranium and chromium).

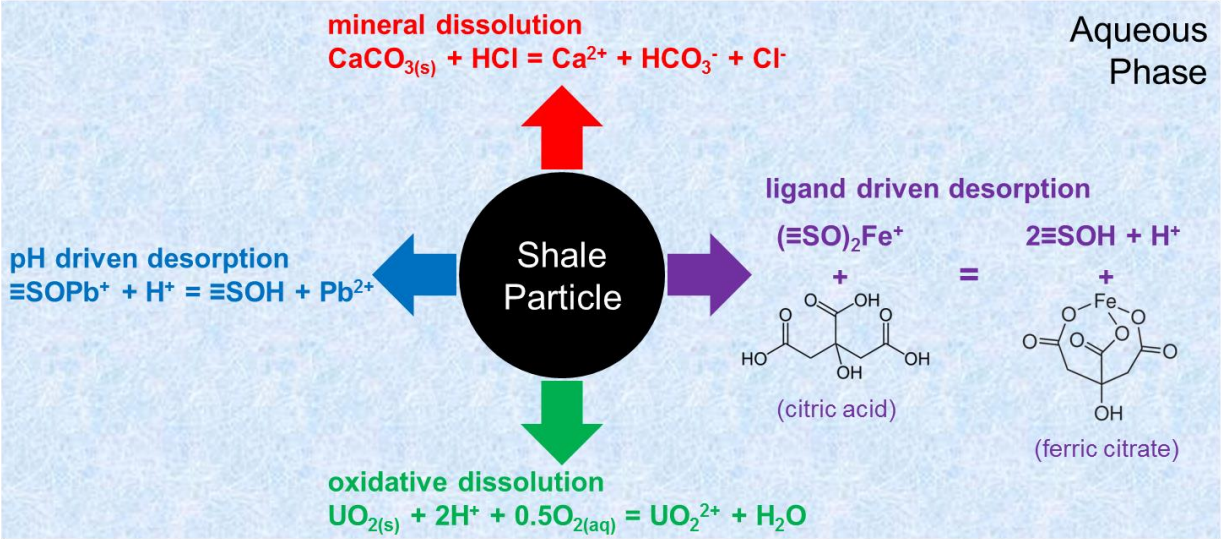

Figure 1.4 Illustration of possible chemical pathways of element mobilization from shales during shale-fluid interaction.

Eagle Ford Formation and Bakken Formation

The Eagle Ford shale gas and oil play is located within the Texas Maverick Basin (Figure 1.2). The play contains a high liquid component, leading to definition of three zones: an oil zone, a condensate zone and a dry gas zone, with an estimated 3.4 billion barrels of technically recoverable oil and 20.8 trillion cubic feet of technically recoverable natural gas (U.S. EIA, 2011).

The Bakken shale oil play is located within the Williston Basin in Montana and North Dakota (Figure 1.2) and extends into the Canadian provinces of Manitoba and Saskatchewan (U.S. EIA, 2011). Based on the most USGS assessment, this shale play together with the Three Fork Formation (right below Bakken Formation), contains a mean undiscovered, technically

recoverable volume of 7.4 billion barrels of oil, 6.7 trillion cubic feet of associated/dissolved natural gas, and 0.53 billion barrels of natural gas liquids. This estimate for shale oil reserve would be the largest finding in U.S history (USGS, 2013).

Motivation

Advances in understanding the composition of flowback and produced waters during hydraulic fracturing processes are critical for the associated wastewater treatment and management. Despite the potential effects of flowback constituents, little has been reported about the extent or pathway of shale-bound element release from shale-fracturing fluid contact. Such information is critical for managing potential waste streams that contain elements mobilized from the fractured rock. Knowledge obtained from bench-scale experiments is also important in evaluating possible chemical reaction kinetics and mechanisms in geological formations similar to the Eagle Ford and Bakken formations.

1.2 Research Objectives

1.2.1 Project 1 Objectives

The three main objectives associated with Project 1 are to

1) quantify the impact of water chemistry on As(III) adsorption to lepidocrocite
2) develop a surface complexation model to describe equilibrium As(III) and As(V) adsorption to lepidocrocite
3) elucidate the mechanism of Fe(II)-mediated As(III) oxidation at the lepidocrocite-water interface.

The degree of arsenic adsorption to lepidocrocite is subject to a variety of water chemistry properties, such as pH, As/Fe ratio, and dissolved oxygen level. Experiments pursued

objective 1 by evaluating arsenic adsorption over a wide range of conditions to enable the identification of the most important factor. A surface complexation model was then developed to facilitate the understanding of the adsorption mechanism and predict the behavior of arsenic in other conditions than those examined in this project. Finally, a system with co-occurrence of Fe(II) and Fe(III) solids was explored, further advancing the understanding of chemical interactions between arsenic and Fe(II)/lepidocrocite, which is common in both natural waters and engineered systems.

1.2.2 Project 2 Objectives

The two main research objectives for Project 2 were to:

1) investigate the impact of water chemistry on trace element mobilization from shales
2) identify the dominant mobilization pathways.

Observations and measurements based on laboratory experiments were able to provide information necessary in accomplishing Objective 1. However, the interpretation of these results would depend on how to correlate mobilization data with actual sample geochemistry and fluid properties. Objective 2 sought to identify the most important reaction pathways that govern the potential element release, which is helpful to evaluate shale-bound release from formations with similar geochemical properties.

1.3 Research Approach and Overview of Dissertation

The overall research approach for this dissertation is divided into two main tasks with each task corresponding to one of the two research projects.

The primary goal of Task 1 is to investigate chemical reactions at the lepidocrocite surface that influence the mobility, speciation, and solid-water distribution of arsenic. This task

is further divided into two research subtasks: Subtask 1A) the impact of water chemistry on As(III) and As(V) adsorption onto lepidocrocite and Subtask 1B) the mechanism of Fe(II)-mediated As(III) oxidation. Batch experiments were designed to measure As(III) removal from water and to examine the interfacial chemistry between As(III) and lepidocrocite.

Subtask 1A involved a set of batch experiments to examine As(III) to lepidocrocite as a function of pH, total arsenic concentration, iron loading, and competing adsorbate presence. The data on As(V) adsorption to lepidocrocite were obtained from previous experiments performed by a colleague. A surface complexation model was developed and optimized to describe the adsorption of both As(III) and As(V) to lepidocrocite over a broad range of conditions. Subtask 1B included additional experiments performed to study the potential oxidation of As(III) with dissolved Fe(II) and to investigate the reaction mechanism when oxidation does occur. Fe(II)-mediated As(III) oxidation at the lepidocrocite surface was studied at both oxic and anoxic conditions. Chapter 2 summarizes the results from Task 1 and specifically focuses on the effect of pH, As/Fe ratio, dissolved oxygen, and Fe(II) on the adsorption of arsenic to lepidocrocite. The impact of phosphate as a competing adsorbate is described in Appendix A. To account for the enhanced arsenic adsorption with 2-propanol (as a radical scavenger) observed in Chapter 2, the effect of 2-propanol on the colloidal stability of lepidocrocite is discussed in Appendix B.

Task 2 was designed to examine the rates and extents of trace metal mobilization from shales during shale-fluid interactions as a function of fluid property. It involved a set of batch experiments to evaluate the impact of water chemistry on shale-bound trace element mobilization. The fluid was varied with regard to pH, redox condition, solid:water ratio, temperature, salt concentration, and chemical additive presence. The interpretation of aqueous

analyses was combined with chemical equilibrium and reaction pathway modeling to identify dominant mobilization pathways.

Task 2 consisted of two subtasks that investigated core samples from the Eagle Ford formation (Subtask 2A) and the Bakken formation (Subtask 2B). These samples were characterized with regard to their mineralogy, elemental composition, specific surface area and total carbon. In batch experiments, the samples were exposed to a variety of fluid properties followed by a series of aqueous measurements for metals and metalloids, anions, dissolved organic carbon, and electrical conductivity. Chapters 3 and 4 describe the element mobilization results from Eagle Ford samples and Bakken shale samples, respectively.

Chapter 5 summarizes the results of the present work. Key observations and important environmental implications are highlighted and areas for future work are identified.

Chapter 2: Effects of pH, Dissolved Oxygen, and Aqueous Fe(II) on the Adsorption of Arsenic to Lepidocrocite

Results of this chapter have been submitted to the *Journal of Colloid and Interface Science* for review.

Graphical Abstract

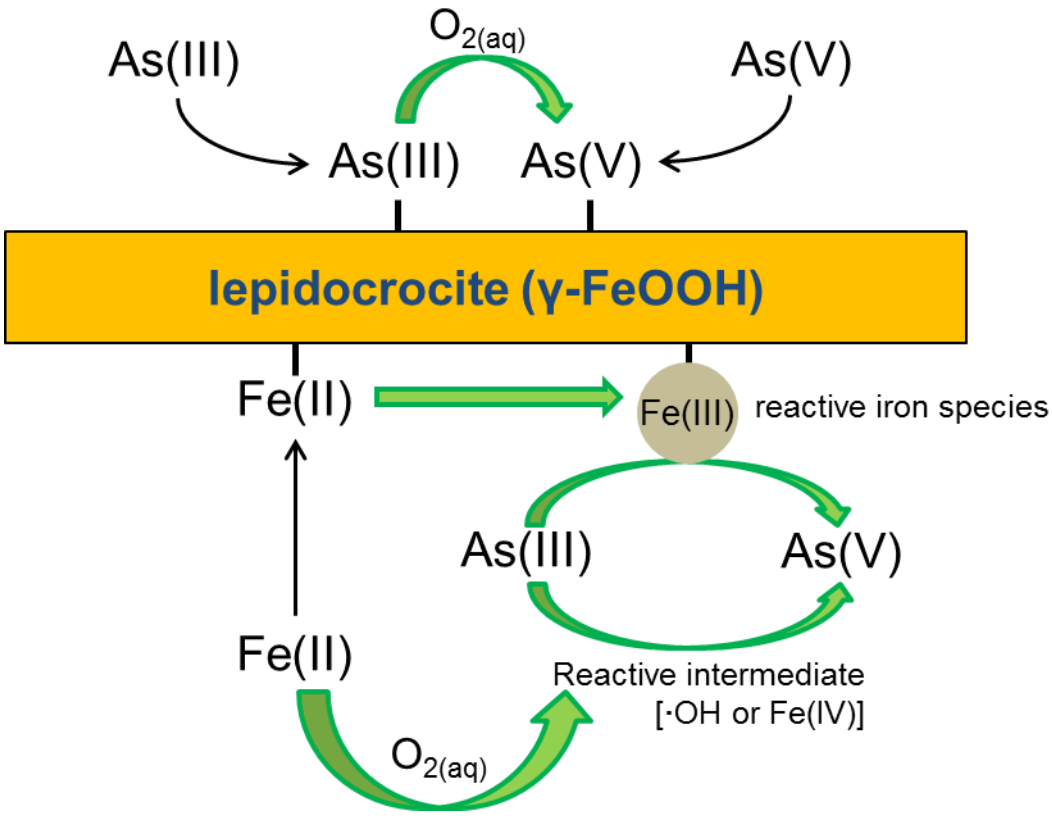

Abstract

The adsorption of arsenic to iron oxyhydroxides strongly depends on water chemistry. Iron(III) oxyhydroxides can also participate in the oxidation of As(III) to As(V), which changes arsenic's toxicity and adsorption behavior. As(III) and As(V) adsorption to lepidocrocite (γ-FeOOH) were examined in batch experiments that explored the effects of lepidocrocite dose, pH, availability of dissolved oxygen, and the presence of aqueous Fe(II) on adsorption. Lepidocrocite is an iron oxyhydroxide found in soils, and it is one of the major products of iron electrocoagulation for water treatment. A surface complexation model was able to describe the adsorption of both As(III) and As(V) to lepidocrocite over a broad range of conditions. The concentration and oxidation states of arsenic in solution were measured over the course of the reactions. At both oxic and anoxic conditions, As(III) was oxidized to As(V) in systems that contained lepidocrocite together with Fe(II); this oxidation led to overall enhanced arsenic adsorption at near neutral pH. With oxygen the pH-dependent generation of oxidants from the Fenton reaction drove the As(III) oxidation. In the absence of oxygen the As(III) was probably oxidized by Fe(III) in lepidocrocite that had become more reactive upon reaction with Fe(II).

Keywords: Arsenic Adsorption, Electrocoagulation, Surface Complexation Modeling, Fe(II)-mediated Arsenic Oxidation

2.1 Introduction

Arsenic is a toxic element that can be found at high concentrations in natural waters (Smedley and Kinniburgh, 2002). Sources of arsenic in aquatic systems are primarily natural soil and rocks, while human activities can influence hydrogeochemistry in ways that increase concentrations (Harvey et al., 2006). The most common forms are inorganic oxyanions of trivalent As(III) and pentavalent As(V) (Smedley and Kinniburgh, 2002). At circumneutral conditions, As(V) exists primarily as ionic forms ($H_2AsO_4^-$ and $HAsO_4^{2-}$), while As(III) exists predominantly as the neutral molecular form H_3AsO_3 . The maximum contaminant level for arsenic in US drinking water is 10 µg/L (0.13 µM).

Iron (oxyhydr)oxides are used in engineered systems to remove both As(III) and As(V) from drinking water by adsorption (Jekel, 1994; Hering et al., 1997; Fields et al., 2000; Mohan and Pittman, 2007; Balasubramanian et al., 2009). Water treatment can involve loading iron (oxyhydr)oxides into packed columns (Zeng et al., 2008), optimizing pH for adsorption to iron (oxyhydr)oxides formed during chemical coagulation (Hering et al., 1997; Han et al., 2002; Wickramasinghe et al., 2004), and producing iron (oxyhydr)oxides during electrocoagulation (Ratna Kumar et al., 2004; Parga et al., 2005; Thella et al., 2008; Wan et al., 2011; Li et al., 2012). The association of arsenic with iron (oxyhydr)oxides is strongly affected by water chemistry. The adsorption of As(V) substantially decreases with increasing pH (Wilkie and Hering, 1996; Jönsson and Sherman, 2008; Wan et al., 2011) and is influenced by competitive adsorption with other groundwater solutes such as silica and phosphate (Zeng et al., 2007; Kanematsu et al., 2013). While As(III) adsorption is less pH-dependent and generally weaker than that of As(V), it can still be affected by competing adsorbates (Kanematsu et al., 2013).

Surface complexation modeling (SCM) has been used to predict both As(III) and As(V) adsorption over a broad range of total arsenic, iron oxide type, and competitive adsorbate conditions (Dixit and Hering, 2003; Fukushi and Sverjensky, 2007; Zeng et al., 2007; Kanematsu et al., 2013). In a surface complexation model, the surface of the solid is treated as specific functional groups that react with dissolved solutes to form surface complexes. The equilibrium of surface complexation and ionization can be described via mass action equations with adjustments for variable electrostatic conditions (Davis and Kent, 1990). While previous studies have demonstrated the use of surface complexation models to simulate As(III) and As(V) adsorption onto different iron (oxyhydr)oxides (Wilkie and Hering, 1996; Dixit and Hering, 2003; Fukushi and Sverjensky, 2007; Zeng et al., 2007; Kanematsu et al., 2013), they have not developed models for arsenic adsorption onto lepidocrocite or examined the effect of direct addition of ferrous ion in the system.

Iron (oxyhydr)oxides can participate in the oxidation of As(III) to As(V), which can potentially affect arsenic mobility and toxicity. Ferrihydrite was found to have a catalytic effect on As(III) oxidation by oxygen on a time scale of several days to a week (Zhao et al., 2011). Photoinduced oxidation of As(III) was observed in the presence of goethite and ferrihydrite, and the iron(III) oxides were found to be the oxidants (Bhandari et al., 2011; Bhandari et al., 2012). Fe(II)-mediated As(III) oxidation in oxic conditions was observed in a sand column with aqueous Fe(II) (Bisceglia et al., 2005). As(III) oxidation was also observed on the surfaces of magnetite and ferrihydrite; while As(III) was rapidly oxidized upon adsorption to magnetite, As(III) oxidation on ferrihydrite was observed only after addition of aqueous Fe(II) within the examined time scale of 24 hours (Ona-Nguema et al., 2010). Dissolved oxygen and soluble intermediates involved in Fe(II) oxidation may act as rate-enhancing species in As(III) oxidation

(Sahai et al., 2007). Previous studies have proposed pH-dependent generation of oxidants in the Fenton reaction, where reactive oxygen species are produced at low pH while a less reactive but more selective oxidant [most likely Fe(IV)] forms at circumneutral pH (Hug and Leupin, 2003; Katsoyiannis et al., 2008). Further, an Fe(II)-activated Fe(III) intermediate species was suggested to induce redox transformation of arsenic at strictly anoxic conditions (Amstaetter et al., 2010). Lepidocrocite is a common iron oxyhydroxide found in soils that actively participates in iron redox cycling (Cornell and Schwertmann, 2003). It is also the dominant product of iron electrocoagulation, which is an effective treatment technique to remove arsenic from water (Ratna Kumar et al., 2004; Parga et al., 2005; Gomes et al., 2007; Thella et al., 2008; Balasubramanian et al., 2009; Lakshmanan et al., 2010; Wan et al., 2011; Li et al., 2012). The oxidation of As(III) on lepidocrocite has not previously been examined.

The objectives of this study were to quantify the impact of pH, dissolved oxygen, and Fe(II) presence on As(III) and As(V) adsorption on lepidocrocite by both experimental and modeling approaches. Batch experiments were performed to investigate arsenic adsorption to lepidocrocite as a function of lepidocrocite dose, pH, availability of oxygen, and the presence of aqueous Fe(II). In this study, surface complexation modeling was used to describe chemical interactions at the lepidocrocite interface.

2.2 Material and Methods

2.2.1 Materials

All chemicals were used as received from vendors. Solutions were prepared with ultrapure water (resistivity > 18.2 MΩ•cm). Glass volumetric flasks and beakers were acid-

cleaned and rinsed several times with deionized water and ultrapure water prior to use. As(III) and As(V) stock solutions were prepared from reagent grade $NaAsO_2$ and $Na_2HAsO_4 \cdot 7H_2O$ (Sigma Aldrich). A fresh batch of 90 mM Fe(II) solution was prepared before each experiment from $FeSO_4 \cdot 7H_2O$ (Sigma Aldrich). The HNO_3 was of trace-metal grade from Fisher Scientific. The NaOH for pH adjustment, and $NaNO_3$ and $NaHCO_3$ for ionic strength adjustment were of ACS grade.

2.2.2 Lepidocrocite Generation

Lepidocrocite was synthesized in a bench-scale electrocoagulation reactor that we previously used to examine arsenic removal (Wan et al., 2011). In the electrocoagulation process iron is released from an iron metal anode into solution as Fe(II) and it is then oxidized to Fe(III) by oxygen (Lakshmanan et al., 2009). The reactor consisted of a 1-L glass beaker with two iron rods immersed in 1 mM $NaHCO_3$ aqueous solution. Each rod had a diameter of 1.75 cm, length of 20 cm, and total wetted area of 57 cm^2. Before each synthesis run, the electrodes were abraded with sandpaper to remove scales and then cleaned with ultrapure water. A voltage of 12 V was applied to the electrodes from a direct current power supply. The solution was magnetically-stirred (200 rpm) and sparged with air at a flow rate above 60 mL/min to provide oxygen for the formation of Fe(III) precipitates. After a four-hour electrocoagulation run, the suspension pH was adjusted to approximately 7.7, which is a published pH_{pzc} of lepidocrocite determined from potentiometric titration data (Peacock and Sherman, 2004), to promote the settling of the solids. The supernatant was decanted and the suspension was further purified with dialysis. Dry solids were then obtained by freeze-drying. The precipitate was confirmed to be lepidocrocite from the X-ray diffraction (XRD) pattern, which was collected using a diffratometer with Cu Kα radiation (D-MAX/A, Rigaku, Japan) (Figure S2.1). About 100 mg of

lepidocrocite was generated in one run and the suspensions from multiple syntheses following the same protocol were combined to form a lepidocrocite stock suspension (6 g/L γ-FeOOH-Fe) that was then used for all adsorption and As(III) oxidation expermients.

2.2.3 Equilibrium Adsorption Experiments

Equilibrium adsorption of As(V) and As(III) to the lepidocrocite generated from electrocoagulation was investigated in batch experiments as a function of pH and arsenic or lepidocrocite loading. All experiments were performed in 50-mL digestion tubes (copolymer polypropylene), with suspensions continuously mixed by magnetically stirring at 300 rpm. Adsorption was initiated by the addition of 10 mg/L As(III) or As(V) stock solution (133.3 μM) to pH-adjusted lepidocrocite suspensions. Desired pH values from 4 to 10 were obtained by addition of either 0.1 M NaOH or 0.1 M HNO_3. The pH of the resulting suspensions was monitored throughout the course of adsorption experiments; the final pH measured at the end of the experiments is the value reported for equilibrium adsorption.

For As(III) adsorption, a total As concentration of 1.33 μM (100 μg/L) or 6.67 μM (500 μg/L) was used with a background electrolyte of 0.01 M $NaNO_3$. The concentrated lepidocrocite suspension was added to reach a loading of 120 mg Fe/L (190 mg γ-FeOOH/L). Based on preliminary experiments a reaction time of 48 h was found to ensure that As(III) adsorption reached equilibrium (Figure S2.2). For As(V) adsorption, a lepidocrocite concentration of 79 mg/L and a total As concentration of 1.33 μM (100 μg/L) or 13.3 μM (1000 μg/L) were used. The batch reactors were equilibrated for 24 h with a background electrolyte of 1 mM $NaHCO_3$.

In experiments to generate data for an As(III) adsorption isotherm at pH 7.5, 6.67 μM total As(III) was used with 8 different lepidocrocite loadings from 30 to 480 mg Fe/L. Experiments for both the As(III) adsorption edge and adsorption isotherm were performed in a

glovebox with an N_2/H_2 mixture circulated over a heated Pd catalyst to minimize As(III) oxidation by oxygen. For an As(V) adsorption isotherm at pH 4, the lepidocrocite concentration was fixed at 79 mg/L with total As(V) concentrations ranging from 2.2 to 94.1 μM. The pH values for the adsorption isotherms were selected such that they provided the maximum extent of adsorption for the particular arsenic oxidation state.

2.2.4 Effect of Fe(II)

Experiments with Fe(II) were performed to investigate Fe(II)-mediated As(III) oxidation. A volume of 500 μL 9 mM Fe(II) solution freshly made from $FeSO_4 \cdot 7H_2O$ solid was spiked together with the addition of As(III) stock solution to give a final Fe(II) concentration of 90 μM. To elucidate the role of Fe(II) on As(III) oxidation, some experiments were performed with the addition of 2-propanol as a radical scavenger, with 60 μL 2-propanol spiked into the batch reactor to give a 15 mM concentration. Previous research reported that this amount of 2-propanol would be able to quench hydroxyl radicals generated from the Fenton reaction (Buxton et al., 1988).

2.2.5 Dissolved Arsenic Speciation

An anion-exchange method (Ficklin, 1983) was adopted for dissolved arsenic speciation following the procedure outlined in a previous study (Wilkie and Hering, 1998). Samples of 5 mL volume were collected from the suspension during and at the end of experiments, diluted to 10 mL, and filtered through 0.22 μm polyethersulfone filter membranes. Half of the filtrate was adjusted to pH 5 and passed through a column of anion exchange resin (AG 1-X8 from Bio-Rad); the resin was received in chloride form and converted to an acetate form prior to use in arsenic separations. At pH 5, neutral As(III) species pass through the column while anionic

As(V) species are retained (Wilkie and Hering, 1998).The other half of the filtrate and the effluent from the column were then acidified to 2% HNO_3 by the addition of concentrated HNO_3 for analysis of total dissolved arsenic and As(III), respectively. The As(V) concentration was determined as the difference between total dissolved arsenic and As(III).

2.2.6 Analytical Methods

The filtered and acidified samples were analyzed for dissolved concentrations of As by inductively coupled plasma mass spectrometry (ICP-MS) (7500ce, Agilent Technologies, Santa Clara, CA). The detection limit for As was 0.1 μg/L. The Fe(II) concentration was determined using the ferrozine method (Stookey, 1970).

2.2.7 Surface Complexation Modeling

A surface complexation model was developed to fit both As(III) and As(V) adsorption data. The diffuse double layer model was employed to account for the electrostatic effects at the lepidocrocite surface. The surface area of lepidocrocite generated from this reactor has been observed in the range of 180 – 210 m^2/g, and a surface area of 201 m^2/g was chosen for the modeling; this value was measured for lepidocrocite synthesized from the same procedure in a previous study in our group (Wan et al., 2011). A surface site density of 1.6 sites/nm^2 and equilibrium constants of surface acid-base reactions reported for lepidocrocite by (Peacock and Sherman, 2004) were used; they had determined these values from FITEQL optimization of surface complexation parameters to fit potentiometric titration data. The equilibrium constants of lepidocrocite surface acid-base reactions were then adjusted to account for the difference in lepidocrocite specific area based on the approach described by (Sverjensky, 2003) (Table S2.1).

Two surface complex stoichiometries (monodentate and bidentate models) were evaluated for both As(III) and As(V) adsorption. One set of models used only monodentate surface complexation reactions with the consideration of reaction stoichiometries from a previous study that fit As(III) and As(V) adsorption onto goethite, amorphous iron oxide, and magnetite (Dixit and Hering, 2003). Other sets of models included bidentate reactions based on spectroscopic evidence for bidentate surface complexation of As(III) and As(V) on lepidocrocite (Farquhar et al., 2002; Manning et al., 2002; Sherman and Randall, 2003; Ona-Nguema et al., 2005). Multiple runs of equilibrium calculations in MINEQL+ v 4.6 (Schecher and McAvoy, 2007) were performed to determine both the best set of reactions for modeling As(III) and As(V) adsorption to lepidocrocite and the optimal values of the equilibrium constants of surface complexation reactions included in those models. The surface complex reactions included in the final model together with their equilibrium constants are summarized in Table 2.1. The aqueous reactions in the models are compiled in Table S2.4. The overall procedure for model development and optimization as well as the aqueous reactions are described in the Supporting Information.

2.3 Results and Discussion

2.3.1 Equilibrium As(III) Adsorption

As(III) adsorption onto lepidocrocite was mildly affected by pH (Figure 2.1a). Adsorption increased with increasing pH, reached a stable level of high adsorption between pH 6 and 9, and then decreased with further increase in pH. The maximum percentage of adsorption decreased with increasing total As(III) concentration, which reached 94% and 78% at around pH

8 for total As(III) concentrations of 1.33 µM (100 µg/L) and 6.67 µM (500 µg/L), respectively. Similar adsorption patterns with broad ranges of maximum adsorption have been observed for the pH dependence of As(III) adsorption onto an amorphous iron oxide and goethite (Wilkie and Hering, 1996; Dixit and Hering, 2003).

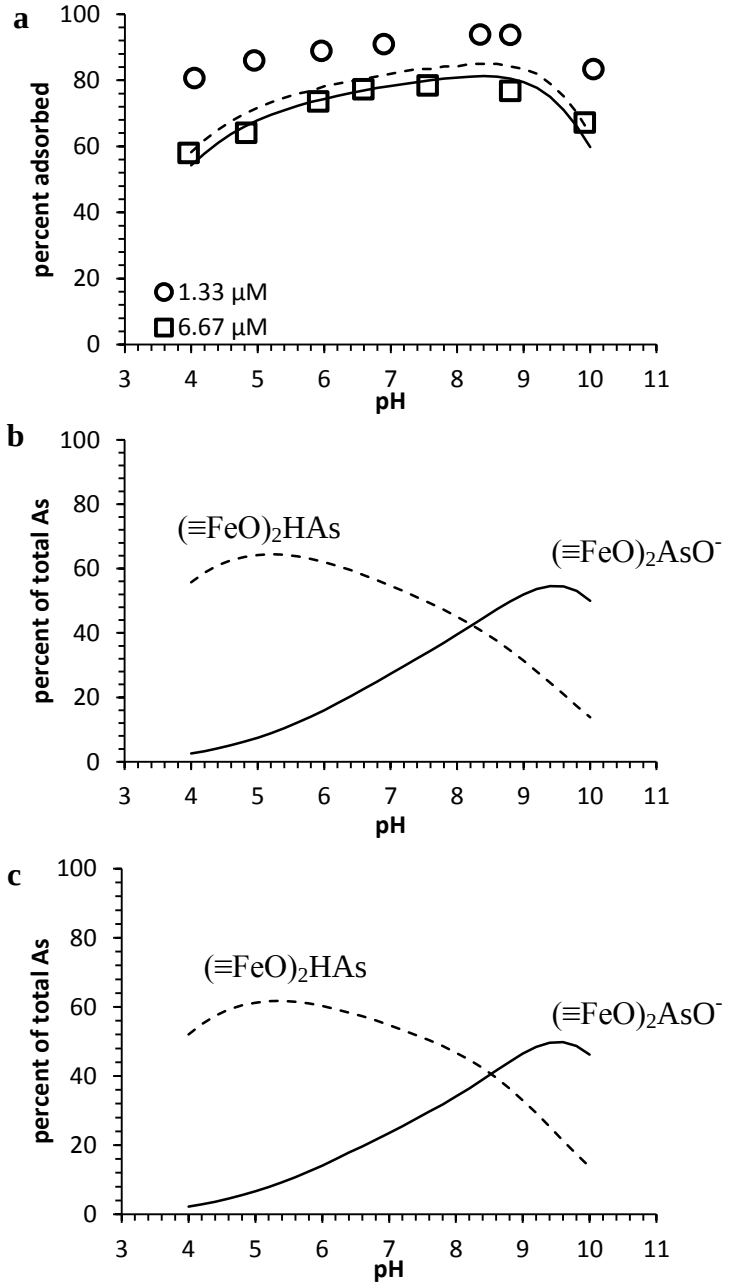

Figure 2.1 (a) As(III) adsorption edges on lepidocrocite at 1.33 and 6.67 µM total As(III) concentrations together with predicted surface speciation for (b) 1.33 µM As(III) and (c) 6.67 µM As(III). Experimental

data at 50 h adsorption are shown as markers; SCM predictions are shown as lines. All experiments were performed in a glovebox with N_2/H_2 passed over a heated Pd catalyst.

The capacity for As(III) adsorption was further explored at pH 7.5 (Figure 2.2a), which is the pH of the maximum adsorption density. With the specific surface area of 201 m^2/g and adsorbed As(III) species assumed to all be bidentate surface complexes (Table 2.1), the observed maximum adsorption density of 0.06 μM As/mg Fe corresponds to As(III) occupancy of 0.34 sites/nm^2. This value is lower than the total site density (1.6 sites/nm^2) used in the surface complexation modeling, which suggests that the majority of surface sites remained unoccupied by arsenic even at the highest total arsenic concentration studied. The adsorption density would still increase with increasing arsenic loading.

Greater arsenic adsorption with oxygen than at anoxic conditions was observed for experiments that started with As(III) (Figure 2.2a). This higher As adsorption was probably caused by As(III) oxidation to As(V) because As(V) adsorbs more strongly than As(III) at pH 7.5. Previous research indicated that lepidocrocite alone without oxygen could not oxidize As(III) (Ona-Nguema et al., 2005), which agrees with the dissolved arsenic speciation in the anoxic experiments in this study. It is likely that the lepidocrocite surface catalyzed the oxidation of As(III) by dissolved oxygen. Similar mechanisms have been suggested for As(III) oxidation in the presence of ferrihydrite (Zhao et al., 2011) and intercalated Fe(III)-montmorillonite nanoparticles (Izumi et al., 2005).

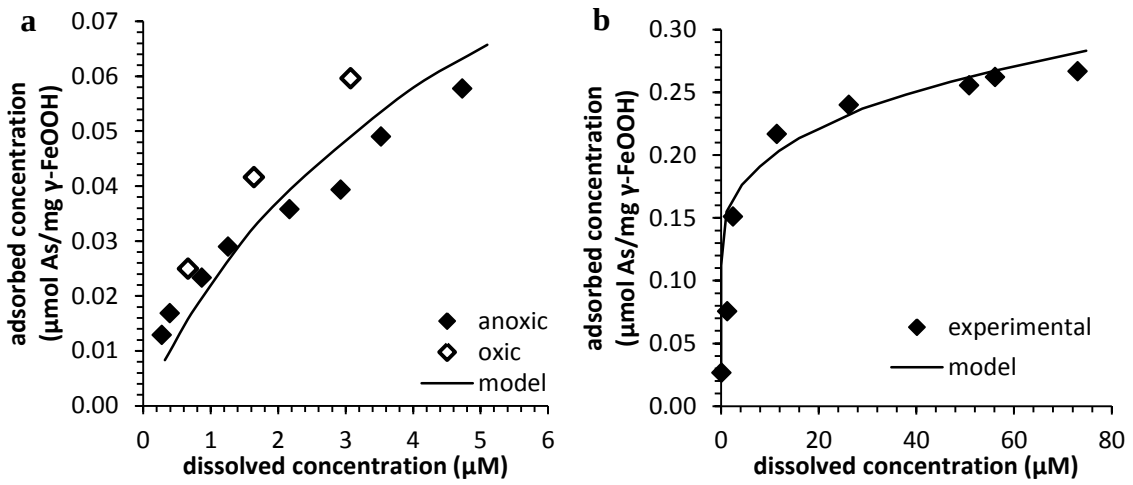

Figure 2.2 Adsorption isotherm-style data for (a) As(III) at pH 7.5 and (b) As(V) at pH 4. The line represents of the prediction from the same surface complexation model used to simulate adsorption edges in Figures 2.1 and 2.3. Experiments for As(III) adsorption in the anoxic series were performed in a glovebox with N_2/H_2 with the atmosphere circulated over a heated Pd catalyst.

2.3.2 Equilibrium As(V) Adsorption

The effect of pH on adsorption was much more pronounced for As(V) than it was for As(III) (Figure 2.3a). For a total As(V) concentration of 1.33 µM (100 µg/L), the amount of As(V) adsorbed remained close to 100% up to pH 8 and decreased sharply above this pH. For a total As(V) concentration of 13.3 µM (1000 µg/L), the adsorbed As(V) concentration steadily decreased with increasing pH from 4 to 10. Comparison of the adsorption edges for As(III) and As(V) shows that the As(V) adsorption is more favorable at lower pH, but at higher pH the degree of As(III) adsorption can be comparable to or even more favorable than As(V) adsorption. Similar trends have been observed for As(V) adsorption on other iron (oxyhydr)oxides (Wilkie and Hering, 1996; Dixit and Hering, 2003; Antelo et al., 2005; Zeng et al., 2007; Wan et al., 2011; Kanematsu et al., 2013). For the As(V) isotherm, the maximum surface coverage observed in our study corresponds to an adsorption density of 0.8 sites/nm^2 for monodentate surface complexation, indicating that there are still vacant sites for further adsorption at a higher As/Fe ratio if adsorption occurs as monodentate surface complexes.

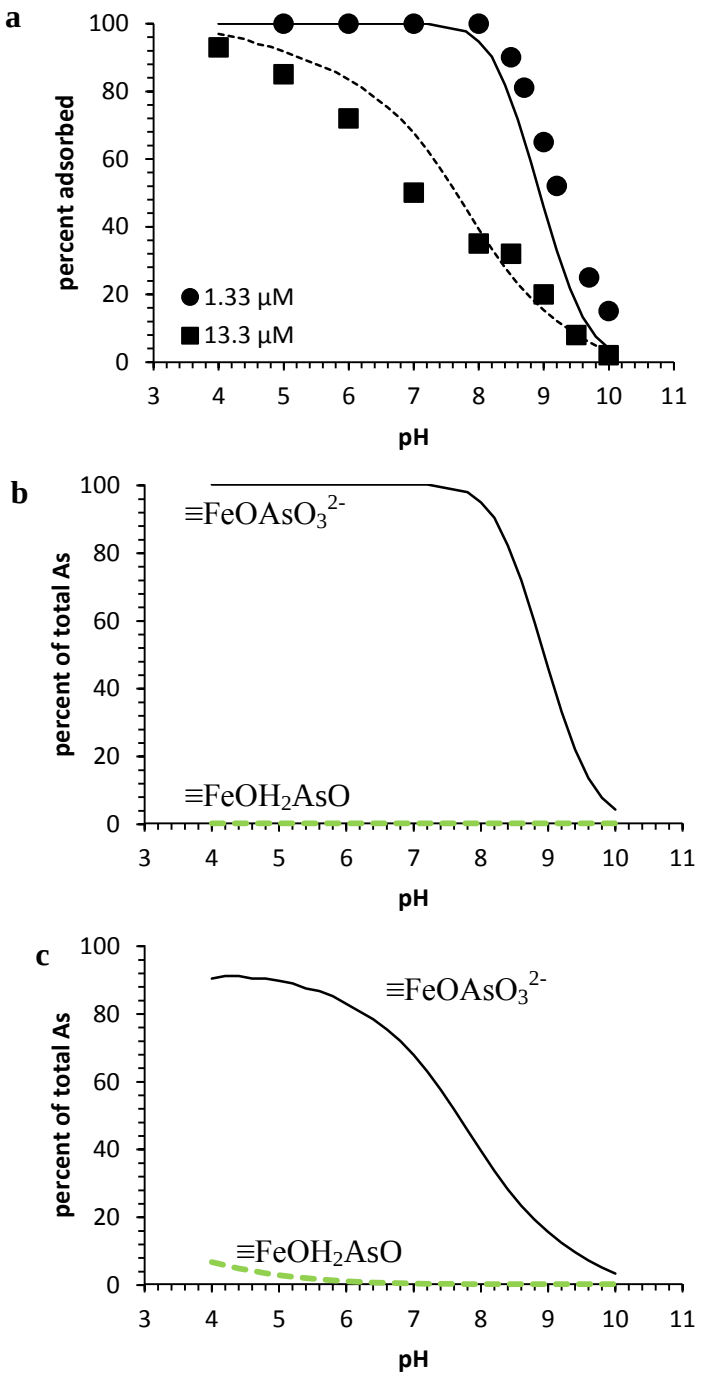

Figure 2.3 (a) As(V) adsorption edges on lepidocrocite at 1.33 and 13.3 µM total As(V) concentrations together with predicted surface speciation at (b) 1.33 µM As(V) and (c) 13.3 µM As(V). Experimental data at 50 h adsorption are shown as markers; SCM predictions are shown as lines.

2.3.3 Surface Complexation Modeling

Efforts were made to evaluate models that included only monodentate surface complexes and models that included bidentate surface complexes. For each of the four models evaluated, the Log K values of reactions were simultaneously optimized for both the adsorption edges and the adsorption isotherm (Tables S2.2 and S2.3). For As(III) adsorption, the model with only bidentate surface complexation reactions (Table 2.1) was finally adopted because of its ability to simulate the experimental data and its consistency with spectroscopic observations of adsorbed As(III) coordination environments from other studies. For As(V) adsorption, the model with only monodentate surface complexation reactions (Table 2.1) was selected because it fit both the adsorption edges and the isotherm very well. While a model that included two As(V) bidentate surface complexation reactions in addition to a monodentate surface complexation reaction (Table S2.3) could provide a good prediction for the adsorption edges, it was unable to provide a good fit of the adsorption isotherm. The protonated bidentate surface complex [$(\equiv FeO)_2HAsO_2$] that was the dominant species at pH 4 led to underprediction of arsenic adsorption, and the model could not accommodate an arsenic sorption density as high as 0.28 μM As(V)/mg γ-FeOOH (Figure 2.2b) that was observed experimentally.

The bidentate surface complexation model for As(III) and monodentate surface complexation model for As(V) (Table 2.1) could provide a good fit for the adsorption behavior of both species over a broad range of pH and total arsenic concentrations (Figures 2.1a and 2.3a). For the As(III) adsorption edge, the model fits well with the experimental data in terms of the overall curvature. However, the difference in the model predictions for the two total arsenic concentrations is always smaller than the differences in the experimental results for the two concentrations. The inability of the model to more perfectly fit data for both total arsenic

concentrations may be due to the model's consideration of only a single type of site on the lepidocrocite surface. In reality, different crystal faces and edges of the lepidocrocite particles may have different affinities for As(III) adsorption. When multiple types of sites (e.g., strong and weak sites) are present, sorption affinity varies as higher-affinity sites are preferentially filled and more abundant lower-affinity sites becomes dominant (Dzombak, 1990). Recent work has also considered the variation in surface site density on goethite as a function of particle size and morphology (Villalobos et al., 2009). A division of the lepidocrocite surface sites into different types could have yielded an improved fit of the model to the experimental data at both total arsenic concentrations.

Table 2.1 Reactions and parameters used for surface complexation modeling of As(V) and As(III) adsorption on lepidocrocite.

Reactions	Log K^{0} [a]	Log K^{0} [b]
Surface acid-base reactions		
$\equiv FeOH + H^+ = \equiv FeOH_2^+$	7.57 [c]	6.27
$\equiv FeOH = \equiv FeO^- + H^+$	-7.81 [c]	-9.11
As(V) adsorption (0.079 g/L γ-FeOOH, $[\equiv FeOH]_{total} = 4.22 \times 10^{-5}$ M, A = 201 m^2/g, N = 1.6 sites/nm^2)		
$\equiv FeOH + AsO_4^{3-} + 3H^+ = \equiv FeOH_2AsO_3 + H_2O$	29.5	28.2
$\equiv FeOH + AsO_4^{3-} + H^+ = \equiv FeOAsO_3^{2-} + H_2O$	19.8	18.5
As(III) adsorption (0.191 g/L γ-FeOOH, $[\equiv FeOH]_{total} = 1.02 \times 10^{-4}$ M, A = 201 m^2/g, N = 1.6 sites/nm^2)		
$2\equiv FeOH + AsO_3^{3-} + 3H^+ = (\equiv FeO)_2HAsO + 2H_2O$	37.8	35.5
$2\equiv FeOH + AsO_3^{3-} + 2H^+ = (\equiv FeO)_2AsO^- + 2H_2O$	45.6	43.3

[a] Intrinsic equilibrium constants calculated based on the correction established by Sverjensky (2003).
[b] Molar concentration based equilibrium constants, as input in MINEQL. Note that for bidentate species, the equilibrium constants as entered into MINEQL depend on the solid concentrations; more information is provided in the Supporting Information.
[c] Numbers are obtained from Peacock and Sherman (2004) and adjusted according to Sverjensky (2003).

The surface complexation model for As(III) that includes two bidentate surface complexes (Figures 2.1b and 2.1c) is consistent with the molecular structure of adsorbed As(III)

reported in other studies (Farquhar et al., 2002; Manning et al., 2002). Those studies used extended X-ray absorption fine structure spectroscopy (EXAFS) to determine that As(III) forms predominantly inner-sphere bidentate mononuclear edge-sharing (^{2}E) and binuclear corner-sharing (^{2}C) complexes with lepidocrocite at low surface coverages (0.016 – 0.018 moles of As/mole surface sites) comparable to the surface coverages in this work (0.010 – 0.051 moles of As/mole surface sites). The predicted surface speciation of As(III) is presented in Figures 2.1b and 2.1c. The protonated complex [$(\equiv FeO)_2HAsO$] and the deprotonated complex [$(\equiv FeO)_2AsO^-$] are dominant at low and high pH, respectively. The crossover pH for the two surface species increased with increasing As/Fe ratio, consistent with the predictions from an extended triple layer model developed for As(III) adsorption onto a goethite-based adsorbent (Kanematsu et al., 2013). While previous work (Ona-Nguema et al., 2005) also ascribed a portion of As(III) adsorption to monodentate mononuclear corner-sharing (^{1}V) complex, this species was only important at much higher arsenic surface coverages (0.36 moles of As/mole surface sites) than those of the present study, and even then the bidentate binuclear corner sharing (^{2}C) surface complex was the major surface species in the modeling done in that previous work.

The As(V) surface complexation model predicts that the deprotonated complex [$\equiv FeOAsO_3^{2-}$] dominates over the entire pH range from 4 to 10 for both total As(V) concentrations (Figures 2.3b and 2.3c). The protonated complex [$\equiv FeOH_2AsO_3$] will ultimately dominate at low pH with increasing arsenic loading. While inclusion of this complex was not necessary to provide good fits to the adsorption edges, its presence was necessary for the surface complexation model to provide a satisfactory fit of the adsorption-isotherm style data (Figure 2.2b).

In an attempt to establish a model consistent with spectroscopic and molecular observations (Sherman and Randall, 2003; Fukushi and Sverjensky, 2007), efforts were made to develop a surface complexation model that included two bidentate surface complexes and one monodentate surface complex (Table S2.3) for As(V). While this model could have its parameters optimized to fit either the adsorption edge or the adsorption isotherm, no optimization of the model could provide a good fit for both the adsorption edge and isotherm at conditions relevant to this study (more detailed discussion is included in the Supporting Information). Although deviating from the spectroscopic evidence, the monodentate model as adopted is consistent with previous studies (Wilkie and Hering, 1996; Dixit and Hering, 2003) on As(V) interactions with iron oxides and provides a simple yet successful simulation of the experimental data.

2.3.4 Impact of Fe(II) on As(III) Adsorption on Lepidocrocite

The occurrence of iron cycling between dissolved Fe(II) and solid Fe(III) (oxyhydr)oxides in both natural and engineered systems motivated the design of experiments with both Fe(II) and lepidocrocite. These conditions are relevant to those of an electrocoagulation reactor or to a groundwater system in which Fe(II) is oxidized to produce Fe(III) (oxyhydr)oxides. The experiments performed in this study found that 1) lepidocrocite alone cannot oxidize As(III), 2) As(III) oxidation is favorable but slow in the copresence of lepidocrocite and oxygen, and 3) the addition of Fe(II) induces fast oxidation of As(III) to As(V) and greatly enhances total arsenic adsorption both with and without oxygen.

The addition of 90 μM Fe(II) significantly enhanced the extent of arsenic adsorption both with and without dissolved oxygen at pH 5.6 when starting with As(III) (Figure 2.4). This increase was slightly more evident with oxygen, as almost all arsenic was removed from the

aqueous phase within 24 h. This promotional effect was evident even after 1 h of adsorption. Fe(II) probably enhanced arsenic adsorption in experiments starting with As(III) by contributing to the oxidation of As(III) to As(V), which is more readily adsorbed to lepidocrocite at this pH.

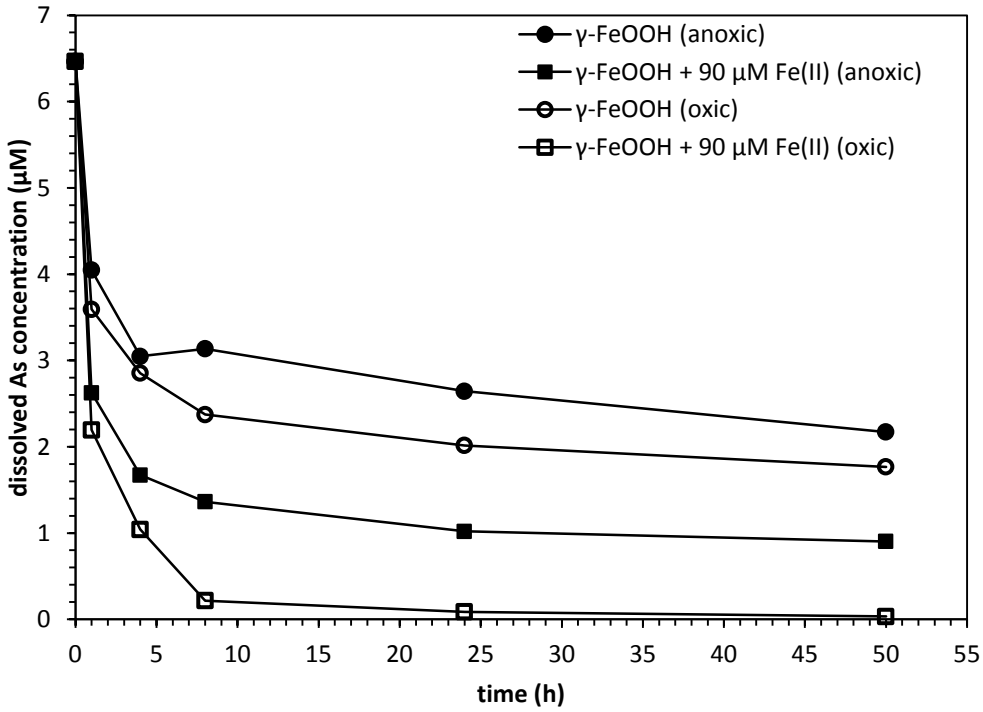

Figure 2.4 Dissolved arsenic concentration profile with (squares) and without (circles) 90 µM Fe(II) in anoxic (closed symbols) and oxic (open symbols) conditions at pH 5.6. All experiments started with 6.67 µM (500 µg/L) As(III). Data are shown as the average of the duplicates, and the relative standard deviations between replicates were always below 5%.

Measurements of aqueous arsenic speciation (Figure 2.5) provide evidence for As(III) oxidation in the presence of Fe(II). When neither oxygen nor Fe(II) was present (Figure 2.5a), As(III) oxidation was negligible, which agrees with previous studies that found that lepidocrocite alone could not oxidize As(III) (Ona-Nguema et al., 2005). The 10% decrease in Fe(II) concentration at anoxic conditions (Figure 2.5a) can be best explained by the adsorption to lepidocrocite, as Fe(II) adsorption has been observed on the surface of hematite (Larese-Casanova and Scherer, 2007), goethite, lepidocrocite and ferrihydrite (Hiemstra and van

Riemsdijk, 2007). This adsorption of Fe(II) to lepidocrocite was further confirmed by an anoxic control experiment where only Fe(II) and lepidocrocite were present without adding arsenic (data not shown), indicating that Fe(II) was not oxidized when there was no oxygen.

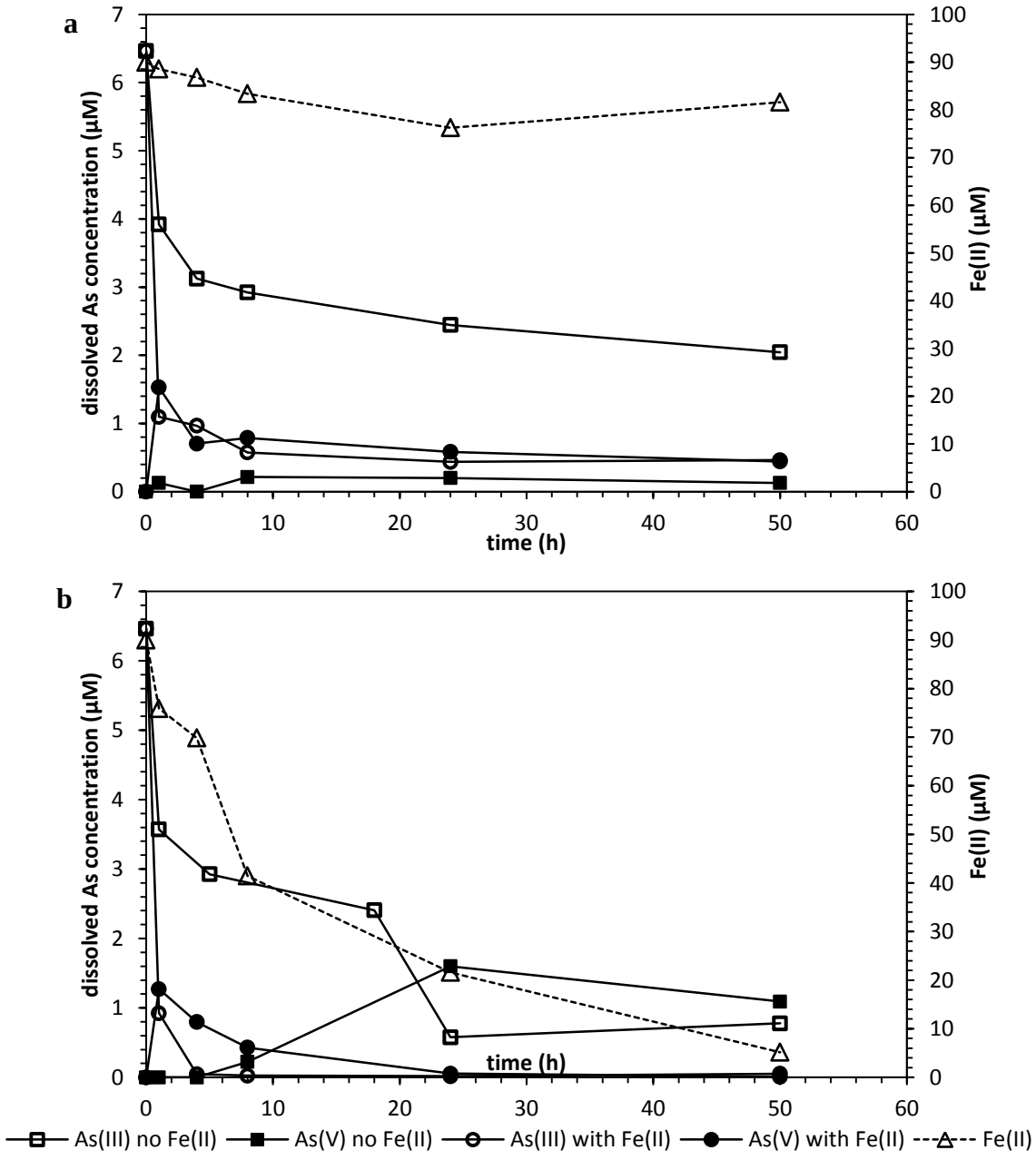

Figure 2.5 Dissolved arsenic speciation and Fe(II) concentration in (a) anoxic and (b) oxic conditions at pH 5.6. All experiments started with 6.67 µM (500 µg/L) As(III). Experiments with Fe(II) had an initial Fe(II) concentration of 90 µM. Data are shown as the average of the duplicates, and the relative standard deviations between replicates were always below 5%.

The extent of As(III) adsorption at 50 hours is consistent with the results predicted by the surface complexation model discussed in the last section, indicating that equilibrium had been reached. The addition of Fe(II) led to the generation of measurable As(V) in solution throughout the course of the experiment. Both dissolved As(III) and As(V) concentrations decreased over time. At the end of the experiment, 0.46 μM (34.6 μg/L) As(III) and 0.44 μM (33.1 μg/L) As(V) remained in the aqueous phase. For these dissolved concentrations, the equilibrium adsorption densities of As(III) and As(V) can be predicted by the surface complexation model. The surface complexation model predicts that while the dissolved concentrations of As(III) and As(V) are similar, the ratio of As(III) to As(V) complexes at the lepidocrocite surface would be 1:3.

In the presence of oxygen and absence of Fe(II), As(V) was not detectible in the solution until 8 h into the reaction (Figure 2.5b). After that time the dissolved As(V) concentration increased due to oxidation and then decreased as a result of adsorption on lepidocrocite. This slow oxidation can explain the slightly enhanced arsenic adsorption in the presence of oxygen (Figure 2.3a) as As(V) adsorbs more strongly than As(III) at circumneutral pH. However, at the end of the experiment, considerable amounts of both As(III) and As(V) remained in the solution. In contrast, the addition of Fe(II) in the presence of oxygen greatly enhanced As(III) oxidation; As(V) was the dominant dissolved arsenic species in all samples with both Fe(II) and oxygen. After 28 h almost all arsenic had transferred from the aqueous phase to the solid phase. The Fe(II) concentration decreased substantially with time, indicating the oxidation of Fe(II) in the presence of oxygen followed by precipitation (Figure S2.3).

Fe(II)-promoted oxidation of As(III) has been observed in previous studies and was attributed to the pH dependent formation of oxidants from the Fenton reaction in the presence of oxygen (Hug and Leupin, 2003; Katsoyiannis et al., 2008; Ona-Nguema et al., 2010; Li et al.,

2012; van Genuchten et al., 2012). The Fenton reaction produces hydroxyl radical at acidic pH and another oxidant, usually presumed to be Fe(IV), above pH 5 (Remucal and Sedlak, 2011). The latter is less reactive but more selective towards As(III) oxidation (Hug and Leupin, 2003). To see whether the Fenton reaction played a role in our system, 2-propanol was used as a radical scavenger to probe the formation of hydroxyl radical. If 2-propanol could effectively inhibit As(III) oxidation at acidic conditions and have negligible effects at pH above 5, then the Fenton reaction is most likely to play a role in the fast adsorption of arsenic onto lepidocrocite in the presence of Fe(II).

The adsorption experiment results with Fe(II) and 15 mM 2-propanol as a radical scavenger agreed with the Fenton reaction hypothesis (Figure 2.6). At pH 5.6 (Figure 2.6a), the addition of 2-propanol had a negligible effect on the As(III) oxidation in that almost all As, regardless of its speciation, transferred from the aqueous phase to solid phase within 24 h. This observation is consistent with a previous study on As(III) oxidation and removal during iron electrocoagulation at circumneutral pH (Li et al., 2012). At pH 4 (Figure 2.6b), the addition of 2-propanol effectively inhibited As(III) oxidation. Dissolved As(V) concentrations were much lower when both Fe(II) and 2-propanol were present, less than one fifth of those without 2-propanol. While the Fenton reaction was likely to contribute to As(III) oxidation and the overall enhanced arsenic adsorption, it is worthwhile to note that at pH 4 the dissolved As(III) concentrations were also considerably lower with 2-propanol than without. The 2-propanol might alter the surface properties of the lepidocrocite (e.g. surface charge distribution) so that the solids have a stronger affinity for arsenic adsorption.

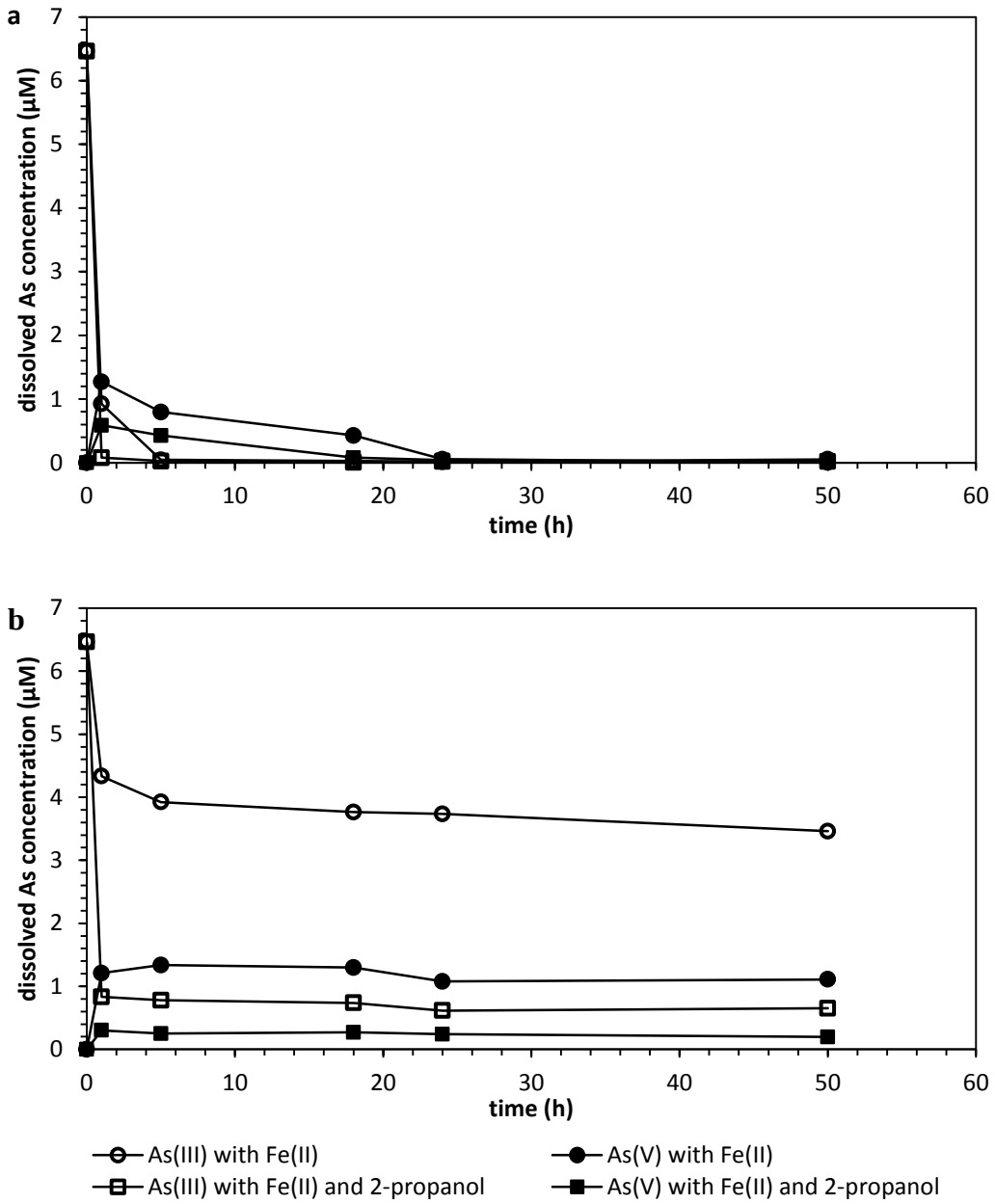

Figure 2.6 Dissolved arsenic speciation in the presence of Fe(II) and O_2 with/without 2-propanol at (a) pH 5.6; (b) pH 4. All experiments started with 6.67 µM (500 µg/L) As(III) and 90 µM Fe(II). The concentration of 2-propanol was 15 mM. Data are shown as the average of the duplicates, and the relative standard deviations between replicates were always below 5%.

Fe(II) also induced As(III) oxidation in the absence of oxygen (Figure 2.5a). Rapid As(III) oxidation was observed in strictly anoxic conditions for Fe(II)-goethite systems, which

was attributed to the formation of a reactive intermediate Fe(III) phase upon Fe(II) addition and electron transfer into bulk goethite (Amstaetter et al., 2010). While the atom exchange between Fe(II) and goethite did not induce any phase transformation (Handler et al., 2009), the reaction of Fe(II) with ferrihydrite promoted its transformation into more stable phases such as lepidocrocite and goethite (Pedersen et al., 2005). In the presence of Fe(II), lepidocrocite has been observed to rapidly release Fe into the solution (Pedersen et al., 2005); the solid phase either remained untransformed or transformed to magnetite only with a Fe(II) concentration above 0.6 mM (Pedersen et al., 2006), a concentration much higher than that of this study. Therefore the most plausible explanation for As(III) oxidation and the subsequent overall enhancement of arsenic adsorption is the formation of a reactive intermediate phase during the recrystallization of lepidocrocite induced by the addition of Fe(II).

2.4 Conclusions

In engineered systems iron (oxyhydr)oxides are often used to remove arsenic from drinking water. The co-occurrence of aqueous Fe(II) and Fe(III) solids is beneficial for arsenic removal because Fe(II) can induce As(III) oxidation to As(V) and thus alter arsenic adsorption behavior. The pH should be controlled carefully as both As(III) and As(V) adsorption to iron (oxyhydr)oxides are affected by pH. Above pH 8 As(V) can be more mobile than As(III); at low pH where Fenton chemistry generates hydroxyl radical, the presence of radical scavengers such as carbonate and NOM can compete for the oxidants with As(III). In groundwater systems where dissolved Fe(II) and Fe(III) (oxyhydr)oxides are both commonly found, the rise and drop of the water table may lead to alternate oxidative and reductive environments that influence the fate and transport of arsenic.

Acknowledgements

This study was supported by research funding from the Washington University International Center for Advanced Renewable Energy and Sustainability. The authors thank Wei Wan for his previous work on related projects, and Xiaochen Zuo and Patty Wurm for their assistance with the experiments and analyses.

Chapter 2. Supporting Information

Supporting information for Chapter 2 includes three figures (XRD pattern of lepidocrocite, time series of selected batch experiments, and the calculation of Fe(II) oxidation rate) and four tables with reactions for surface complexation modeling. The detailed procedure for developing and optimizing the surface complexation model is also included.

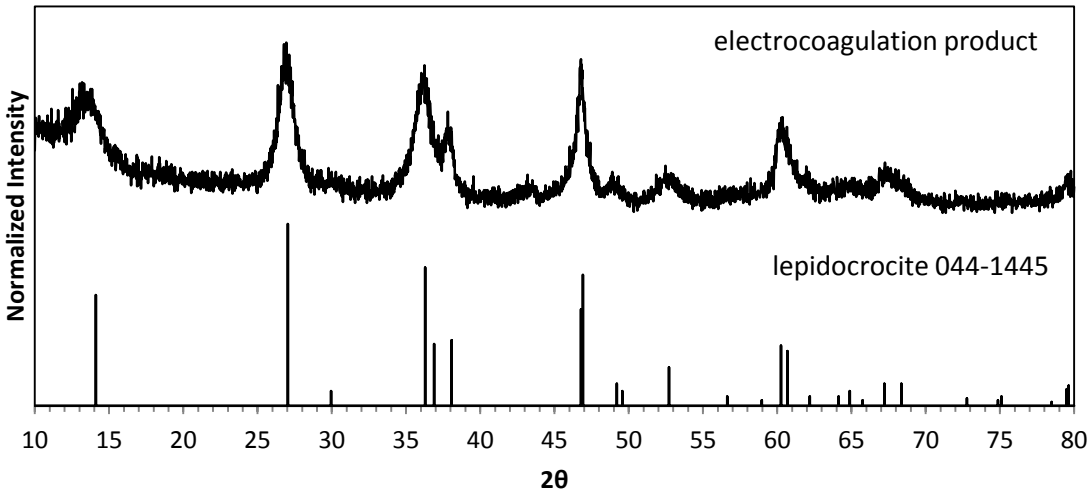

Figure S2.1 X-ray diffraction pattern for freeze-dried electrocoagulation product with the reference pattern for lepidocrocite. The match of the two patterns indicates that the product of electrocoagulation is lepidocrocite.

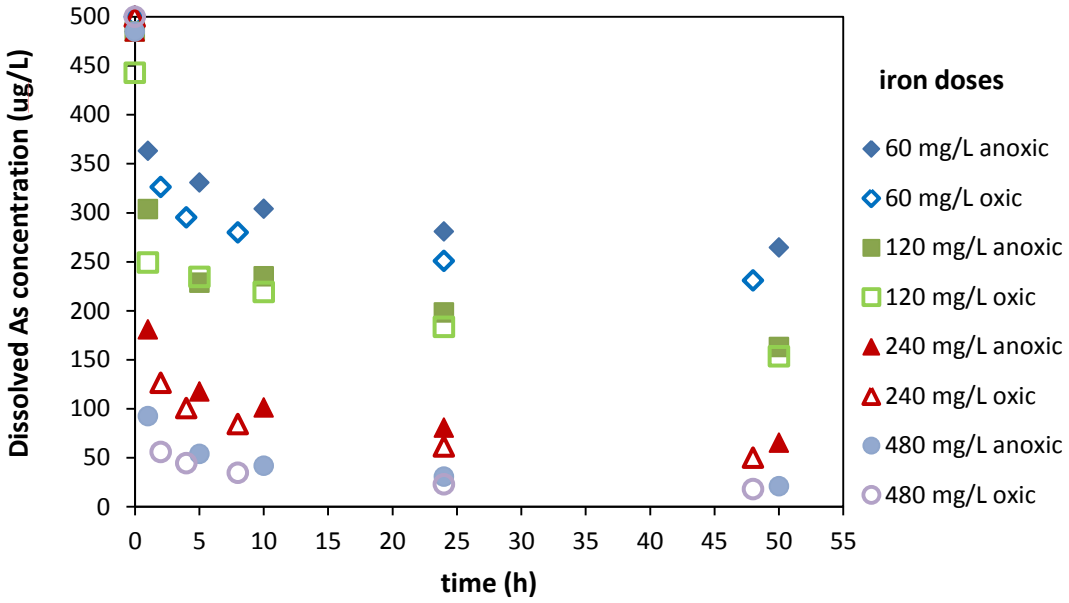

Figure S2.2 Dissolved As concentration profile over time with and without oxygen starting with 6.67 mM As(III) at pH 7.5. The data show that 48 hours are sufficient for As(III) adsorption to lepidocrocite to reach equilibrium.

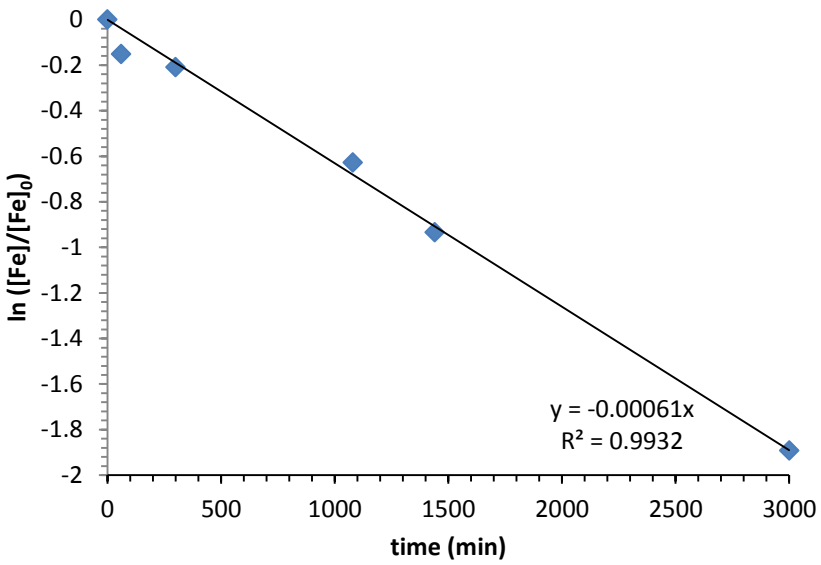

Figure S2.3 Calculation of Fe(II) oxidation rate for experiment that started with 6.67 μM As(III) in the presence of 90 μM Fe(II) and oxygen at pH 5.6.

The rate form was expressed as $-d[Fe(II)]/dt = k[OH^-]^2P_{O_2}[Fe(II)]$ where $P_{O_2} = 0.21$ atm. The line was a linear regression on the data points from experimental measurements. The slope of the linear trend line corresponds to a rate constant of 1.9×10^{14} $M^{-2}atm^{-1}min^{-1}$.

Procedure for Developing and Optimizing Surface Complexation Models

The surface complexation modeling approach was started by building the basic inputs to the models based on the published literature. The identification of possible surface complexation reactions was then considered based on published models and spectroscopic data from previous studies that determined the molecular-scale structures of adsorbed species. Various models, with each model consisting of different sets of reactions, were optimized with the model input compared to the data. Ultimately, one model for As(III) and one model for As(V) were selected. The steps below describe the sequence for the overall surface complexation model development.

1) A surface site density of 1.6 sites/nm^2 reported by Peacock and Sherman (2004) was used; they had determined this value from FITEQL simulation of potentiometric titration data of lepidocrocite.

2) Equilibrium constants of lepidocrocite surface acid-base reactions were taken from Peacock and Sherman (2004) and adjusted based on the approach described by Sverjensky (2003) for accounting for differences in specific surface area (Table S2.1). The Peacock and Sherman study used lepidocrocite with a specific surface area of 75.24 m^2/g, while our study used lepidocrocite with a specific surface area of 201 m^2/g.

Table S2.1 Adjustment of equilibrium constants of lepidocrocite surface acid-base reactions

Reactions	Log K [a]	Log K^{0} [b]	Log K^{0} [c]
$\equiv FeOH + H^+ = \equiv FeOH_2^+$	6.69	7.57	6.27
$\equiv FeOH = \equiv FeO^- + H^+$	-8.69	-7.81	-9.11

[a] Molar concentration based equilibrium constants from Peacock and Sherman (2004).
[b] Intrinsic equilibrium constants calculated based on the correction established by Sverjensky (2003).
[c] Molar concentration based equilibrium constants, as input in MINEQL. Note that for surface acid-base reactions, the equilibrium constants are independent of solid concentrations.

Implementing the surface complexation model with bidentate surface complexes in MINEQL required some adjustments to provide a model that was internally consistent. In MINEQL, an exponent of two is used for the activity of ≡FeOH in the mass action expression for bidentate surface complexation. The equilibrium constants in MINEQL are with a standard state of 1 mol/L and are not instrisically independent of the specific surface areas or the site density of the adsorbents. Because the models in the present study involved the comparison of As(III) and As(V) adsorption at different solid concentrations and denticity, the traditional molar-based constants (K^0) were converted into intrinsic equilibrium constants (K^θ) using the corrections established by Sverjensky (2006):

For monodentate surface complexation,

$$K^\theta = K^0 \left(\frac{NA}{N^* A^*}\right)$$

For bidentate surface complexation,

$$K^\theta = K^0 \left(\frac{(NA)^2}{N^* A^*}\right) C_S$$

where N (sites/nm^2) and A(m^2/g) are the site density and specific surface area of the lepidocrocite. N^* = 10 sites/nm^2 and A^* = 10 m^2/g are selected as the reference site density and specific surface area. C_S (g/L) is the concentration of lepidocrocite solid. Ultimately the selection of the particular reference site density and specific surface area do not affect the molar concentration based equilibrium constants in MINEQL because these equations are then used to determine the constants for the exact surface area and site density used in our study.

3) Constrain the denticity of the surface complexation reactions of As(III) and As(V) adsorption onto lepidocrocite based on previous studies.

a. Ona-Nguema et al. (2005) found from EXAFS analysis that As(III) forms dominantly bidentate binuclear corner sharing (^{2}C) sorption complexes with a minor amount of monodentate mononuclear corner sharing (^{1}V) sorption complexes. Manning et al. (2002) and Farquhar et al. (2002) had similar findings with their EXAFS measurements that As(III) forms both bidentate mononuclear edge-sharing (^{2}E) and binuclear corner-sharing (^{2}C) complexes with lepidocrocite. This discrepancy in the occurrence of the mononuclear edge-sharing complex was hypothesized to be related to the difference in surface coverages such that at low surface coverage, ^{2}E complexes would be favored over ^{2}C and ^{1}V complexes on the lepidocrocite surface. The conditions in our study are closer to the low surface coverage values reported in these studies, so for the As(III) bidentate model, only bidentate surface complexes were included.

b. Sherman and Randall (2003) used density functional theory calculations as well as EXAFS measurements to conclude that for As(V) adsorbed to lepidcrocite, the bidentate corner-sharing (^{2}C) complexes would be substantially more favorable than ^{2}E and ^{1}V complexes. Farquhar et al. (2002) also observed the dominance of bidentate arsenic complexes on lepidocrocite in their EXAFS analysis.

c. For both As(III) and As(V), efforts were made to develop models that contained only monodentate surface complexes (as used in many other studies) and models that included bidentate surface complex reactions (for consistency with spectroscopic and molecular evidence). In total, four models (Tables S2.2 and S2.3) were evaluated. Here we refer to these model as As(III) monodentate, As(III) bidentate, As(V) monodentate and As(V) bidentate; the As(V) bidentate model also included one monodentate surface complexation reaction. Ultimately, the As(III) bidentate model and As(V) monodentate model were used because of their ability to simulate both the adsorption edges and isotherms.

4) Development of As(V) monodentate surface complexation model

a. Optimization of the Log K values of reactions that form $\equiv FeOH_2AsO_3$, $\equiv FeOHAsO_3^-$, and $\equiv FeOAsO_3^{2-}$ (Table S2.2)

The data of the two adsorption edges in Figure 2.3a were used to obtain the optimized Log K values for the three monodentate surface complexes. The three surface complexes were expected to all contribute to As(V) adsorption over a wide pH range and each would dominate in different pH regions. Multiple forward calculations of the model in MINEQL were performed with a matrix of different combinations of the three Log K values to find the set of constants that yielded the minimum sum of squares of the residuals between experimental and predicted results of adsorption percentages from the two adsorption edges.

b. Minor adjustment for fitting As(V) adsorption isotherm

The Log K values that generated the best fit for the adsorption edges had only one surface complex, $\equiv FeOAsO_3^{2-}$, that dominated over the entire pH range from 4 to 10. However, the best fit model for the adsorption edges provided a poor fit of the As(V) adsorption isotherm at pH 4 because it systematically underestimated As(V) adsorption at high As/Fe ratios at pH 4. An adjustment to increase the Log K for $\equiv FeOH_2AsO_3$ while decreasing the Log K for $\equiv FeOAsO_3^{2-}$ significantly improved the fitting for the adsorption isotherm while maintaining a very good fit to the adsorption edges.

c. Sensitivity tests and finalizing the model for As(V) monodentate model

Steps a and b were repeated to update the three Log K values in the As(V) monodentate complex model to reach the best overall simulation for both adsorption edges and isotherm. Model sensitivity to the individual Log K values was tested at different pH regions. For the final model shown in Table 2.1, the reaction for formation of $\equiv FeOHAsO_3^-$ was removed (Table S2.2)

because that specific Log K had no impact on the fitting, and $\equiv FeOHAsO_3^-$ remained negligible throughout the pH range and As(V) concentrations considered.

Table S2.2 Surface species and reactions in monodentate surface complexation modeling

Reactions	Log K^{0} [a]	Log K^{0} [b]
Model 1: As(V) monodentate		
(0.079 g/L γ-FeOOH, $[\equiv FeOH]_{total}$ = 4.22 × 10^{-5} M, A = 201 m^2/g, N = 1.6 sites/nm^2)		
$\equiv FeOH + AsO_4^{3-} + 3H^+ = \equiv FeOH_2AsO_3 + H_2O$ [d]	**29.5**	**28.2**
$\equiv FeOH + AsO_4^{3-} + 2H^+ = \equiv FeOHAsO_3^- + H_2O$ [c]		
$\equiv FeOH + AsO_4^{3-} + H^+ = \equiv FeOAsO_3^{2-} + H_2O$ [d]	**19.8**	**18.5**
Model 2: As(III) monodentate		
(0.19 g/L γ-FeOOH, $[\equiv FeOH]_{total}$ = 1.02 × 10^{-4} M, A = 201 m^2/g, N = 1.6 sites/nm^2)		
$\equiv FeOH + AsO_3^{3-} + 3H^+ = \equiv FeOH_2AsO_2 + H_2O$	32.21	31.70
$\equiv FeOH + AsO_3^{3-} + 2H^+ = \equiv FeOHAsO_2^- + H_2O$	39.84	39.33

[a] Intrinsic equilibrium constants calculated based on the correction established by Sverjensky (2003).
[b] Molar concentration based equilibrium constants, as input in MINEQL. Note that for monodentate species, the equilibrium constants are independent of solid concentrations.
[c] This reaction was removed because the $\equiv FeOHAsO_3^-$ species was never predicted to be present at even 1% of the total surface As thoughout pH 4-10 for both As(V) concentrations. Consequenlty, its inclusion did not improve the quality of the fit to the model.
[d] Reactions in bold red are the ones that are included in the final model.

5) Development of As(III) monodentate model (Table S2.2), As(V) bidentate model and As(III) bidentate model (Table S2.3) using similar strategies outlined in Step 4.

Table S2.3 Surface species and reactions in bidentate surface complexation modeling

Reactions	Log K^{0} [a]	Log K^{0} [b]
Model 3: As(V) bidentate		
(0.079 g/L γ-FeOOH, $[\equiv FeOH]_{total}$ = 4.22 × 10^{-5} M, A = 201 m^2/g, N = 1.6 sites/nm^2)		
$2\equiv FeOH + AsO_4^{3-} + 3H^+ = (\equiv FeO)_2HAsO_2 + 2H_2O$		
$2\equiv FeOH + AsO_4^{3-} + 2H^+ = (\equiv FeO)_2AsO_2^- + 2H_2O$		
$\equiv FeOH + AsO_4^{3-} + H^+ = \equiv FeOAsO_3^{2-} + H_2O$		
Model 4: As(III) bidentate		
(0.19 g/L γ-FeOOH, $[\equiv FeOH]_{total}$ = 1.02 × 10^{-4} M, A = 201 m^2/g, N = 1.6 sites/nm^2)		
$2\equiv FeOH + AsO_3^{3-} + 3H^+ = (\equiv FeO)_2HAsO + 2H_2O$ [c]	**37.8**	**35.5**
$2\equiv FeOH + AsO_3^{3-} + 2H^+ = (\equiv FeO)_2AsO^- + 2H_2O$ [c]	**45.6**	**43.3**

[a] Intrinsic equilibrium constants calculated based on the correction established by Sverjensky (2003).

[b] Molar concentration based equilibrium constants, as input in MINEQL. Note that for bidentate species, the equilibrium constants are dependent of solid concentrations.

[c] Reactions in bold red are the ones that are included in the final model.

6) Determination of final models used in the study

For As(III) adsorption, the monodentate surface complex model (Model 2 in Table S2.2) and bidentate surface complex model (Model 4 in Table S2.3) could both provide good fitting for adsorption edges and the adsorption isotherm. However, the bidentate complex model was finally adopted for its consistency with the spectroscopic observations in other studies that As(III) bidentate complexes at the lepidocrocite surface were the dominant species (Step 3a).

For As(V) adsorption, the monodentate complex model (Model 1 in Table S2.2) could simulate both the adsorption edges and isotherm very well. While the bidentate model (Model 3 in Table S2.3) could provide a good prediction for the adsorption edges, it could not fit the isotherm because with bidentate surface complexes being the dominant species at pH 4, the model would run out of surface sites and could not accommodate the sorption density as high as 0.28 μM As(V)/mg γ-FeOOH (Figure 2.2b) that was observed in our study.

Table S2.4 Other aqueous reactions used in the surface complexation modeling

Reactions	Log K
As(V) acid-base reactions	
$AsO_4^{3-} + H^+ = HAsO_4^{2-}$	11.50
$AsO_4^{3-} + 2H^+ = H_2AsO_4^-$	18.46
$AsO_4^{3-} + 3H^+ = H_3AsO_4$	20.70
As(III) acid-base reactions	
$AsO_3^{3-} + H^+ = HAsO_3^{2-}$	13.414
$AsO_3^{3-} + 2H^+ = H_2AsO_3^-$	25.454
$AsO_3^{3-} + 3H^+ = H_3AsO_3$	34.744

Chapter 3: Impact of Water Chemistry on Element Mobilization from Eagle Ford Shale

Results of this chapter have been published in *Environmental Engineering Science* (early online access).

Graphical Abstract

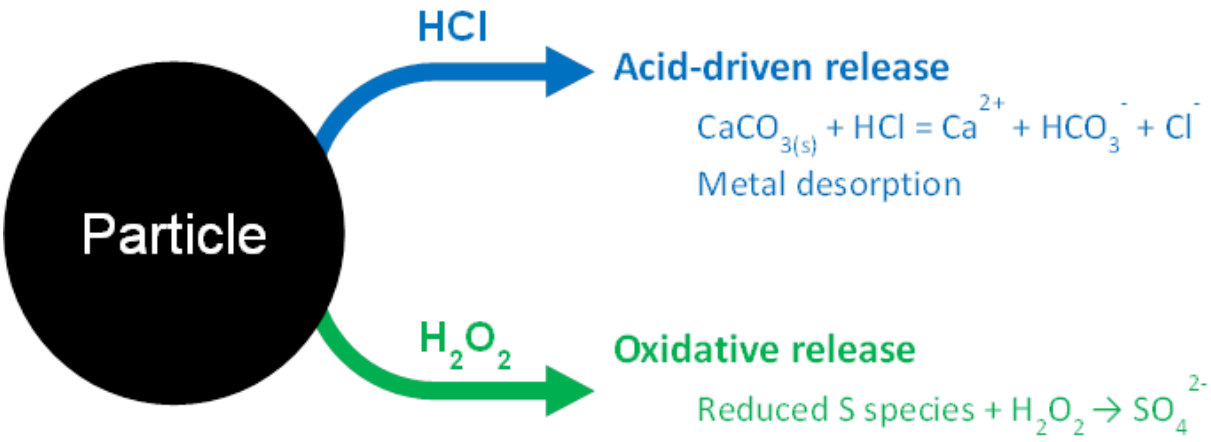

Abstract

The rapid expansion of hydraulic fracturing operations for natural gas and oil production can impact water quality. The water that flows back to the surface as part of the hydraulic fracturing process and during well production can contain trace elements, including regulated metals and metalloids, mobilized by interactions of the fracturing fluid with the formation. The rate and extent of mobilization depends on the geochemistry of the formation, the composition of the fracturing fluid, and the contact time. Laboratory experiments detailed here examined the influence of water chemistry on element mobilization from core samples taken from the Eagle Ford formation, which is currently producing natural gas from hydraulically fractured zones. Fluid properties were varied with regard to pH, oxidant level, and solid:water ratio. The release of elements (Ca, Mg, Fe, Ba, As) from the Eagle Ford samples strongly depended on pH, which in turn was primarily controlled by calcite dissolution. The presence of oxygen and addition of H2O2 led to pyrite oxidation and resulted in an elevated amount of sulfate. Barium concentrations were largely controlled by the amount of sulfate present via solubility equilibrium of barite that formed as a secondary phase. The effect of increasing solid:water ratio on the extents of mobilization varied widely for different elements. Taken together, these findings demonstrate the need to understand both the aqueous- and geo-chemistries of a hydraulically fractured formation with regard to elemental mobilization in produced and flow back waters.

Keywords

Hydraulic Fracturing, Eagle Ford Shale, Flowback Water, Element Mobilization

3.1 Introduction

Recent advances in energy recovery technologies from low-porosity formations have increased viable oil and gas reserves for a number of regions, including the United States (Kuuskraa et al., 2011). Shale gas and oil, in particular, has been a production focus in recent years due to advances in horizontal drilling and hydraulic fracturing techniques (GWPC et al., 2009; U.S. EIA, 2013). The United States has led in the development of shale-based, petroleum resources and the total U.S. proven reserves of wet natural gas have correspondingly increased from 192 tcf (trillion cubic feet) in 2001 to 323 tcf in 2012 (U.S. EIA, 2014). Natural gas currently supplies 27% of primary energy in the United States, with growth in total natural gas consumption expected at 0.7% per year from 2012 to 2040 (U.S. EIA, 2014).

Hydraulic fracturing (also referred to as "fracking") is typically done by pumping a mixture of water, proppant, and chemical additives into the well bore, under pressure, to create and propagate fractures in the surrounding formation (Ely, 1985). The proppant (fine sand or ceramic grains) is added to hold resulting pores and channels open in the formation thus allowing for subsequent oil and gas extraction. A typical fracturing job can require 2-5 million gallons (7,000-18,000 m^3) of water (Hagemeier and Hutt, 2009; Gregory et al., 2011). After the fracturing process some of the fracturing fluid returns to the surface and is referred to as flowback. As an example, for hydraulically fractured wells in Pennsylvania, 9-53% of the injected fracturing fluid is recovered as flowback (Vidic et al., 2013). Flowback contains the original or degraded additives as well as constituents mobilized from the formation. These can include a number of metals, metalloids, dissolved organics and hydrocarbons (Benko and Drewes, 2008; Gregory et al., 2011). Flowback and produced waters can have total dissolved solids (TDS) several times higher than those of seawater (Haluszczak et al., 2013), and recent

management practices of waters from the Marcellus formation have had a discernible imprint on surface water compositions such as elevated levels of As, Sr, Se, and Br concentrations compared to background observations (Wilson and VanBriesen, 2012; Ferrar et al., 2013; Fontenot et al., 2013; Olmstead et al., 2013; Warner et al., 2013; Wilson and Van Briesen, 2013). TDS values of flowback and produced waters from the Eagle Ford, which was the focus of this study, have been reported in the range of 40,346-144,952 mg/L (Blondes et al., 2014). While there is some published data of regulated trace elements in flowback and produced waters (Hayes, 2009; Chapman et al., 2012; Haluszczak et al., 2013), overall information about metal and metalloid concentrations mobilized from formations and the factors affecting the mobilization is limited.

Approximately 750 chemicals were listed as additives for hydraulic fracturing in a 2011 report to Congress (Waxman et al., 2011). However, most fluids contain less than 20 total additives (U.S. EPA, 2004). Additives can comprise 0.5-3% (wt/wt) of the fluid and include surfactants, scale inhibitors, co-solvents and acids (King, 2012). The compositions of hydraulic fracturing fluids are often tailored to specific formations and can be varied over different stages of well development. Despite this, there are common fluid properties and additive classes that can be considered across a spectrum of well and formation types (U.S. EPA, 2011).

Solid-water interactions have the potential to mobilize elements through a variety of pathways that depend on the formation composition and fracturing fluid chemistry. Dissolution of acid-soluble minerals may be a release pathway as strong acids (e.g., HCl) are often used to initiate fractures and are usually the single largest liquid additive in a fracturing fluid (Arthur et al., 2008; Gregory et al., 2011). Desorption of metals from host minerals can occur due to changes in pH and through the introduction of complexing agents. EDTA and citrate, both used

for iron control, form strong complexes with several metals and metalloids, such as Pb(II), Cu(II), Co(II), which can increase their mobility (Huang et al., 1995). Further, dissolved oxygen and other oxidative fluid additives (e.g. ammonium persulfate, magnesium peroxide) that are used to promote the breakdown of gel polymers (Vidic et al., 2013), may drive significant redox sensitive geochemical reactions. For example, oxidation of reduced forms of uranium and chromium typically increases their solubility (Rai et al., 1989; Wu et al., 2007).

The objectives of this study were to examine the impact of aqueous chemistry on the mobilization of metals and to investigate the dominant mobilization pathways during solid-water interactions involving samples from hydraulically fractured formations. The study used samples from the Eagle Ford formation, a highly productive oil and natural gas play in south Texas. Experiments on the release of elements as a function of pH, oxidant level and solid:water ratio sought to advance the understanding of factors controlling the behavior of metals and metalloids during water-rock interactions. Such information is critical for managing potential aqueous waste streams that contain elements mobilized from the fractured rock.

3.2 Experiment Protocols

3.2.1 Materials

All chemicals were used as received from the vendors without further treatment. Solutions were prepared with ultrapure water (resistivity > 18.2 MΩ•cm). Glass volumetric flasks, beakers and bottles were acid-cleaned and rinsed several times with deionized water and ultrapure water prior to use. When pH adjustments were performed, hydrochloric acid (HCl) and sodium hydroxide (NaOH) of trace-metal grade were used (Fisher Scientific). For experiments

at high oxidant loadings, hydrogen peroxide (H_2O_2, 30 wt % solution, Sigma Aldrich) was used as a model oxidant.

A cylindrical sample with 1 cm in diameter and 2.5 cm in length (Figure S3.1) was collected from a core taken from a well at a depth of 5668 ft (1728 m) in the Eagle Ford formation that are the target of current fracking operations. Upon arrival in the laboratory, samples were stored and ground to powders with an agate mortar and pestle in the anoxic atmosphere of a glovebox filled with a N_2/H_2 mixture circulated over a heated Pd catalyst. Two powder samples (Sample 1 and Sample 2) from the same core and depth were used in the experiments. After grinding, Sample 2 was sieved to a size fraction of 53 – 106 μm and all of the Sample 1 powder was kept without sieving.

3.2.2 Solid Characterization

X-ray diffraction (XRD) with Cu Kα radiation (Bruker d8 Advance X-ray diffractometer) provided information on the mineralogy of the samples. Approximately 250 mg of powder sample was placed in aluminum sample holders with preferred orientation minimized by excessive sample agitation. The Bruker Topas Program was used to conduct quantitative analysis of multiphase mixtures by means of Rietveld analysis of the entire diffraction pattern (2θ ranged from 5 °to70 °). The lower detection limit of the Rietveld analysis is approximately 1 wt% (Madsen et al., 2001), which was sufficient to capture the pyrite available in the samples. Strong acid digestion (procedure in supplementary material) followed by inductively coupled plasma mass spectrometry (ICP-MS, Agilent 7500ce) was performed for elemental composition analysis. Extraction results of two USGS reference shale materials, by the same procedure, are listed in Table S3.1. The extractable portions for the elements of interest (Ca, Mg, Fe, As) were higher than 80%. The specific surface area of the powdered samples was measured by BET-N_2

adsorption (Brunauer et al., 1938) (Autosorb-1, Quantachrome Instruments). Total carbon (TC) and total inorganic carbon (TIC) were measured with a total organic carbon analyzer (TOC-LCPH with SSM-5000A, Shimadzu Corp.).

3.2.3 Batch Experiments

The mobilization of metals from the samples was studied in a series of batch experiments that explored a range of pH, oxidant conditions, and solid:water ratios (Table 3.1). All experiments were performed in duplicate at room temperature. Blank controls, without sample powders, were conducted, sampled and analyzed in parallel for all conditions evaluated. Reactions were initiated by the addition of sample into 100 mL ultrapure water to achieve a target solid:water ratio, which was 1 g/L in most experiments. The solid:water ratio was selected to eliminate potential transport limitations and to drive element mobilization. Suspensions were continuously mixed by magnetically stirring at 600 rpm. All batch reactors except for those probing anoxic conditions were loosely capped so that the suspension was open to the atmosphere. Reaction times of either 96 or 120 hours (Table 3.1) were used; in preliminary experiments, this time was found to be sufficient for most elements (Ca, Mg, Fe, Ba, U) to be released to stable concentrations that were no longer changing (Figure S3.2). Aliquots (10 mL) of suspension were sampled at 1, 4, 24, 48 and 96 (120) hours and filtered through 0.22 μm polyethersulfone (PES) membranes for aqueous phase analyses. The suspension pH was monitored throughout the course of experiments with a benchtop pH meter (Fisher Scientific Accumet XL15).

Table 3.1 Conditions and variables explored in the experiments performed

Exp. No.	Sample Number	Reaction time (h)	pH	Final pH [a]	Redox condition	Solid:water ratio (g/L)
1	1	96	target pH 4	7.05	Atmospheric [b]	1
2			target pH 5	7.50		
3			target pH 6	7.61		
4			target pH 7	7.87		
5			target pH 8	7.95		
6			target pH 9	8.08		
7			target pH 10	8.37		
8	2	120	Unadjusted	8.20	Anoxic	1
9				8.26	1.5% H_2O_2	
10				8.19	3% H_2O_2	
11				8.18	1.5%+1.5% H_2O_2	
12	2	120	Unadjusted	8.62	Atmospheric [b]	1
13				8.69		2
14				8.55		10
15				8.30	Anoxic	10

[a] For Experiments 1-7, these are the suspension pH when the last samples were taken. They were different than target pH due to the buffering capacity of the carbonate mineral in the samples.
[b] "Atmospheric" means that the reactors were loosely capped to allow exchange with the air. Oxygen was the primary oxidant in this condition.

For investigation of pH (Experiments 1-7), either 0.1 M HCl or 0.1 M NaOH was intermittently added to the suspensions to adjust the pH to target values of 4 to 10. This approach of pH adjustment was selected as the samples had a strong buffering capacity (see discussion below). The final pH observed drifted considerably from the target value due to the buffering capacity of the sample (Figure S3.3). In investigating the effect of oxidizing conditions (Experiments 9-10), H_2O_2 was selected as a model oxidant to eliminate the generation of metals, metalloids or anions of concern from the additives that could interfere with the interpretation of the experimental results. The concentrations of H_2O_2 were selected to be in great excess of the oxidant demand exerted by organic carbon and pyrite in the samples thus driving the maximum extent of oxidation for those species that can be oxidized by H_2O_2. A portion of 10 mL or 5 mL

30% H_2O_2 solution was diluted to a total volume of 100 mL with ultrapure water to obtain 3% or 1.5% H_2O_2 concentration prior to the addition of sample powders. In Experiment 11 the reaction started with 1.5% H_2O_2 and a second 5-mL aliquot of 30% H_2O_2 solution was added 24 hours later to give a total added H_2O_2 concentration of 3%. In Experiments 13 and 14, two elevated solid loadings (2 and 10 g/L) were used to investigate the effect of solid:water ratio on element release to solution.

Experiment 8 at anoxic conditions was conducted with 100 mL serum bottles (Figure S3.4). The ultrapure water loaded into the bottles was first bubbled with ultrapure N_2 that contained 400 ppm CO_2 (N_2/CO_2 gas) for at least 30 minutes. For the experiment a 50 mL suspension prepared with that water was used, and the serum bottle headspace was replenished with a continuous flow of the N_2/CO_2 mixture. The presence of CO_2 in the headspace that was equivalent to that of the atmosphere resulted in dissolved inorganic carbon (DIC) and pH of the suspensions that were comparable to those in the other experiments. The dissolved oxygen level as determined with a dissolved oxygen microprobe (Ocean Optic Neofox system) was measured to be below 0.5 mg/L. Due to the limited suspension volume, no samples were taken during the 120-hour experiment and a single 10 mL sample was collected and filtered at the end of the experiment.

3.2.4 Analytical Methods

A portion of the filtrate was acidified and analyzed for concentrations of dissolved metals (Ca, Mg, Fe, Ba, U, Pb, Cr) and metalloids (As, Sb) by ICP-MS (Agilent 7500ce with a quadruple mass analyzer). The detection limits for major elements (Ca, Mg, Fe) were 0.01 mg/L, and for trace elements (Ba, As, U) were 0.1 µg/L. The ranges of calibration standards were 0.1- 10 mg/L for major elements and 0.1 – 100 µg/L for trace elements. Another portion of

the filtrate was analyzed for sulfate by ion chromatography (881 Compact IC pro, Metrohm USA Inc.). The electrical conductivity (EC) of the suspensions in Experiments 8-15 was measured with a conductivity meter (ECTestr11, Eutech Instruments).

3.2.5 Chemical Equilibrium Modeling

Chemical equilibrium modeling was used to evaluate whether the solutions had compositions that were controlled by equilibration with specific solid phases. The general approach was to solve for equilibrium based on mole balance equations, charge balance, and a set of equilibrium reactions (Nordstrom et al., 1990) (Table S3.2). Equilibrium compositions were solved using both spreadsheet-based calculations and the software program MINEQL+ v 4.6 (Schecher and McAvoy, 2007). In MINEQL and for spreadsheet (Microsoft Excel) approaches, activity coefficients were determined using the Davies equation (Table S3.2). It should be noted that the approach for activity correction used are valid for the ionic strength values (below 0.05 M) observed in this study (Table S3.2), but other approaches (such as Pitzer equations) may be appropriate for solutions with higher ionic strengths (He et al., 2014).

3.3 Results and Discussion

3.3.1 Core Sample Composition.

Mineral and elemental compositions of the two core samples were very similar. Based on XRD measurements (Figure S3.5), carbonates (calcite, dolomite, and ankerite) are the dominant phases (74.6 - 77.9 wt %) in both samples. Other minerals included quartz, clay minerals (kaolinite), feldspar (albite) and a small amount of pyrite (1.3 – 1.9 wt %). Quantitative XRD

analysis (Table 3.2) agrees well with the major element compositions (Ca, Mg and Fe) of the sample. The relative richness of TOC, carbonates, quartz and clay minerals are consistent with other studies of the Eagle Ford formation (Mullen, 2010; Harbor, 2011; Sondhi, 2011; Kearns, 2012).

The solid digestion results (Table 3.3) indicated that both samples were rich in calcium (25.4% for Sample 1 and 29.2% for Sample 2), corresponding to 63.5% and 73.0% calcite by mass. Other major elements included magnesium (2.3%) and iron (1.0 - 1.1%). The contents of some regulated trace elements (e.g., Cr was 15.9 mg/kg in Sample 1 and 36.1 mg/kg in Sample 2) were lower than their average crustal abundance (83 mg/kg for Cr), while other elements of concern were higher than their crustal average (e.g., As has a crustal average of 1.7 mg/kg while the samples had concentrations of 24.6 and 25.7 mg/kg) (Taylor, 1964). The abundances of major and trace elements in Sample 1 and Sample 2 are also compared with other reported literature values for Eagle Ford samples (Table 3.3).

Samples 1 and 2 had comparable physical and chemical properties (Table 3.3). Despite the difference in particle size distribution, the specific surface areas (3.5 m^2/g for Sample 1 and 3.6 m^2/g for Sample 2) were almost identical. TIC content (70.7 mg/g for Sample 1 and 85.0 mg/g for Sample 2) was consistent with the numbers estimated from the mass fractions of carbonate mineral as determined by quantitative XRD analysis (Table 3.2). In another study of Eagle Ford formation properties, TIC was also observed to have a positive linear relationship with Ca content (Kearns, 2012). The total organic carbon (TOC) content, determined as the difference between TC and TIC, was 48.6 mg/g (4.86%) for Sample 1 and 44.8 mg/g (4.48%) for Sample 2. These numbers are consistent with the elevated organic matter content in the Eagle Ford Formation as a proven hydrocarbon source rock (Harbor, 2011).

Table 3.2 Quantitative XRD analysis of core samples compared with reported ranges of Eagle Ford sample properties

Mineral	Chemical formula	Molecular Weight	Mass Fraction Sample 1[a]	Mass Fraction Sample 2[a]	Mass Fraction (Harbor 2011)[e]
Calcite	$CaCO_3$	100.1	0.5695	0.5830	0.03-0.92
Quartz	SiO_2	60.1	0.1142	0.0997	0.02-0.40
Dolomite	$CaMg(CO_3)_2$	184.4	0.0813	0.1257	0.01-0.04
Ankerite	$CaFe_{0.2}Mg_{0.8}(CO_3)_2$	190.4	0.0952	0.0703	0.01-0.06
Kaolinite	$Al_2Si_2O_5(OH)_4$	258.2	0.0633	0.0609	0.03-0.80
Albite	$NaAlSi_3O_8$	263.0	0.0571	0.0470	
Pyrite	FeS_2	120.0	0.0194	0.0134	0.01-0.05
SUM			1.0000	1.0000	
Criteria of fit [b]	**R_{wp} (%)**		14.30	15.65	
	R_p (%)		11.05	12.27	
	GOF		2.56	2.75	

	Mass Fraction Predicted [c]		Mass Fraction Experimental [d]	
	Sample 1	**Sample 2**	**Sample 1**	**Sample 2**
Calcium	0.2655	0.2753	0.2538	0.2917
Magnesium	0.0202	0.0235	0.0227	0.0230
Iron	0.0147	0.0104	0.0114	0.0103
TIC	0.0909	0.0952	0.0707	0.0850

[a] These values were from quantitative XRD analysis by the Bruker Topas program. TOC amounts of up to 5% were not considered in the mass fractions presented here, which only correspond to the inorganic mineral component of the samples. After grinding Sample 1 was kept without sieving and Sample 2 was sieved to a size fraction of 53-106 μm.

[b] Criteria of fitting used here include: "R-weighted pattern", R_{wp}; "R-pattern", R_p; "Goodness of fit", GOF.

[c] Predicted values are those that would result if the minerals determined by XRD were the only phases contributing Ca, Mg, Fe, and inorganic carbon.

[d] Experimental values are from acid digestion and inorganic carbon analysis (Table 3.3).

[e] Reported ranges of values for comparison.

Table 3.3 Physical and chemical properties of core samples compared with reported ranges of Eagle Ford sample properties

	Sample 1[a]	Sample 2[a]	(Kearns, 2012)[c]	(Harbor, 2011)[c]	(Sondhi, 2011)[c]
Major Element (in percentage)					
Calcium	25.38 ±0.56	29.17 ±0.55	1.66-34.83	0.31-38.48	
Magnesium	2.27 ±0.03	2.30 ±0.07	0.09-5.04	0.00-1.04	
Iron	1.14 ±0.03	1.03 ±0.01	0.29-4.79	0.18-4.53	
Trace element (in mg/kg)					
Aluminum	4090.0 ±260.7	3864.3 ±285.3	400-7514	4200-181600	
Potassium	1050.1 ±16.9	1035.7 ±58.7	100-2575	1300-28100	
Sodium	555.7 ±2.5	402.3 ±40.7		145-6160	
Manganese	178.8 ±1.0	191.5 ±3.2	110-790	0-387	
Vanadium	145.5 ±2.0	162.5 ±6.8	10.7-963.8	54-494	
Zinc	123.0 ±20.4	350.2 ±40.2	1.0-419.5	82-246	
Nickel	64.1 ±1.2	60.4 ±0.7	0.0-355.2	9-196	
Barium[b]	47.5 ±4.6	57.9 ±1.5		92-513	
Molybdenum	44.3 ±0.7	41.4 ±0.7	0.1-288.1	<1-118	
Copper	37.5 ±0.3	32.3 ±1.5	0.4-92.7	<10-114	
Arsenic	24.6 ±0.6	25.7 ±1.5			
Chromium	15.9 ±0.7	36.1 ±3.4	3.9-134.4	21-181	
Lead	11.5 ±0.3	17.8 ±3.6		6-16	
Uranium	5.7 ±0.0	6.9 ±0.1	0.0-26.5	<1-73	
Physichemical properties					
Total organic carbon (%)	4.86 ±1.95	4.48 ±0.80	0.763-6.356	0.53-11.80	0.06-6.32
Total inorganic carbon (%)	7.07 ±0.49	8.50 ±0.48	3.357-11.971		
Specific surface area (m^2/g)	3.5	3.6			

[a] Expressed as average ± standard deviation of triplicate analyses

[b] Barium recovery from the solid during solid digestion was incomplete, so these values do not represent the total Ba content of the samples.

[c] Reported ranges of values from literature for comparison.

3.3.2 Summary of Mobilization Results

The following discussion focuses on the aqueous concentrations of Ca, Mg, Fe, Ba, As, U either because they are major elements (Ca, Mg, Fe) that affect the fate of other elements or because they are regulated trace elements (Ba, As, U) with known toxicity and public health implications (U.S. HHS, 2003; U.S. EPA, 2010). Other regulated trace elements (Cu, Pb, Cr) that were below detection limits throughout the experiments, are not discussed. The leaching of Ca and Ba were controlled by equilibrium with solid phases (calcite, barite), while kinetic limitations in reaction rates play a more important role in other constituents such as As, Mg, sulfate.

3.3.3 Effects of Solution pH

The solid suspensions used in batch reactors exhibited a strong buffering capacity due to the high calcite content of the samples. After each manual adjustment targeting a specific pH value, the solution pH drifted back towards the value for calcite equilibrium (Figure S3.6). The final pH range (7.0-8.4) was much narrower than the target pH range (4-10); however, there was good correlation between the final pH and the target pH values (Figure S3.3), which corresponds to the amount of acid or base added. The total acid-neutralizing capacity of the samples was found to be 8.2 mmol acid per gram solid in a strong acid titration of a 1 g/L suspension (Sample 1) to pH below 4.0 (Figure S3.7). High buffering capacity from the high carbonate mass fraction indicates that, for the Eagle Ford formation, initially acidic hydraulic fracturing fluids could flow back with neutral or even higher pH values depending on fluid residence times.

Acid or base pH adjustments, aimed at targeted pH values, of the core sample suspensions significantly affected the mobilization of many metals. In general, higher releases of elements (Ca, Mg, Fe, Ba, As) were observed with more acid addition (Figure 3.1). This

effect was most evident for major elements. At the lowest final pH of 7.0, the dissolved Ca concentration was as high as 165 mg/L, which accounts for approximately 65% of the total Ca in the original solids; while at the highest final pH of 8.4, the Ca concentration was only 3 mg/L. Similarly, about 60% of total Mg was mobilized at the lowest target pH and less than 1% at the highest pH. Trace element release was somewhat affected by pH. Arsenic concentrations were higher at lower pH, and slightly higher U concentrations occurred between final pH values of 7.6-7.9. However, the concentrations of both As and U remained low (0 – 5.0 μg/L for As and 0 – 1.1 μg/L for U) throughout the experiments.

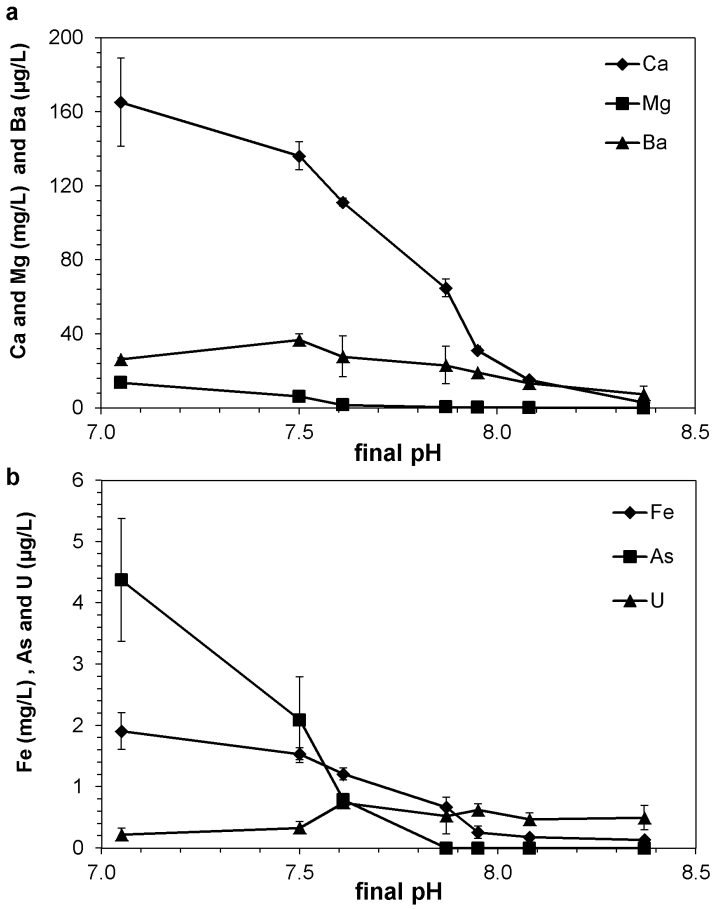

Figure 3.1 Final aqueous concentrations of (a) Ca, Mg, Ba and (b) Fe, As, U after 96 hours of reaction with pH adjustment (Experiments 1-7). Experiments were performed at room temperature with 1 g/L shale loading. Data are shown as the average of the duplicates with the error bars being the standard deviations.

Ca release is correlated with the mobilization of many other elements (Figure 3.2) as calcium carbonate readily hosts (and thus can release) other divalent cations (Mg, Ba, Fe). The relationship between the concentration of an individual element and that of calcium can be the result of more than one factor. Final Fe concentrations were positively correlated with Ca concentrations in Experiments 1-7, which could be partially attributed to the common phenomenon of Fe(II) substitution for Ca in calcite (Reeder, 1983) and the presence of ankerite [$CaFe_{0.2}Mg_{0.8}(CO_3)_2$]. However, soluble Fe concentrations are also subject to the rate and extent of Fe(II)/Fe(III) redox reactions. As the rate of Fe(II) oxidation to Fe(III) by oxygen increases with increasing pH, oxidation of Fe(II) followed by precipitation of Fe(III) may occur at higher pH values (Crittenden et al., 2012). The higher iron concentrations in anoxic conditions relative to open and oxidative systems (Figure 3.3) were a clear indication that iron oxidation and precipitation occurred in the presence of oxygen and/or H_2O_2. Note that the processes above could affect the soluble Fe concentrations simultaneously and yield the almost linear relationship between Fe and Ca concentrations in Figure 3.4. In contrast, Mg concentrations were observed to follow a different linear trend with Ca concentrations at different pH regions, with a larger slope observed at lower pH values. This is consistent with previous studies that dolomite dissolution rates decrease with increasing pH (Pokrovsky et al., 1999; Pokrovsky and Schott, 2001). In addition, the presence of dissolved Ca could also strongly inhibit dolomite dissolution above pH 7 (Pokrovsky and Schott, 2001).

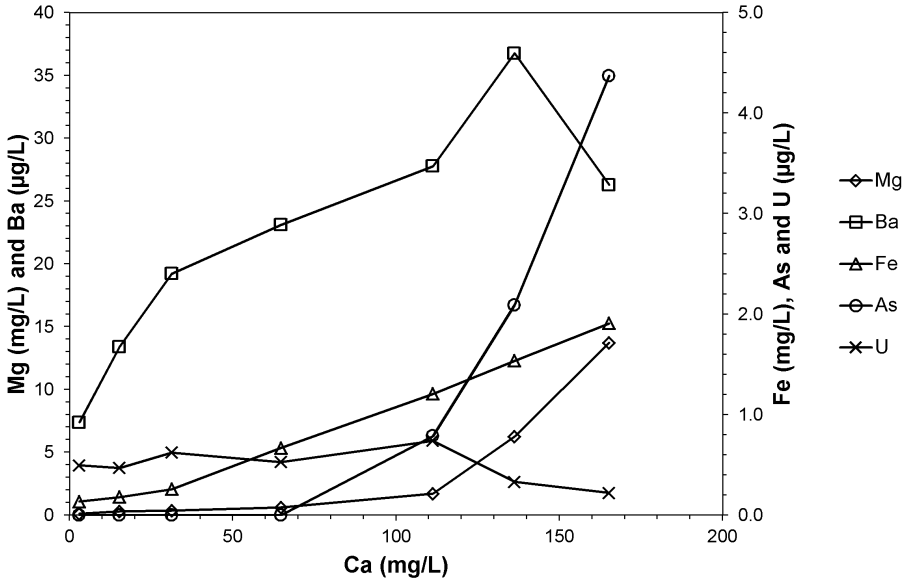

Figure 3.2 Relationship between the final aqueous concentrations of Mg, Ba, Fe, As and U and the final Ca concentrations in experiments with pH adjustment (Experiments 1-7). Experiments were performed at room temperature with 1 g/L shale loading. Data are shown as the average of the duplicates.

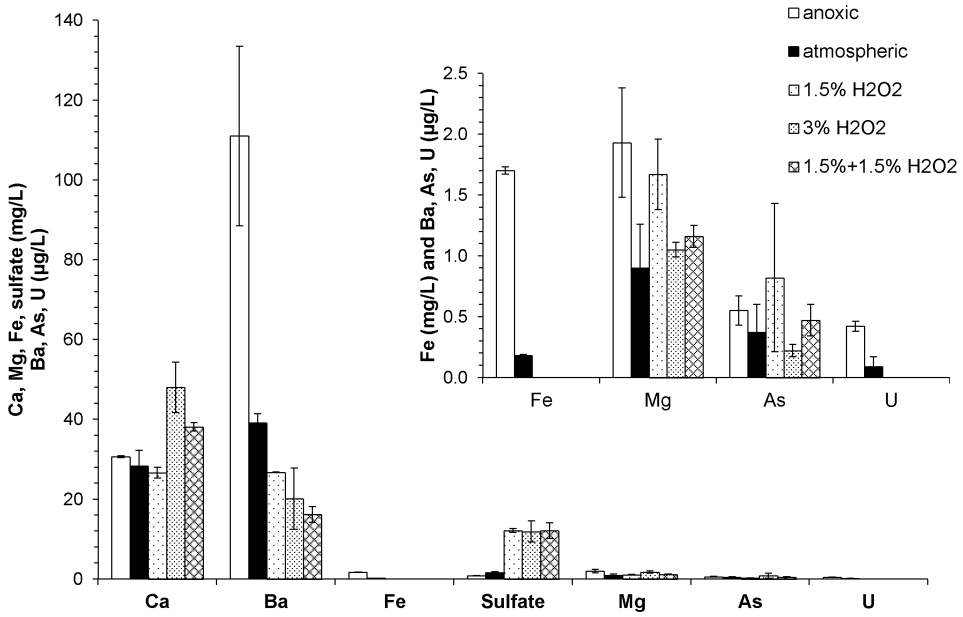

Figure 3.3 Metal and sulfate mobilization after 120 hours of reaction under anoxic (Experiment 8), atmospheric (Experiment 12) and oxidative conditions (Experiment 9-11). Experiments were performed at room temperature with 1 g/L shale loadings. A 1.5% (3%) H_2O_2 solution was prepared fresh for groups marked with 1.5% (3%) H_2O_2. The 1.5%+1.5% H_2O_2 group started with 1.5% H_2O_2, and was reacted for 24 hours before the addition of another 1.5% H_2O_2 (3% total H_2O_2 concentration thereafter). Data are shown as the average of the duplicates with error bars being the standard deviations. The Fe and U concentrations with H_2O_2 were below detection limits. The atmospheric and oxidative condition experiments were open to the laboratory atmosphere, and the anoxic experiments had headspaces with 400 ppm CO_2.

A comparison between predicted calcite equilibrium and experimental data supported calcite dissolution as the dominant pathway for Ca^{2+} mobilization. Results from Experiments 1-7 were compared with equilibrium calcite solubility in open and closed systems (Figure 3.4). Experimental measurements generally agreed with predicted equilibrium for a system closed with respect to atmospheric exchange. Although the batch reactors were loosely capped, the rate of CO_2 exchange between the suspension and atmosphere could have been slower than that of the acid-base reaction from the pH adjustment, especially in lower pH region (pH<4) where CO_2 effectively acts as an inert gas (Hoover and Berkshire, 1969), thus leading to system behavior which is closer to a closed system. Without pH adjustment, calcite dissolution was predicted to equilibrate at pH 8.23 with 18.7 mg/L Ca in the open system and at pH 9.9 with 4.4 mg/L Ca in a closed system according to equilibrium calculations (Figure 3.4). Data from Experiments 8-15 (i.e., those with no pH adjustment) were all close to the model predictions for an open system.

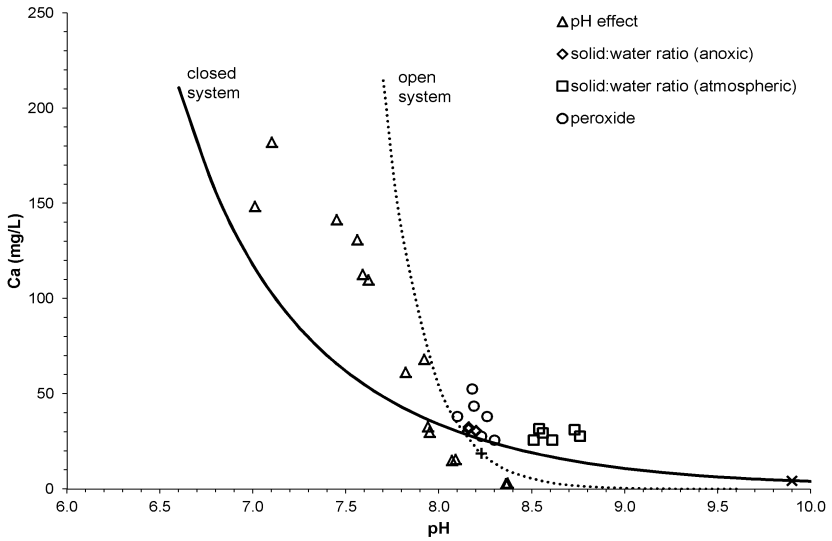

Figure 3.4 Comparison of measured and predicted solution compositions based on calcite equilibrium. Predictions are shown as lines for a system with calcite open to an atmosphere with a CO_2 partial pressure of $10^{-3.46}$ atm (dashed line) and for a system closed with respect to exchange with the atmosphere (solid line) for systems to which acid or base had been added to yield the pH range shown. The predicted pH and calcium concentrations without acid or base addition are shown as the + and x for the open and closed system, respectively. The other markers (open triangle, diamonds, squares and circles) are data from different experiments.

3.3.4 Oxidant Level Effect

Compared with experiments open to the atmosphere, the lack of oxygen in anoxic environments prevents a number of oxidative pathways (Figure 3.3). Monitoring of the pH indicated that the use of the N_2/CO_2 gas sparging and headspace allowed for DIC and pH levels in anoxic experiments that were comparable to those under atmospheric conditions. Ca concentrations were similar with or without oxygen since calcite dissolution is independent of redox conditions. Experiments with H_2O_2 had pH values that were 0.4 – 0.6 units lower than those without H_2O_2 (Figure S3.8), which could explain the slightly higher final Ca concentrations in experiments with a 3% final H_2O_2 concentration. The decrease in pH was likely a result from pyrite oxidation and/or precipitation of $Fe(OH)_3$.

The sensitivity of sulfate concentration to the presence of oxidants suggests that pyrite was being oxidized. After 120 hours, sulfate concentrations were 0.8 mg/L under anoxic conditions and 1.6 mg/L under atmospheric conditions. Further, the addition of 1.5% H_2O_2 generated 11.3 mg/L (118 μM) more sulfate than observed for anoxic conditions. H_2O_2 concentrations (1.5% and 3%) used in the experiments were selected so that they would be in great excess (more than 30-fold) of the oxidant demand exerted by the observed levels of organic carbon and pyrite in the samples. The sulfate released in the anoxic experiment could represent the original amount of sulfate present (0.8 mg SO_4^{2-}/g sample), while the additional 11.3 mg/L sulfate produced in the presence of H_2O_2 represents the amount of oxidizable sulfur (3.8 mg S/g sample) in the solids that could be mobilized within 120 hours. This amount of oxidizable sulfur is 53% of the amount of sulfur in the sample from the pyrite abundance determined from quantitative XRD (7.1 mg FeS_2–S/g sample). Because the measured mass fraction of pyrite (1.3% in Sample 2) was close to the detection limits of the Rietveld refinement, this

inconsistency might be caused by the uncertainty in the pyrite amount that influenced the estimated sulfate amount that could be produced.

Reactions (3.1) and (3.2) show the complete oxidation of both iron and sulfur in pyrite upon exposure to oxygen or H_2O_2. The expected decrease in pH from proton generation as shown in Reactions (3.1) and (3.2) would be significant if there were no other minerals with buffering capacity such as carbonate. The mole ratio of calcite to pyrite that represents complete neutralization is 4:1 (Chermak and Schreiber, 2013) according to Reactions (3.3) and (3.4). The Eagle Ford samples used in this study contained calcite in great excess compared to pyrite (mole ratio = 52.2 :1), effectively stabilizing the pH of the systems.

$$FeS_2 + 15/4\ O_2 + 7/2\ H_2O \rightarrow Fe(OH)_{3(s)} + 2SO_4^{2-} + 4\ H^+ \quad (3.1)$$

$$FeS_2 + 15/2\ H_2O_2 \rightarrow Fe(OH)_{3(s)} + 2SO_4^{2-} + 4\ H^+ + 4\ H_2O \quad (3.2)$$

$$FeS_2 + 4CaCO_3 + 15/4\ O_2 + 7/2\ H_2O \rightarrow Fe(OH)_{3(s)} + 2SO_4^{2-} + 4\ Ca^{2+} + 4\ HCO_3^- \quad (3.3)$$

$$FeS_2 + 4CaCO_3 + 15/2\ H_2O_2 \rightarrow Fe(OH)_{3(s)} + 2SO_4^{2-} + 4\ H_2O + 4\ Ca^{2+} + 4\ HCO_3^- \quad (3.4)$$

Barium concentrations were negatively correlated with sulfate concentrations, which in turn were affected by the oxidant level of the system (Figure 3.3), suggesting that Ba mobilization was controlled by barium sulfate ($BaSO_4$) solubility. $BaSO_4$was not initially present in the samples but rather precipitated as a secondary phase while barium and sulfate likely leached from different sources. This has been further proved by the modeling results that $BaSO_4$ solubility is not influenced by pH, and all experimental data (i.e., the ion activity product for barium sulfate) stayed within one order of magnitude of the predicted equilibrium solubility (Figure S3.9). In anoxic experiments, which had similar pH profiles to those open to the atmosphere, the Ba concentration reached a maximum of 111 μg/L. This value would be equivalent to at least 111 mg/kg barium in the solid, which was higher than the value determined

by solid digestion (57.9 mg/kg in Sample 2). The solid digestion did not recover the entire Ba content of the core sample as Ba released from initial host phases (e.g., substituted in calcite) precipitates as $BaSO_4$ with the sulfate produced during the digestion.

Soluble As and U concentrations remained low at all oxidant levels (only up to 3% for As and 7% for U release observed), and below EPA maximum contaminant levels (MCL) of 10 μg/L and 30 μg/L in drinking water (U.S. EPA, 2009). This is possibly due to their relatively low amounts in the original solid sample and potential for (re)sorption processes with solid particles in suspension.

3.3.5 Solid:Water Ratio Effect

The solid:water ratio affected the mobilization of different elements to varying degrees (Figure 3.5). Ca concentrations were relatively independent of solid loadings because, as mentioned, they were primarily controlled by calcite dissolution equilibrium. Mg and Ba concentrations were higher at elevated solid:water ratios, but the increase was not linear. The non-linearity may be due to different rates of dissolution of specific phases (e.g., dolomite versus calcite) that host these elements as well as potential inhibition of Mg release from dolomite with increasing Ca concentrations (Pokrovsky and Schott, 2001). Soluble Ba concentrations were directly related to the abundance of available sulfate. Sulfate concentrations were much higher at the highest solid:water ratio of 10 g/L. Amounts of sulfate that were directly dissolved from the solid (8.9 mg/L) and produced from oxidation of reduced sulfur sources (4.8 mg/L) were both greater at a 10 g/L solid:water ratio than those (0.8 mg/L and 0.8 mg/L) at 1 g/L loading (Figure S3.10). Compared to the quantitative XRD results, all pyrite was not oxidized in open systems (having available oxygen). This incomplete sulfur oxidation could be the result of slow oxidation rate of pyrite by oxygen alone. Ca concentrations, independent of solid:water ratios,

and higher sulfate, at elevated solid:water ratios, were also observed under anoxic conditions (Figure S3.10).

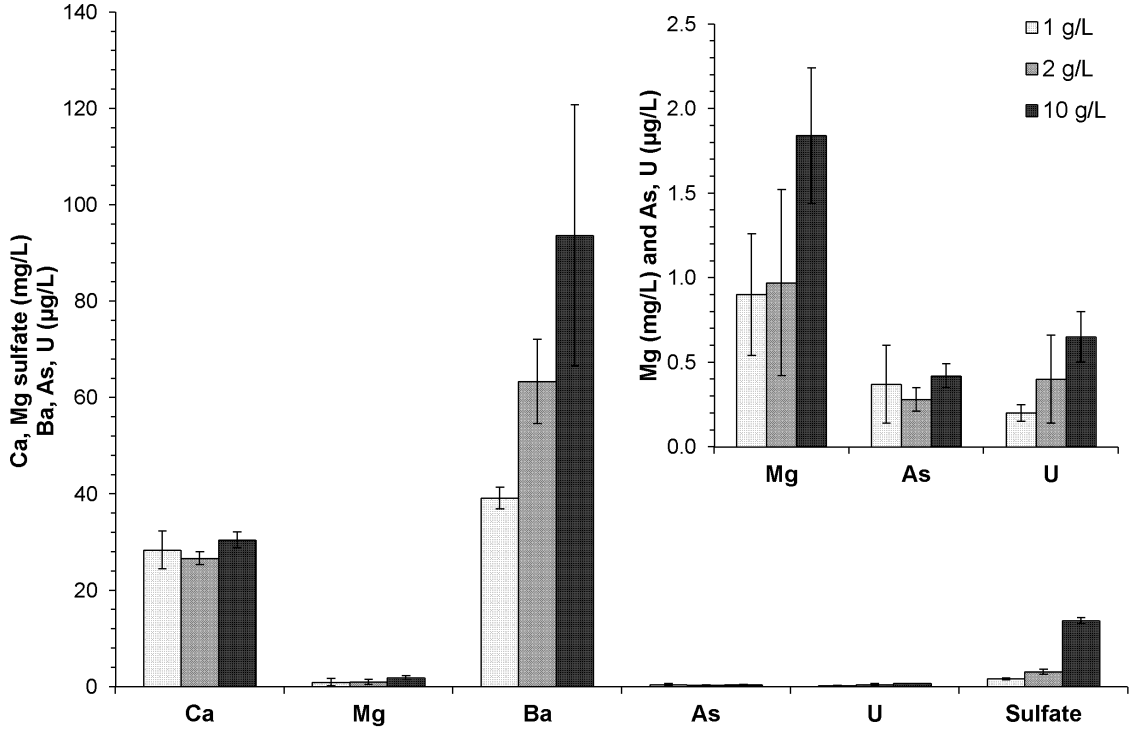

Figure 3.5 Metal and sulfate mobilization with different solid:water ratios (1, 2, 10 g/L) after 120 hours of reaction. Experiments were performed at room temperature and open to the atmosphere. Data are shown as the average of the duplicates with error bars being the standard deviations.

Electrical conductivity (EC) of suspensions remained relatively stable regardless of the solid:water ratio (Figure S3.11) as the aqueous phase composition was largely controlled by calcite dissolution. Measured EC could also be used to estimate the TDS (108-126 mg/L) based on the relative concentrations of the major cations and anions present (Table S3.3). The reported produced water TDS level in Eagle Ford Formation is 40,346-144,952 mg/L (Blondes et al., 2014), which is higher than typically observed in this study. This difference can be attributed to an elevated rock:water ratio and longer contact times. Previous work has shown that TDS of

flowback waters increases with time in the 30 days after hydraulic fracturing ceased (Kimball, 2012; Barbot et al., 2013).

3.4 Conclusions

Understanding element release from shale materials exposed to various water chemistries will aid in managing wastewaters from hydraulic fracturing operations. For the Eagle Ford samples used in this study, the release of elements strongly depended on pH, which was primarily controlled by carbonate dissolution. High Ca concentrations and potential precipitation of $BaSO_4$ will likely impact system-wide scaling. The introduction of oxygen and other oxidants could significantly increase the amount of sulfate over time when pyrite is available. When coupled with bioavailable dissolved organic carbon, the growth of sulfate-reducing bacteria could potentially result in biofouling/biofilm formation and the production of unwanted reduced sulfur species (Kirk et al., 2012; Murali Mohan et al., 2013; Cluff et al., 2014). For these Eagle Ford formation core samples, the trace elements (As, U and Ba) mobilized from rock-fluid contact will probably not affect the choice of strategies for management of produced waters.

The degree to which the findings from this study can be related to flowback from the Eagle Ford Formation will be a function of the parameters used in actual operations and subject to the complicated subsurface conditions. For example, while calcite solubility decreases with elevated temperature in subsurface, Na^+, Mg^{2+} ions present in formation brine could significantly increase calcite solubility due to their incorporation into calcite lattice (Plummer and Busenberg, 1982; He and Morse, 1993). The solid:water ratio in the field will depend on the fracture network (10,000's to 100,000's g/L for overall porosities in the range of 1-10%), however, the

rock-fluid interactions will occur at both fractured surfaces and the mobilized particles-fluid interfaces, thus the total reactive surface area will be a more relevant property to scale up the extent of mobilization. As flowback resident times can reach up to several weeks (Vidic et al., 2013), the flowback volumes can decrease with increasing TDS due to mixing with formation water (Kimball, 2012). Moreover, similar responses of element mobilization towards the addition of acid or base are more likely to apply to carbonate-rich formations while the presence of barium in a pyrite-rich formation might predict the precipitation of barite as a secondary phase and the subsequent scaling as a potential problem for well performance. For these Eagle Ford samples, the dominance of carbonate minerals suggests that the buffering of strong acids could last for very long times, however, the acidic fracturing fluids will not interact with the entire formation and their action to initiate fractures can be limited to the zone immediately adjacent to the well.

Acknowledgements

This study was supported by research funding from the McDonnell Academy Global Energy and Environmental Partnership. The authors thank Ross Tomson from the Shale Water Research Center for providing the samples from the Eagle Ford Formation. Begüm Karakoçak and Andrew Martahus contributed to the experiments. Portions of this work were performed when Lin Wang was a visiting student research collaborator in the Department of Civil and Environmental Engineering at Princeton University. The authors thank Joseph Vocaturo, Lori Tunstall, John Higgins, Elizabeth Lundstrom, Yi Jiang and Jennifer Houghton for their assistance with experiments and analyses.

Chapter 3. Supporting Information

This supporting information includes 11 figures, 3 tables and text that facilitate the interpretation of the results in Chapter 3.

Strong acid digestion procedure

Experiments were performed in triplicate. Three portions of 200 mg sample powders were weighed and introduced into digestion tubes, and 8 mL concentrated HNO_3 and 2 mL concentrated HCl were added. The resulting suspensions were heated in a digestion block for 4 hours at 100±0.5 °C and cooled overnight. Ultrapure water was added to the digestate to give a total volume of 50 mL. Aliquots of 10 mL supernatant were then taken by syringes and filtered through 0.22 μm PES membranes. Serial dilution was performed for the filtrate before analysis by ICP-MS (Agilent 7500ce). By design this acid digestion method will dissolve almost all elements except for those bound in silicate structures. Complete dissolution of silicates would have required the use of hydrofluoric acid. However, based on comparison with extractions of reference shale materials, the acid digestion method mobilizes essentially all of the elements of interest in this study. If a total digestion is necessary, then EPA Method 3052 that uses concentrated nitric acid and hydrofluoric acid should be used.

The extraction results with this method of two standard reference shale materials from USGS are listed in Table S3.1. The certificates of analysis of these two reference materials can be found at http://crustal.usgs.gov/geochemical_reference_standards/

Table S3.1 Recovery of standard reference materials from strong acid digestion

	SGR-1b			SBC-1		
	Experiment [a]	Standard [b]	Extractable (%) [c]	Experiment [a]	Standard [b]	Extractable (%) [c]
Major elements (%)						
Ca	7.63 ±0.06	8.38 ±0.17	91.0	2.76 ±0.03	2.95 ±0.01	93.6
Mg	4.36 ±0.03	4.44 ±0.2	98.1	1.89 ±0.03	2.6 ±0.01	72.6
Fe	2.87 ±0.03	3.03 ±0.14	94.6	7.81 ±0.10	9.71 ±0.02	80.4
Na	0.512 ±0.004	2.99 ±0.13	17.1	0.052 ±0.001	0.15	34.8
K	0.223 ±0.003	1.66 ±0.1	13.4	0.48 ±0.01	3.45 ±0.01	14.0
Al	0.004 ±0.000	6.52 ±0.21	0.1	0.050 ±.001	21 ±0.04	0.2
Trace elements (mg/kg)						
As	57.74 ±0.51	67 ±5	86.2	26.23 ±0.19	25.7 ±0.7	102.1
Ba	223.16 ±2.01	290 ±40	77.0	381.22 ±6.16	788 ±7.7	48.4
Cd	0.56 ±0.01	0.9	62.8	0.18 ±0.01	0.4 ±0.02	45.4
Co	10.08 ±0.06	12 ±1.5	84.0	18.97 ±.30	22.7 ±0.3	83.6
Cr	27.54 ±0.40	30 ±3	91.8	45.25 ±0.78	109 ±1	41.5
Cu	62.15 ±0.69	66 ±9	94.2	28.10 ±1.40	31 ±0.6	90.7
Mn	228.50 ±1.53	267 ±34	85.6	1072.30 ±5.16	1162 ±7.7	92.3
Mo	31.60 ±0.29	35 ±0.9	90.3	2.48 ±0.45	2.4 ±0.07	103.5
Ni	30.46 ±0.20	29	105.0	75.67 ±1.20	82.8 ±0.8	91.4
Pb	41.28 ±1.37	38 ±4	108.6	27.24 ±0.66	35 ±0.3	77.8
Sb	2.27 ±0.05	3.4 ±.5	66.6	0.499 ±0.005	1.01 ±0.03	49.4
Se	3.52 ±0.19	3.5	100.5	1.71 ±0.34	NA	NA
U	3.88 ±0.09	5.4 ±0.4	71.9	2.22 ±0.03	5.76 ±0.11	38.6
V	104.58 ±0.59	130 ±6	80.4	81.17 ±1.24	220 ±1.4	36.9
Zn	125.42 ±1.94	74 ±9	169.5	234.03 ±6.22	186 ±1.7	125.8

[a] Values from the strong acid digestion described in this study.

[b] Values from USGS Certificates of Analysis determined by cooperating laboratories using a variety of analytical methods.

[c] Extractable (%) = Experiment / Standard

Table S3.2 Reactions and parameters used in chemical equilibrium modeling

Reaction	Log K	Reference
Mineral dissolution		
Calcite: $CaCO_{3(s)} \rightleftarrows Ca^{2+} + CO_3^{2-}$	-8.48	(Nordstrom et al., 1990)
Barite: $BaSO_{4(s)} \rightleftarrows Ba^{2+} + SO_4^{2-}$	-9.97	
Carbonate protonation		
$CO_{2(aq)} + H_2O \rightleftarrows H^+ + HCO_3^-$	-6.35	(Plummer and Busenberg, 1982)
$HCO_3^- \rightleftarrows H^+ + CO_3^{2-}$	-10.33	
CO_2 exchange		
$CO_{2(g)} \rightleftarrows CO_{2(aq)}$	-1.47	(Plummer and Busenberg, 1982)

Equations Used

Davies equation for activity coefficient corrections (for water at 25 ℃):

$$\log \gamma_{Davis} = -0.51 z^2 \left(\frac{I^{1/2}}{1 + I^{1/2}} - 0.2I\right)$$

For species I, $\{i\} = \gamma_{Davis,\,i}\,[i]$

Equilibrium reactions:

$H_2CO_3^* \rightleftarrows H_2O + CO_{2(g)}$ $\quad K_{H,CO2} = p_{CO2}/[H_2CO_3^*]$ *(for open system only)* (S3.1)

$H_2CO_3^* \rightleftarrows H^+ + HCO_3^-$ $\quad K_{a1,CO_2} = \frac{\{H^+\}\{HCO_3^-\}}{\{H_2CO_3^*\}} \rightarrow \{HCO_3^-\} = \frac{K_{a1,CO_2}\{H_2CO_3^*\}}{\{H^+\}}$ (S3.2)

$HCO_3^- \rightleftarrows H^+ + CO_3^{2-}$ $\quad K_{a2,CO_2} = \frac{\{H^+\}\{CO_3^{2-}\}}{\{HCO_3^-\}} \rightarrow \{CO_3^{2-}\} = \frac{K_{a1,CO_2}K_{a2,CO_2}\{H_2CO_3^*\}}{\{H^+\}^2}$ (S3.3)

$CaCO_{3(s)} \rightleftarrows Ca^{2+} + CO_3^{2-}$ $\quad K_{sp,CaCO_3} = \{Ca^{2+}\}\{CO_3^{2-}\}$ *(in presence of calcite only)* (S3.4)

Charge balance equation:

$[H^+] + 2[Ca^{2+}] = [OH^-] + [HCO_3^-] + 2[CO_3^{2-}] + [Cl^-]$

Mole balance equation:

for an open system, $[TOTCa]_{dissolved} = [Ca^{2+}]$

for a closed system, $[TOTCa]_{dissolved} = [Ca^{2+}] = TOTCO_3 = [HCO_3^-] + [CO_3^{2-}] + [H_2CO_3^*]$

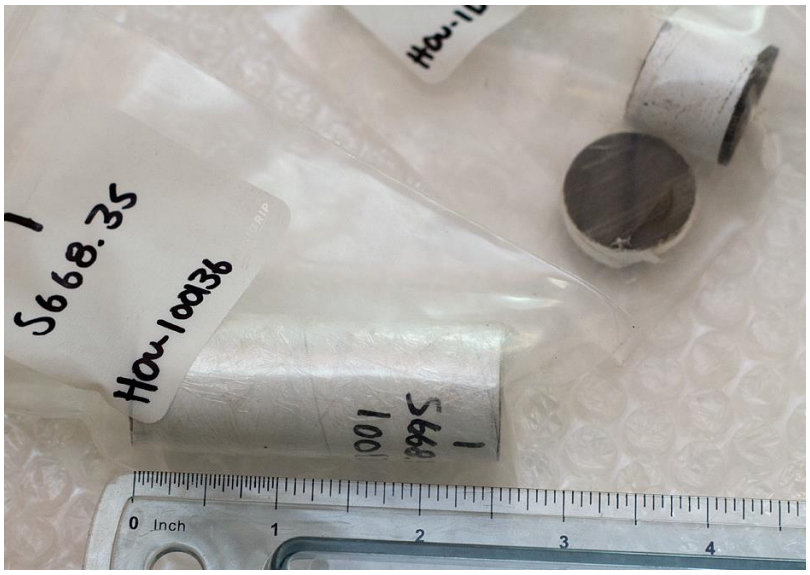

Figure S3.1 Image of samples from the Eagle Ford Formation

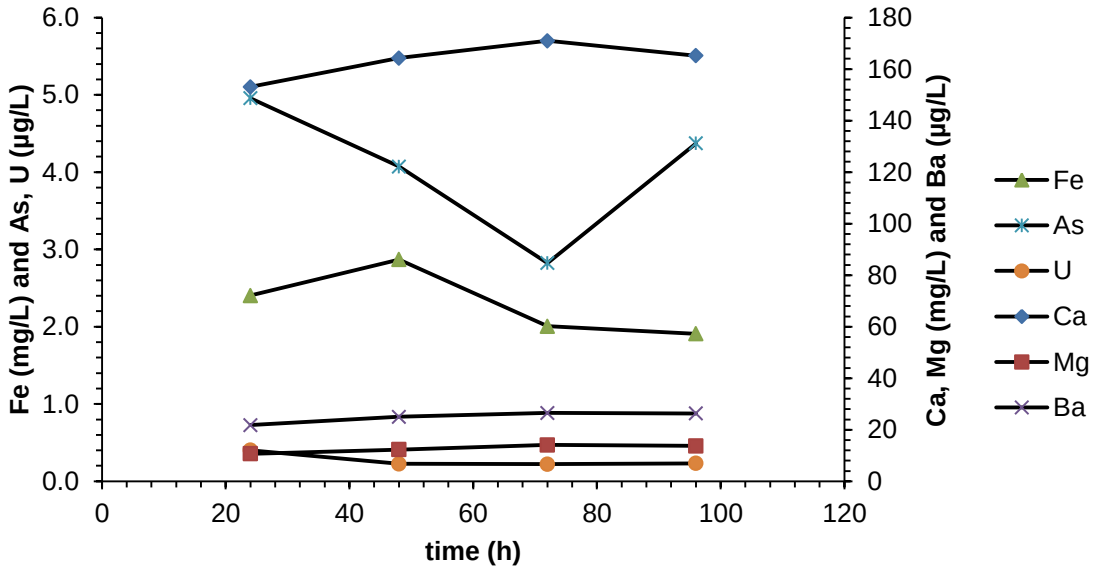

Figure S3.2 Element mobilization with time for Experiment 1 (target pH 4 and final pH 7.05). The concentrations of most elements (Ca, Mg, Ba, Fe, U) stabilized within 96 hours. Data points are presented as the average of the duplicates. The trend with time for other experiment conditions was similar to this one.

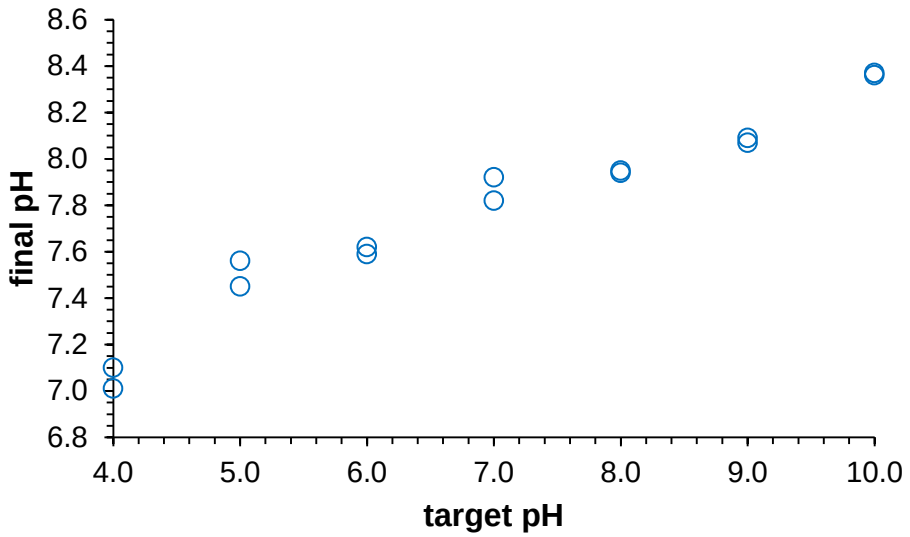

Figure S3.3 Relationship between the final pH and the target pH after 96 hours in Experiments 1-7. Manual adjustment of pH was achieved by monitoring pH and periodically adding 0.1 M HCl or NaOH. Shale loadings were 1 g/L for all batch reactors. Data are shown for duplicates.

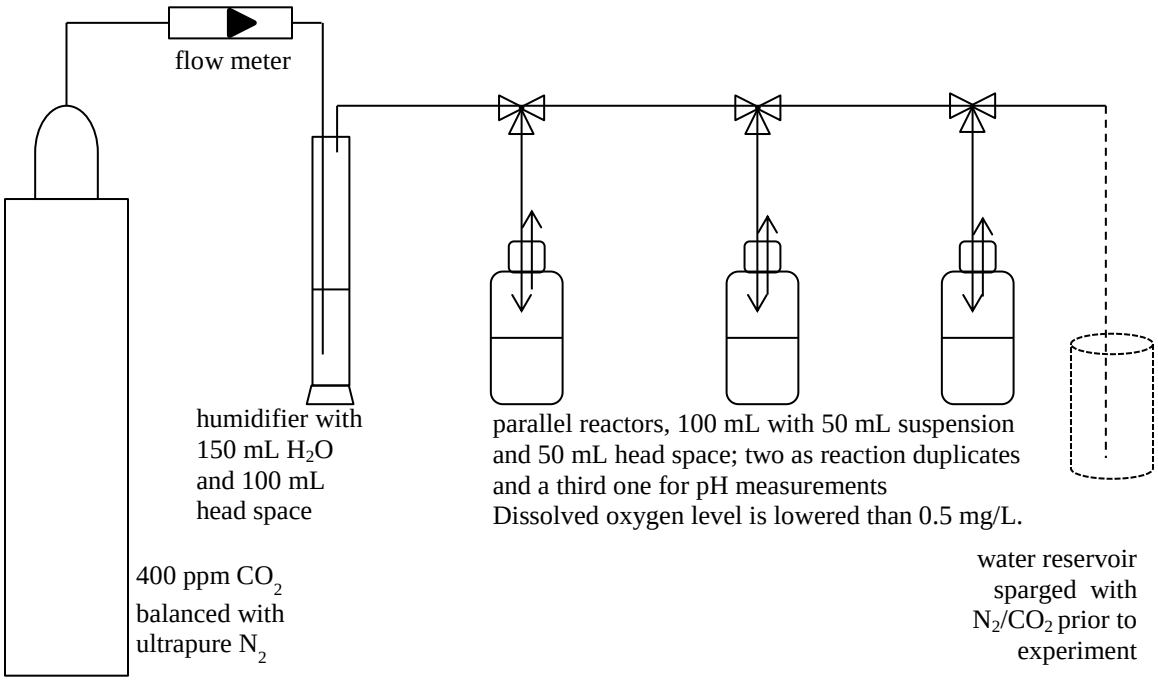

Figure S3.4 Illustration of setup for performing experiments at anoxic conditions

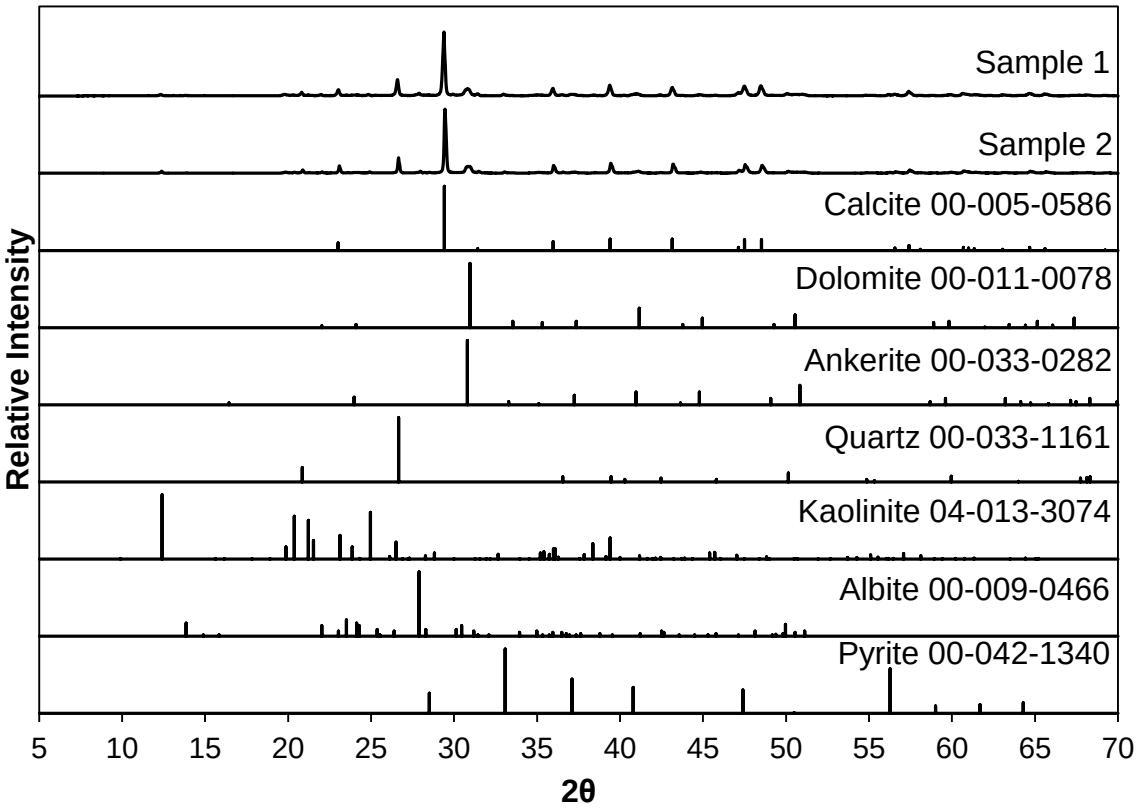

Figure S3.5 Powder X-ray diffraction (XRD) patterns of samples. The reference patterns of seven minerals from the International Centre for Diffraction Data database are shown for comparison.

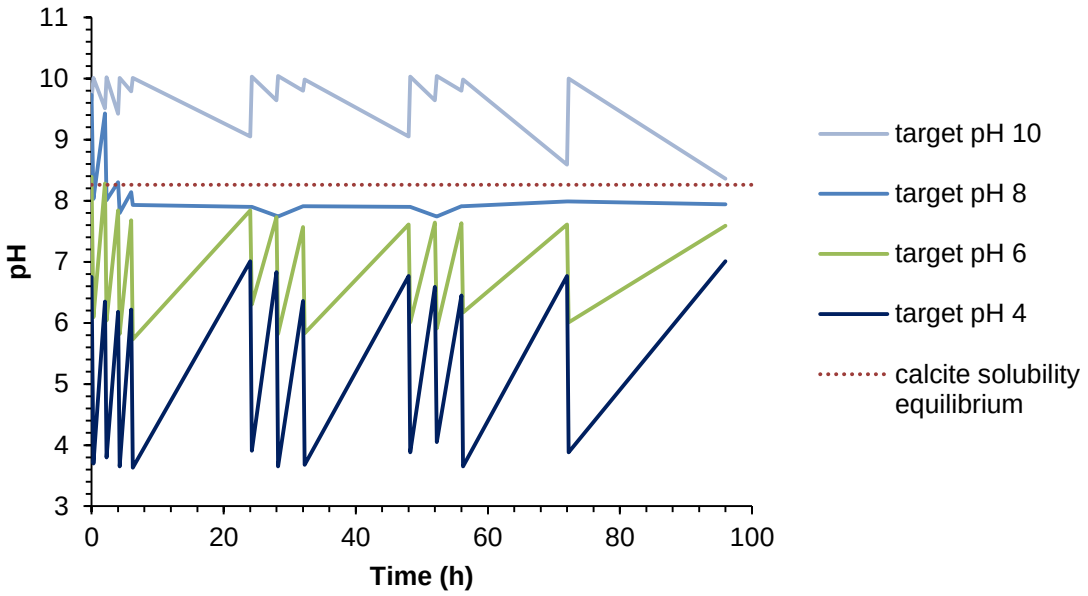

Figure S3.6 pH drift during manual adjustment. The red dotted line is the calculated calcite dissolution equilibrium in an open system ($p_{CO2} = 10^{-3.46}$ atm) without addition of acid or base. The pH of the suspension tended to return to pH 8.3 (marked by dashed line) that corresponds to the equilibrium pH of calcite dissolution in a closed system. This indicates that calcite dissolution dominates Ca mobilization and the solution pH.

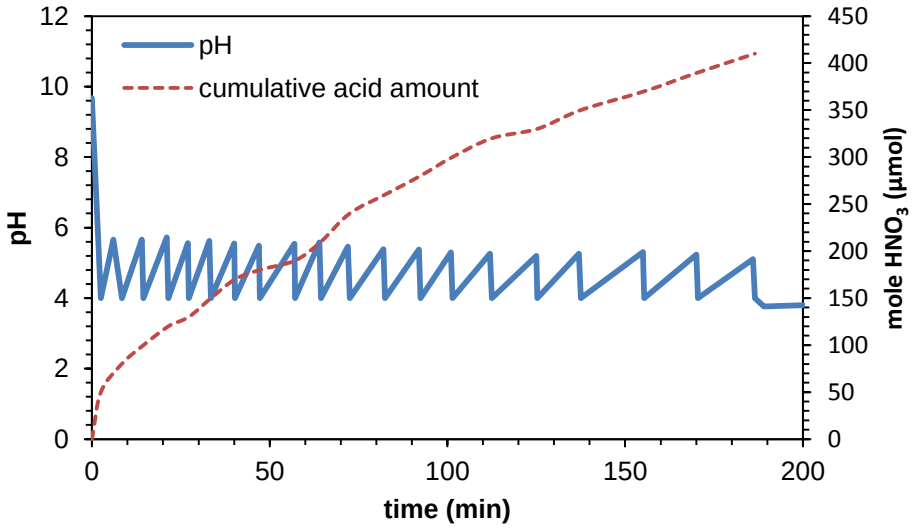

Figure S3.7 Titration of 50 mL of 1 g/L sample suspension (from Core 1) using 1M HNO_3. Ultimately, the solid consumed 8.2 mmol HNO_3 per gram of solid.

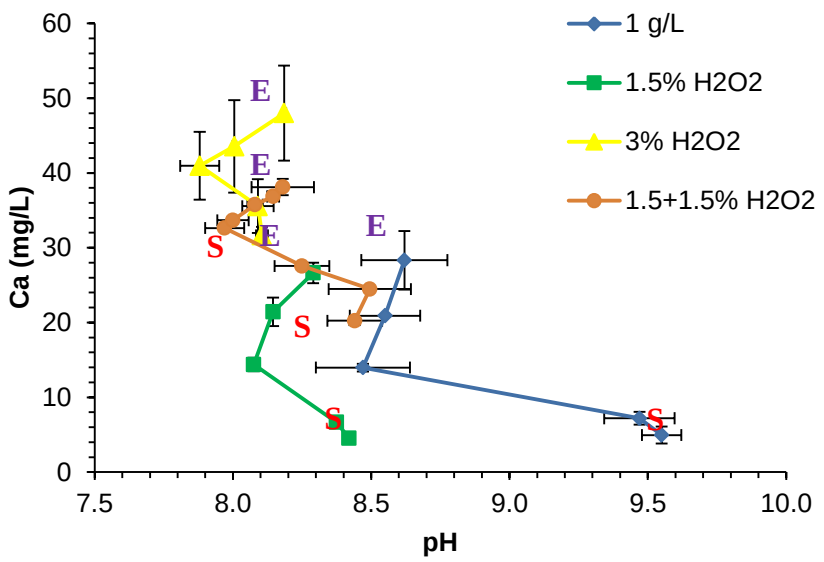

Figure S3.8 Ca dissolution trajectory with pH evolution. "S" indicates the starting point and "E" indicates the end point of reaction.

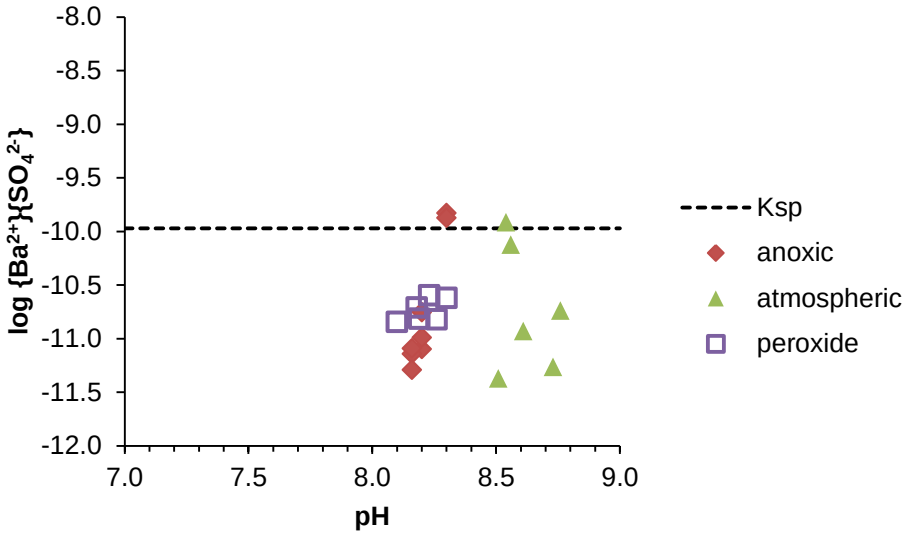

Figure S3.9 $BaSO_4$ ion activity products (IAP) in experiments compared with the solubility product. Markers are IAP in different experiments, calculated as the product of Ba^{2+} activity and SO_4^{2-} activity. The ionic strengths of the aqueous phase were low enough that the activities could be approximated by concentrations. The dashed line is the logarithm of solubility product of $BaSO_4$ (from Table S3.2). Considering the uncertainty of the reported $K_{sp,BaSO4}$ value, the proximity between the data points and the predicted $BaSO_4$ solubility equilibrium (within one order of magnitude) indicate that $BaSO_4$ solubility could control the Ba mobilization.

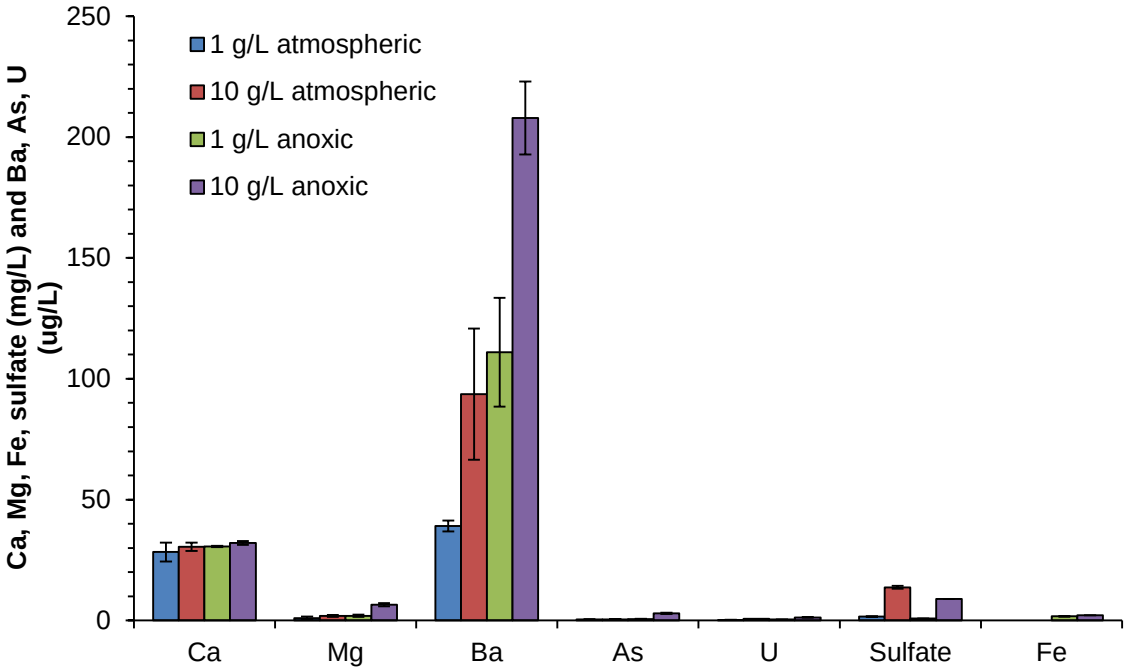

Figure S3.10 Element (sulfate) mobilization at 1 and 10 g/L solid:water ratio in atmospheric and anoxic conditions. Samples taken after 120 hours of reaction.

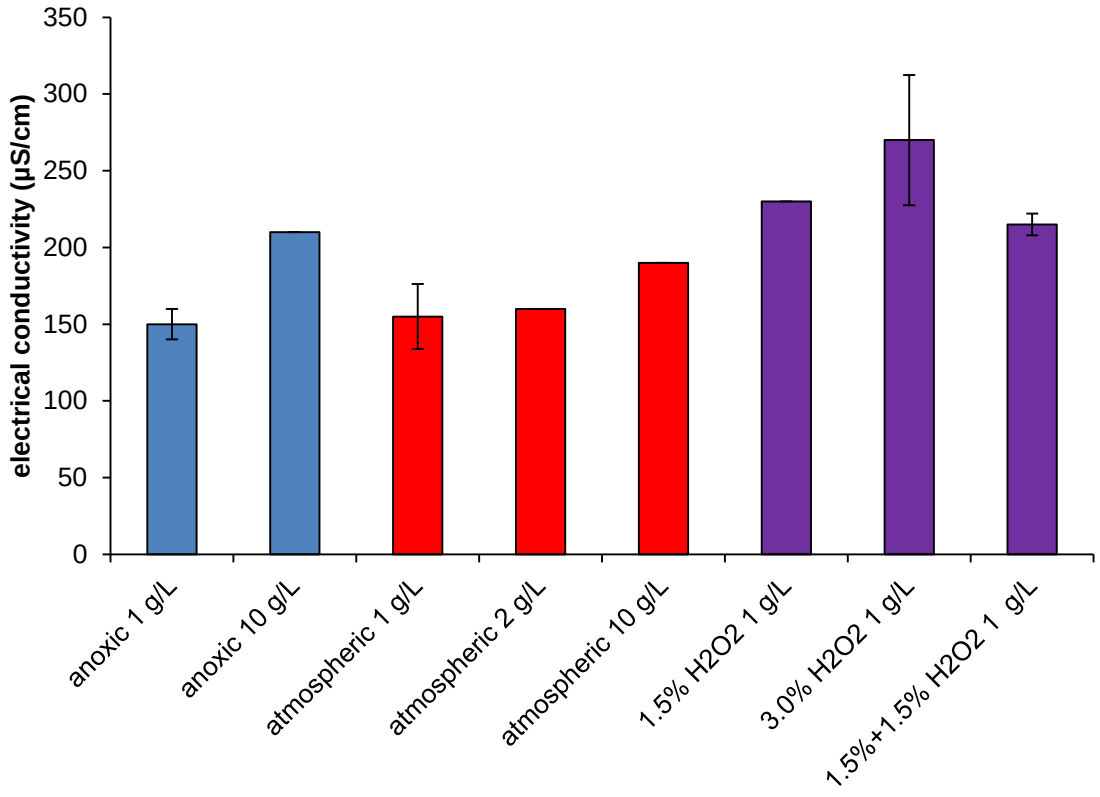

Figure S3.11 Electrical conductivity of suspensions at 120 hours in Experiments 8-15. Data are shown as the averages between the duplicates with error bars being the standard deviations. Some duplicates had the same measurements that resulted in zero standard deviations.

Table S3.3 Measured electrical conductivity compared with calculated conductivity based on aqueous phase composition

solid:water ratio (g/L)	$[Ca^{2+}]$	$[Mg^{2+}]$	$[SO_4^{2-}]$	$[Cl^-]$	$[HCO_3^-]$	TDS[a]	IS[b]	calculated EC[c]	measured EC
	(mg/L)						(mM)	(µS/cm)	
1	28.34	0.90	3.35	7.49	73.88	114.0	2.27	151	155
2	26.64	0.97	4.50	6.17	69.86	108.1	2.17	143	160
10	30.47	1.84	12.94	6.68	74.36	126.3	2.65	174	190

[a] TDS was calculated assuming the cations and anions listed were the only species. $[HCO_3^-]$ was the dominant carbonate species in the relevant pH range and was calculated by charge balance; concentrations of all the other ions were known from analyses.

[b] IS (ionic strength) = $0.5\Sigma c_i z_i^2$ where c_i is the concentration of species i in mole per liter, and z_i is the charge on species i.

[c] Conductivity factors for ions(Tchobanoglous and Schroeder, 1985) were implemented in the calculation.

Chapter 4: Element Mobilization from Bakken Shales as a Function of Water Chemistry

Results of this chapter have been submitted to *Environmental Science and Technology* for review.

Graphic Abstract

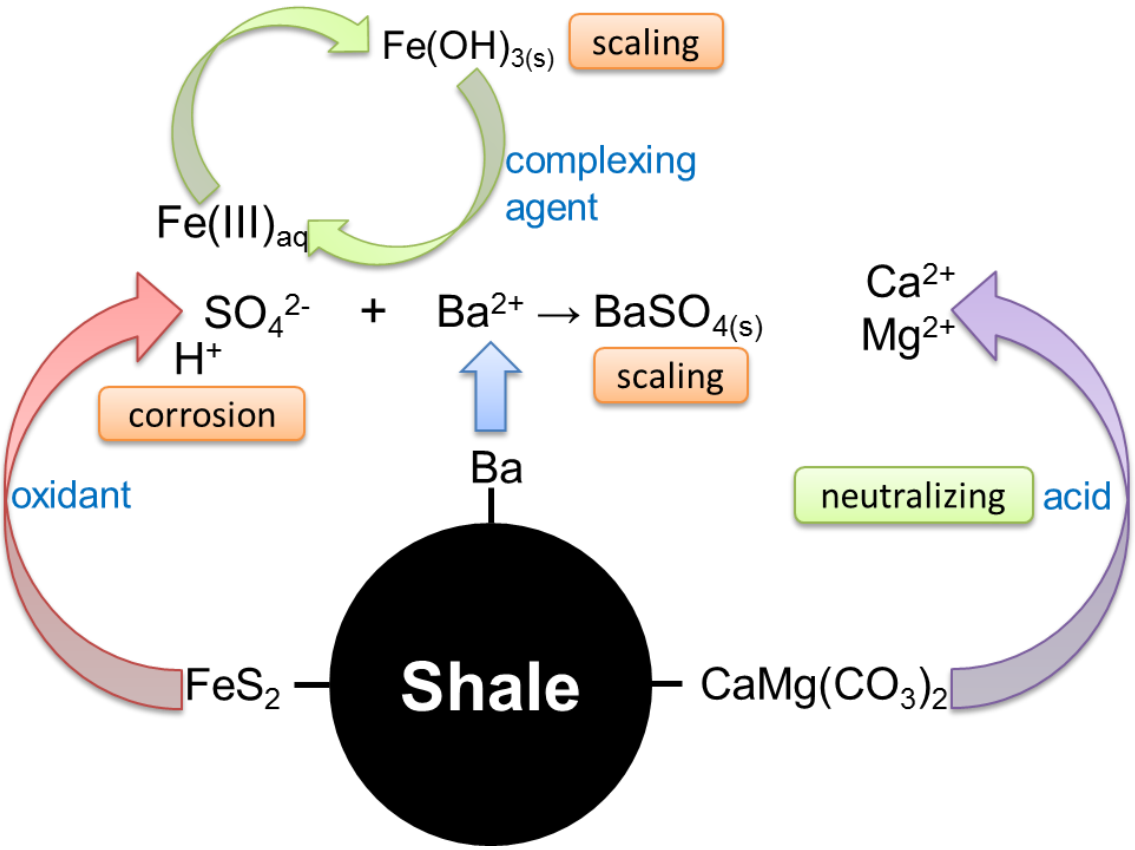

Abstract

The use of hydraulic fracturing for shale gas and oil extraction may significantly impact water quality. The wastewater that returns to the surface after injection of a hydraulic fracturing fluid contains elements, including regulated metals and metalloids, mobilized by interactions between the fracturing fluid and the formation. The rate and extent of mobilization depends on the geochemistry of the formation and the chemical characteristics of the fracturing fluid. Laboratory experiments investigated the influence of water chemistry on element mobilization from core samples taken from the Bakken Formation, one of the most productive shale oil plays in the US. Fluid properties were varied with regard to pH, oxidant level, solid:water ratio, temperature, and chemical additives. The release of elements from the Bakken samples strongly depended on solution pH and redox condition and to a lesser extent on the temperature and solid:water ratio. The presence of oxygen and addition of H_2O_2 or $(NH_4)_2S_2O_8$ led to pyrite oxidation and resulted in an elevated amount of sulfate. The low abundance of carbonate minerals relative to pyrite would lead to lowering of the system pH in the presence of oxidants and to enhanced mobility of many elements.

4.1 Introduction

The use of horizontal drilling in conjunction with the development and expansion of hydraulic fracturing technologies has significantly increased the extraction of natural gas and oil from low-permeability geological formations, and in particular, shale formations (Kuuskraa et al., 2011). Based on these advances, the US Enegry Information Administration (EIA) estimates for total technically recoverable wet natural gas and crude oil resources in the US were increased by 38% and 35% respectively in 2013 (U.S. EIA, 2013). As one of the most productive play in the US, the Bakken formation and Three Forks formation, which underlies the Bakken formation, in the Williston Basin of Montana, North Dakota and South Dakota are estimated to have mean undiscovered volumes of 7.4 billion barrels of oil, 6.7 trillion cubic feet of associated/dissolved natural gas, and 0.53 billion barrels of natural gas (USGS, 2013). The depth of the Bakken formation ranges from 4500-12000 ft (1.4-3.6 km) (Tverberg, 2008; U.S. EIA, 2011), consisting of organic-rich upper and lower shale layers (maximum thicknesses of 56 and 58 ft respectively) as the hydrocarbon source rock with a middle layer (maximum thickness of 90 ft) as a hydrocarbon reservoir (Kuhn et al., 2010; USGS, 2013). The Bakken formation is characterized by high heat flow with a thermal gradient of 1.8-2.0 ℉/100 ft (31.5-35.0 ℃/km) (Olesen, 2010), leading to a temperature between 90 and 100 ℃ at the depth of samples used in this study.

Hydraulic fracturing is a subsurface hydrocarbon recovery technology whereby a mixture of water, proppant, and chemical additives is pumped into the well bore under pressure to create and propagate fractures in the surrounding formation (Ely, 1985). The proppant (for example, fine sand) is added to hold resulting pores and channels effectively open in the formation thus allowing for subsequent gas extraction. A fracturing job can require 0.5-5 million gallons (7570-

18930 m^3) of water and for the Bakken formation, 0.5 to 3 million gallons (1890-11360 m^3) are typically used per well (Hagemeier and Hutt, 2009; Stephen et al., 2010; Gregory et al., 2011; Scanlon et al., 2014). After the fracturing process, some of the injected fracturing fluid returns to the surface (referred to as flowback) in addition to formation waters (referred to as produced water). For wells in the Bakken Formation, 17-47% of the water used in hydraulic fracturing is typically recovered as flowback (Stephen et al., 2010). Flowback contains not only the original additives and natural fluids within the formation (Vengosh et al., 2014) but also elements mobilized from the formation. These can include a number of heavy metals, metalloids, organic matter and hydrocarbons (Gregory et al., 2011). While approximately 750 chemicals are listed as additives for hydraulic fracturing in a reported submitted to the congress (Waxman et al., 2011), most fluids contain less than 20 total additives (U.S. EPA, 2004). Additives usually comprise 0.5-3 wt % of the fluid and include surfactants, scale inhibitors, co-solvents and acids (King, 2012), with each additive serving an engineering purpose. The composition of hydraulic fracturing fluids is typically designed for specific formations and is often varied depending on the stage of well development.

Flowback and produced waters can contain total dissolved solids (TDS) several times higher than those of seawater (Haluszczak et al., 2013). For example, produced waters from the Bakken Formation, the subject of this study, have been reported with TDS ranging from 72,999 to 377,261 mg/L (Blondes et al., 2014). The most common management options for flowback and produced waters are reuse (requiring little treatment), recycle (with more involved treatment) and disposal via deep well injection (Nicot et al., 2014). Disposal approaches vary by play, depending on the quantity and quality of the wastewater, as well as the availability of treatment and disposal facilities (Benko and Drewes, 2008). The Bakken formation waste streams are

typically managed via deep-well injection (Stephen et al., 2010; Nicot et al., 2014). Despite some recent report of regulated trace elements detected in flowback and produced waters (Hayes, 2009; Chapman et al., 2012; Haluszczak et al., 2013; Kondash et al., 2013), information quantifying elements mobilized from shale formations during hydraulic fracturing and the specific factors controlling such mobilization is limited.

Mobilization of elements, via fluid interaction(s), can occur through a variety of pathways that depend on the formation composition and (fracturing) fluid chemistry. Strong acids (e.g., HCl) are usually the single largest liquid additive in a typical fracturing fluid, and are used to dissolve acid-soluble minerals (e.g., carbonates) thus helping to initiate fractures (Gregory et al., 2011). Metals originally attached to host minerals can desorb due to changes in pH and through the introduction of complexing agents. For example, citric acid, which is used to prevent precipitation of metal oxides (Arthur et al., 2008; Gregory et al., 2011), can form strong complexes with several regulated metals (e.g. Cr, Pb, U, Cu) (Hamm et al., 1958; Field et al., 1974; Kourgiantakis et al., 2000; Pasilis and Pemberton, 2003) thus increasing their effective mobility. In addition, oxygen and other oxidative additives (e.g. ammonium persulfate which is used as a gel breaker (Montgomery, 2013)) in fracturing fluids may drive significant redox sensitive geochemical reactions resulting in mobilization of trace elements such as U and Cr that are more soluble in their oxidized forms (Rai et al., 1989; Wu et al., 2007).

The objective of this study was to examine element mobilization during rock-water interactions as a function of aqueous chemistry with core samples from a productive formation that is currently being (primarily) hydraulically fractured. This study used samples from the Bakken formation, a productive natural shale oil play, and investigated the effect of solution pH, oxidant level, solid:water ratio, temperature and selected chemical additives as water chemistry

variables. Experiments sought to advance the understanding of key factors controlling the release of elements from organic-rich shales. Such information is critical for understanding and even controlling flowback and produced water composition(s) for Bakken and similar formations, and for effectively managing resulting wastewater streams.

4.2 Materials and Methods

4.2.1 Materials

All chemicals were used as received without further treatment. Solutions were prepared with ultrapure water (resistivity > 18.2 MΩ•cm). Glass volumetric flasks, beakers and bottles were acid-cleaned and rinsed several times with deionized water and ultrapure water prior to use. For pH adjustments, 0.1 M nitric acid (HNO_3) and 0.1 M sodium hydroxide (NaOH) were prepared from trace-metal grade concentrated HNO_3 and ACS-grade NaOH from Fisher Scientific. For experiments at high oxidant loadings, hydrogen peroxide (H_2O_2, 30 wt % solution, Sigma Aldrich) was used. For experiments with chemical additives, hydrochloric acid (HCl, trace-metal grade), citric acid monohydrate (ACS grade) and ammonium persulfate [$(NH_4)_2S_2O_8$, ACS grade] were from Fisher Scientific.

Bakken shale samples were taken from a rock core that was from a well in Burke County, ND and is preserved in the USGS Core Research Center (Denver, CO). Two samples (Figure S4.1) from the same rock core but different depths [Sample 1 from 7454 ft (2272 m) and Sample 2 from 7407 ft (2258 m)] were used in the experiments. Upon arrival in the laboratory, samples were ground to powders with an agate mortar and pestle, sieved to a size fraction of 53 – 106 μm and stored in a vacuum desiccator.

4.2.2 Solid Characterization

X-ray diffraction (XRD) with Cu Kα radiation (Bruker d8 Advance X-ray diffractometer) provided information on the mineralogy of the samples. Approximately 250 mg of sample were placed in an aluminum sample holder, with preferred orientation minimized by excessive sample agitation. The quantitative analysis of multiphase mixtures was conducted using the Bruker Topas program by means of Rietveld analysis of the entire diffraction pattern (2θ ranged from 5 ° to 70 °). The lower detection limit of the Rietveld analysis is approximately 1 wt% (Madsen et al., 2001), which was sufficient to capture the pyrite phase in the samples. Strong acid digestion (procedure in Supporting Information) followed by inductively coupled plasma mass spectrometry (ICP-MS, Agilent 7500ce) was performed for elemental composition analysis. Extraction results of two USGS reference shale materials, by the same procedure, are listed in Table S4.1. For most elements discussed in this work (Ca, Mg, Fe, As), the extractable portions were above 80%. The specific surface area of the powdered samples was measured by BET-N_2 adsorption (Brunauer et al., 1938) (NOVA 2000e, Quantachrome Instruments). Total carbon (TC) and total inorganic carbon (TIC) of the solids were measured with a total organic carbon analyzer (TOC-LCPH with SSM-5000A, Shimadzu Corp.).

4.2.3 Batch Experiments

The mobilization of metals from both samples was studied in a series of batch experiments that explored the effect of pH, redox condition, solid:water ratio, temperature and chemical additives (Table 4.1). All experiments were performed in duplicate. Reactions were initiated by the addition of sample into 150 mL ultrapure water to achieve a target solid:water ratio, which was 1 g/L in all experiments except for Experiment 8 with an elevated solid:water ratio. Suspensions were continuously mixed by magnetically stirring at 600 rpm. All batch

reactors except for those probing anoxic conditions and at elevated temperatures were open to the atmosphere. A reaction time of 120 hours was used, which was found sufficient for most elements to reach stable concentrations in preliminary experiments. Aliquots (15 mL) of suspension were sampled at 1, 4, 24, 48 and 120 hours and filtered through 0.22 μm polyethersulfone (PES) membranes for aqueous phase analyses. The suspension pH was monitored throughout the course of experiments using a benchtop pH meter (Fisher Scientific Accumet XL15).

For investigation of pH, oxidants [H_2O_2 and $(NH_4)_2S_2O_8$], and chelating agent (citrate) (Experiments 1, 2, 4, 11, 12), the pH was controlled by an autotitrator (902 Titrando, Metrohm USA Inc.). Either 0.1 M HNO_3 or 0.1 M NaOH was intermittently added to the suspensions to control the pH at target values of 4 (±0.02) or 8 (±0.05). In investigating the effect of oxidizing conditions (Experiment 4), H_2O_2 was selected as a model oxidant. The concentration of H_2O_2 (3 wt %) was selected to be in great excess of the oxidant demand exerted by organic carbon and pyrite in the samples, thus driving the maximum extent of oxidation for those species that can be oxidized by H_2O_2. A portion of 15 mL 30% H_2O_2 solution was diluted to a total volume of 150 mL with ultrapure water to obtain 3% H_2O_2 concentration prior to the addition of sample powders. In Experiment 8, an elevated solid loading of 10 g/L was used to investigate the effect of solid:water ratio on element release to solution. For experiments that examined chemical additives (Experiments 10-12), the concentrations of HCl, citrate, and $(NH_4)_2S_2O_8$ were selected based on the actual concentrations of these chemicals used in wells that are hydraulically fractured in Burke County, ND. The chemical usage information, declared voluntarily be well operators, was accessed from the FracFocus website. These three additives were selected

because their presence would alter the solution properties (e.g. pH and redox condition) and possibly drive chemical changes.

Experiment 3 at anoxic conditions followed the procedure outlined in the authors' previous work with Eagle Ford formation samples (Wang et al., 2014), and the illustration for the experimental setup is in Figure S4.2. Experiments 6 and 7 at elevated temperatures were performed with a circulating heated bath (Isotemp 3016H, Fisher Scientific). The circulating fluid was either water for temperature control at 50 ℃ (Experiment 6) or antifreeze for temperature control at 80 ℃ (Experiment 7). Pyrex bottles with Teflon tape and autoclavable polypropylene seal caps had a headspace of about 150 mL.

4.2.4 Analytical Methods

A portion of the filtrate was acidified to contain 2% HNO_3 and analyzed for concentrations of dissolved metals (Ca, Mg, Fe, Ba, U, Pb, Cr, etc.) and metalloids (As) by ICP-MS. Another portion of the filtrate was refrigerated at 4 ℃ for sulfate analysis by ion chromatography (Dionex ICS-1600, Thermo Scientific) and non-purgeable organic carbon (NPOC) measurements (TOC-LCPH, Shimadzu Corp.). Inductively couple plasma optical emission spectrometry (ICP-OES, PerkinElmer Optima 7300DV) was used for As and Cr analysis in Experiment 13 to eliminate polyatomic interferences observed on ICP-MS. Detection limits for these analytical methods are compiled in Table S4.2.

Table 4.1 Conditions and variables explored in the experiments performed

Exp. No.	Target pH	Final pH [a] Sample 1	Final pH [a] Sample 2	Redox condition [b]	Solid:water ratio (g/L)	Temperature (℃)	Salt (g/L)	Chemical additives
1	4	4.0	4.0	Atmospheric	1	22	-	-
2	8	8.0	8.0		1		-	-
3	Unadjusted	7.8	7.9	Anoxic	1		-	-
4	8	8.0	8.0	Oxidative	1	22	-	3% H_2O_2
5	Unadjusted	7.8	8.2	Atmospheric	1		-	-
6	Unadjusted	7.7	8.9	Atmospheric	1	50	-	-
7		5.8	8.4		1	80	-	-
8	Unadjusted	7.7	8.4	Atmospheric	10	22	-	-
9	Unadjusted	7.9	8.1	Atmospheric	1	22	10	-
10	Unadjusted	1.5	1.5	Atmospheric	1	22	-	66 mM HCl
11	4	4.0	4.0	Atmospheric	1		-	1.0 mM citrate
12	8	8.0	8.0	Oxidizing	1		-	2.9 mM $(NH_4)_2S_2O_8$
13	Unadjusted	1.5	1.5	Oxidative	1	80	-	66 mM HCl, 1.0 mM citrate and 2.9 mM $(NH_4)_2S_2O_8$

[a] Expressed as the average between the duplicates; the differences between the duplicates for all experiments were below 0.2 pH unit. In Experiments 1, 2, 4, 11, 12, pH was controlled by an autotitrator.

[b] "Atmospheric" means that the solutions were exposed to the reactor headspace in Experiments 6,7 and 11 or the reactor was open to the atmosphere in the other experiments. Oxygen was the primary oxidant in this condition. "Oxidative" indicates the addition of an oxidant (3% H_2O_2 in Experiment 4 and 2.9 mM $(NH_4)_2S_2O_8$ in Experiments 12 and 13)

Table 4.2 Physical and chemical properties of core samples compared with reported values of Bakken sample properties

	Sample 1	Sample 2	Lower Bakken [d]	Middle Bakken [d]	Upper Bakken [d]
Major Element [a] (in percentage)					
Calcium	1.70 ±0.03	4.01 ±0.12	2.21 ±3.79	8.39 ±4.45	3.94 ±4.49
Magnesium	1.00 ±0.01	2.34 ±0.04	1.25 ±0.52	2.92 ±1.46	1.62 ±1.03
Iron	3.40 ±0.04	0.91 ±0.02	2.22 ±1.33	1.19 ±0.65	2.08 ±0.81
Silicon	NA	NA	25.12 ±4.78	26.24 ±6.28	21.68 ±4.93
Aluminum	0.01 ±0.00	0.01 ±0.00	6.87 ±1.96	3.34 ±1.43	5.79 ±1.68
Potassium	0.46 ±0.00	0.47 ±0.02	4.17 ±1.19	2.37 ±1.00	3.94 ±1.11
Sodium	0.09 ±0.00	0.20 ±0.00	0.44 ±0.22	0.39 ±0.26	0.36 ±0.16
Manganese	0.01 ±0.00	0.02 ±0.00	0.03 ±0.09	0.05 ±0.02	0.02 ±0.02
Trace element [a] (in mg/kg)					
Vanadium	334.1 ±4.4	19.7 ±0.7	5299.91 ±7619.12	433.47 ±1629.01	4402.41 ±7286.56
Zinc	90.6 ±2.2	93.0 ±1.3	859.54 ±3735.05	59.04 ±154.58	1223.29 ±3143.97
Nickel	781.0 ±5.4	35.0 ±0.4	286.57 ±216.50	33.04 ±28.23	343.53 ±209.56
Barium [b]	16.3 ±0.0	14.1 ±0.4	308.37 ±529.77	252.72 ±519.39	495.65 ±1431.62
Molybdenum	528.0 ±10.6	6.2 ±5.5	NA	NA	NA
Copper	113.0 ±1.0	43.2 ±0.9	71.71 ±93.00	11.39 ±8.49	98.69 ±125.74
Arsenic	109.4 ±1.0	11.5 ±0.2	NA	NA	NA
Chromium	25.5 ±0.8	16.9 ±0.6	460.02 ±477.94	206.10 ±277.02	355.31 ±448.77
Lead	66.7 ±1.2	13.1 ±0.7	29.15 ±25.25	14.29 ±17.17	42.53 ±46.41
Uranium	67.8 ±1.1	0.3 ±0.0	62.91 ±117.69	5.20 ±5.28	42.71 ±41.19
Physichemical properties					
Specific surface area (m^2/g)	2.17	11.55			
Total carbon [a] (mg/g)	195.9 ±2.1	27.9 ±0.5			
Inorganic carbon [a] (mg/g)	8.2 ±0.2	20.9 ±0.6			
Total organic carbon [c] (mg/g)	187.7 ±2.1	7.0 ±0.8			

[a] Expressed as average ± standard deviation of triplicate analyses

[b] Barium recovery from the solid during solid digestion was incomplete, so these values do not represent the total Ba content of the samples.

[c] Determined as the difference between the total carbon and inorganic carbon.

[d] Data from Karma and Parslow, 1989 and expressed as average ± standard deviation of hundreds of samples for geochemical analysis.

4.3 Results and Discussion

4.3.1 Sample Composition

Based on XRD measurements (Figure 4.1 and Table S4.3), both samples were rich in quartz, dolomite, clay minerals (illite) and K-feldspar (microcline) with a minor amount of pyrite, which is consistent with the reported mineralogy of the Bakken Formation (Mba and Prasad, 2010; Sarg, 2012). The ratio of dolomite to pyrite is much higher in Sample 2 (25.2) than Sample 1 (1.5) resulting in the significantly different acid neutralizing capacities of the two samples (for the case of pyrite oxidation). Solid digestion results (Table 4.2) are consistent with XRD observations. The Mg/Ca mass ratio is 0.588 in Sample 1 and 0.584 in Sample 2, which are very close to the theoretical value of 0.606 in dolomite. For these samples, the amount of Fe corresponds to the presence of pyrite. The organic-rich Sample 1 contains higher amounts of regulated trace elements (As, Cu, Cr, Pb, U) than organic-poor Sample 2.

Sample 1 and Sample 2 had distinct physical and chemical properties (Table 4.2). Although ground and sieved to the same particle size fraction (53 – 106 μm), the specific surface areas of the two samples differed (2.17 m^2/g for Sample 1 and 11.55 m^2/g for Sample 2). TIC (8.2 mg/g for Sample 1 and 20.9 mg/g for Sample 2) as carbonate was correlated with the amount of dolomite. The total organic carbon (TOC), determined as the difference between TC and TIC, was 187.7 mg/g (18.77%) for Sample 1 and 7.0 mg/g (0.70%) for Sample 2. Overall, the abundance of some redox-sensitive trace elements (Cu, Mo, Ni, U, V) and TOC in Sample 1 is consistent with the enrichment of these elements in the organic-rich lower Bakken shales, whereas lower contents of these in Sample 2 corresponds to the composition of the middle Bakken layer (Nandy et al., 2014).

The following discussion on mobilization results focuses on the aqueous concentrations of selected metals and metalloids either because they are major elements (Ca, Mg, Fe, Mn) that affect the fate of other elements and influence the total dissolved solids of the water or because they are regulated trace elements (Ba, As, Cr, U) (U.S. HHS, 2003; U.S. EPA, 2010). The mobilization results for all analyzed elements (concentrations and percentages) that were above detection limits are compiled in Tables S4.4 and S4.5.

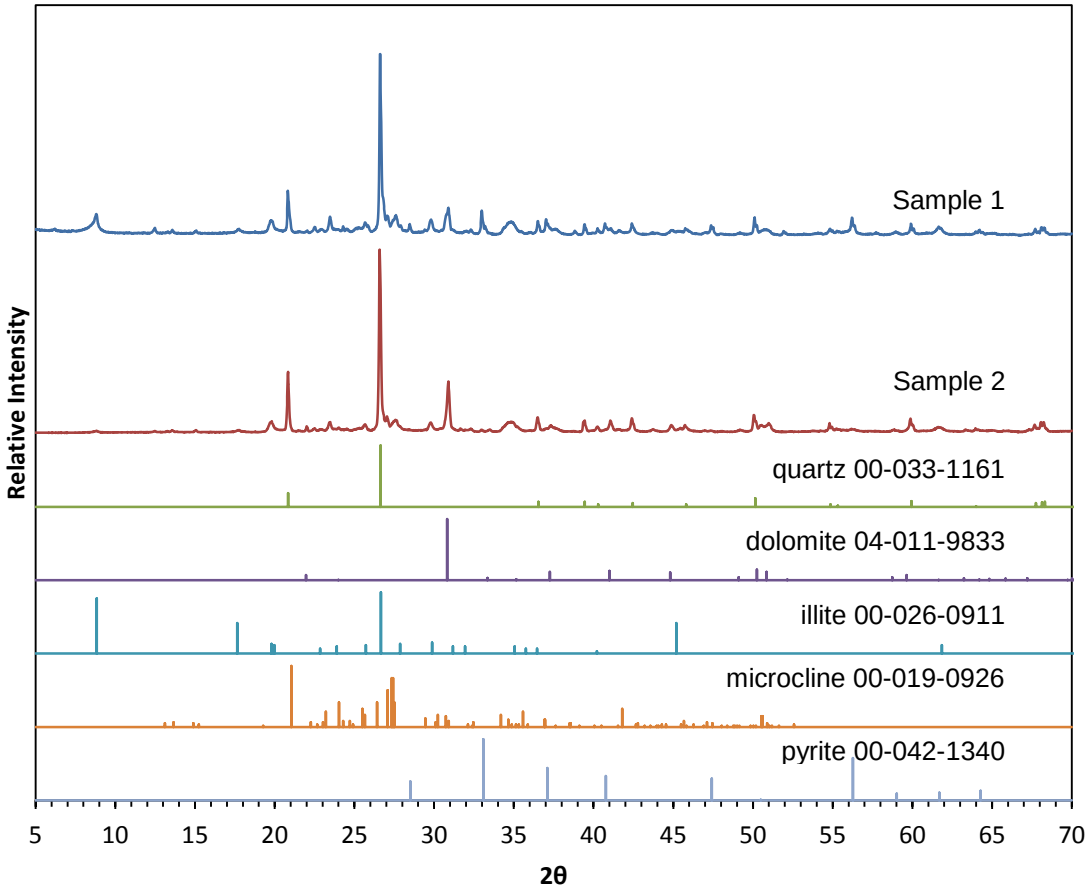

Figure 4.1 Powder X-ray diffraction (XRD) patterns of samples. The reference patterns of five minerals from the International Centre for Diffraction Data database are shown for comparison.

4.3.2 Effects of Solution pH and Citrate

The pH of the sample suspension significantly affected the mobilization of many metals. In general, higher concentrations of elements (Ca, Mg, Fe, Mn, As) were observed at lower pH (Figure 4.2). In Experiment 10, which investigated the effect of acid (HCl) as a chemical additive, pH was decreased to 1.5 and all Ca and most Mg (84.2% in Sample 1 and 91.3% in Sample 2) were observed to dissolve. At pH 4, while all Ca and Mg available in Sample 2 was dissolved, only 82.1% Ca and 73.5% Mg from Sample 1 were mobilized. Mg and Ca concentrations were strongly correlated due to their common dolomite source, and in general, their mobilization agreed with previous observations of dolomite dissolution increasing with decreased pH (Pokrovsky et al., 1999). The Mg/Ca ratio in the aqueous phase were almost always below that of stoichiometric dolomite dissolution (Figure S4.3) which is likely due to the preferential release of Ca from dolomite due to the lower hydration energy of Ca relative to Mg as observed in other studies (Busenberg and Plummer, 1982; Pokrovsky and Schott, 2001). For both samples, Fe and Mn concentrations were much higher at lower pH values, consistent with the solubility of iron oxides and manganese oxides in atmospheric conditions. Arsenic (As) concentrations tracked Fe concentrations for Sample 1, reaching 44 μg/L at pH 1.5. The concentrations of both Cr and U remained below 10 μg/L throughout these experiments.

The addition of 1 mM citrate increased the extent of Fe and As mobilization from Sample 1 (Figure 4.2a). According to solubility calculations, citrate is expected to significantly increase total dissolved Fe if Fe(III) is the primary oxidation state (Figure S4.4). While Fe concentrations with citrate were twice as much as those without, the degree of this increase was well below the equilibrium solubility prediction (Figure S4.4), which is likely due to the kinetic limitations of oxidative pyrite dissolution, as indicated by the similar sulfate concentrations (Table S4.4) at pH

4 with and without citrate. Consistent with Fe mobilization, As release from Sample 1 was also higher in the presence of citrate. Throughout all the experiments, As concentrations were observed to correlate with Fe concentrations (Figure S4.5), most likely due to their common source being sulfide minerals. Citrate also promoted dolomite dissolution, which could be explained by dolomite surface coordination theory (Pokrovsky and Schott, 2001). The adsorption of citrate results in a net negative charge to the surface coordination sphere, polarizing the Ca-O and Mg-O bonds and facilitating the detachment of Ca and Mg from the mineral surface (Pokrovsky and Schott, 2001).

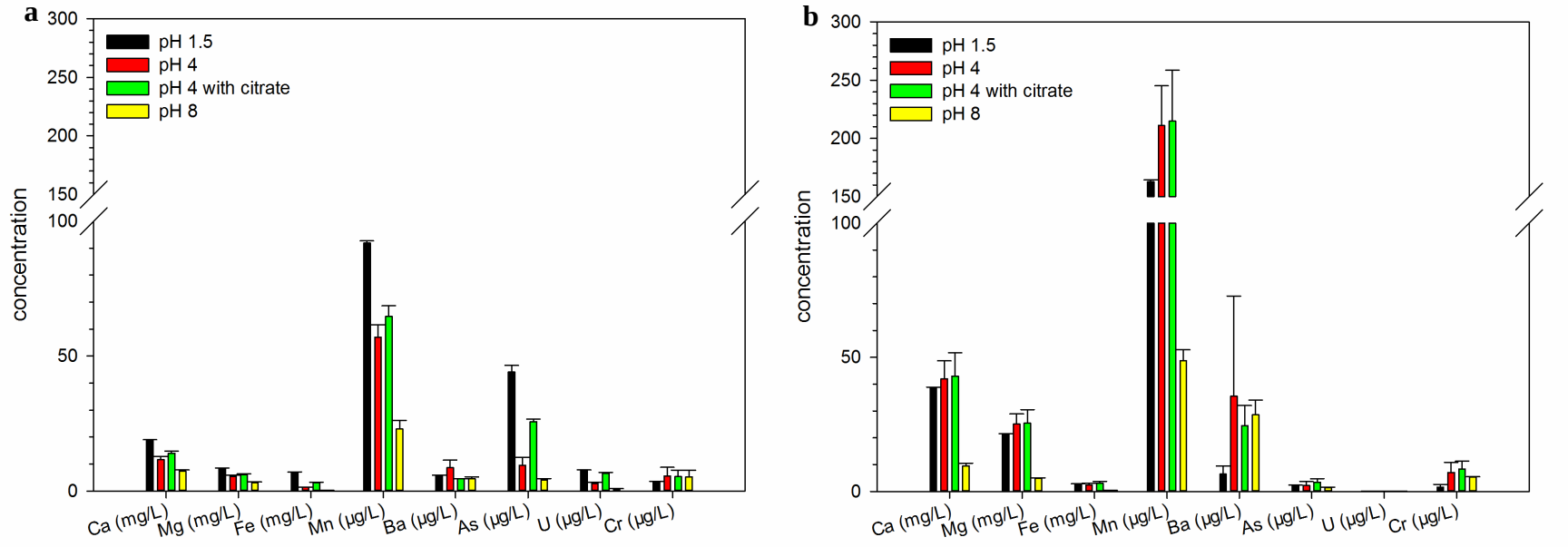

Figure 4.2 Final metal concentrations after 120 hours of reaction with (a) Sample 1 and (b) Sample 2 at pH 1.5 (Experiment 10), pH 4 and 8 (Experiments 1 and 2) and pH 4 with citrate (Experiment 11). Experiments were performed at room temperature (22℃) with 1 g/L shale loading. Data are shown as the average of the duplicates with the error bars being the standard deviations. In Experiment 10, pH stabilized at 1.5 upon HCl addition at the beginning of the reaction to achieve a total HCl concentration of 66 mM. In the other experiments, an autotitrator was used to control the suspension pH at 4.00 ±0.02 or 8.00 ±0.05.

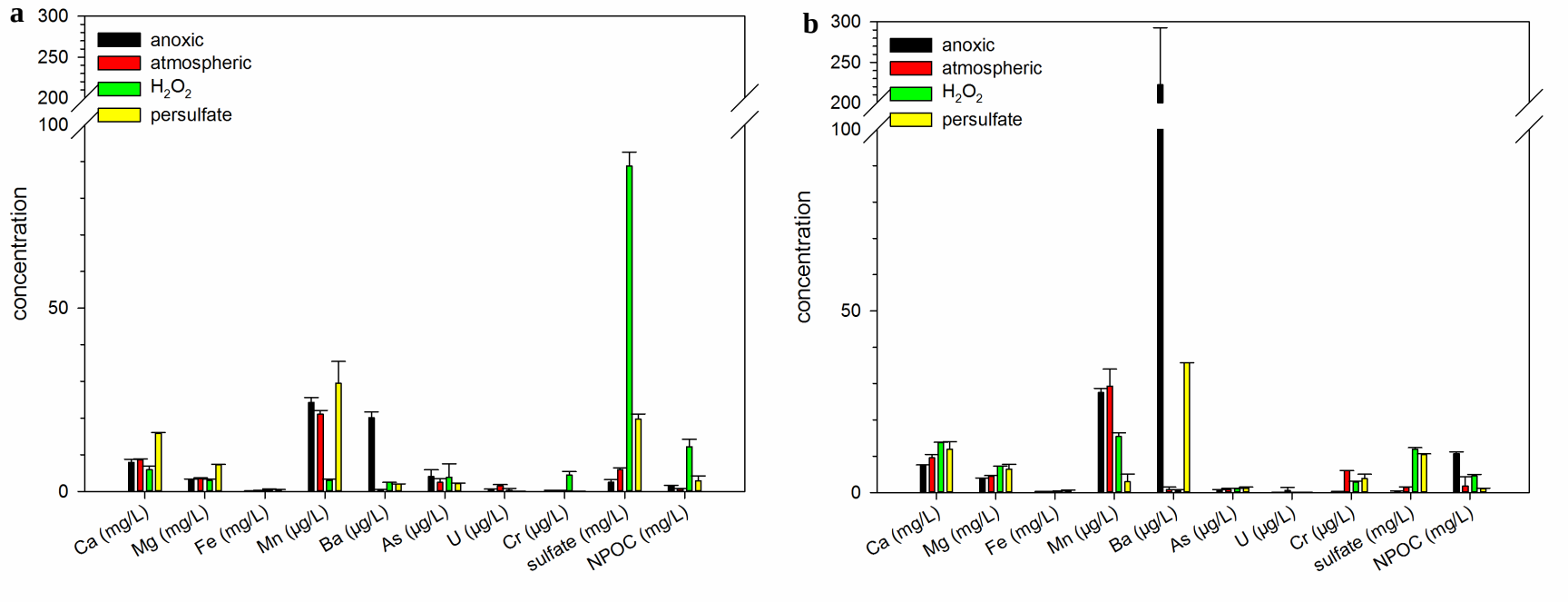

Figure 4.3 Metal, sulfate and NPOC mobilization after 120 hours of reaction with (a) Sample 1 and (b) Sample 2 under anoxic (Experiment 3), atmospheric (Experiment 5) and oxidative conditions (Experiments 4 and 12). Experiments were performed at room temperature (22°C) with 1 g/L shale loadings. Data are shown as the average of the duplicates with error bars being the standard deviations. The atmospheric and oxidative condition experiments were open to the laboratory atmosphere, and the anoxic experiments had headspaces with 400 ppm CO_2. For anoxic and atmospheric conditions, pH stabilized at 8.0 ±0.2 without adjustment. For oxidative conditions (with H_2O_2 or persulfate), an autotitrator was used to control the suspension pH at 8.00 ±0.05.

4.3.3 Oxidant Level Effect

For anoxic experiments, thorough pH monitoring indicated that the use of N_2/CO_2 gas sparging through the headspace (Figure S4.2) allowed for TIC and pH levels comparable to those under atmospheric conditions. With a stable pH (8.0 ± 0.2) for all redox conditions evaluated, Ca and Mg concentrations were similar with or without oxygen/H_2O_2 as dolomite dissolution is relatively independent of redox conditions (Figure 4.3). Fe concentrations remained low (below 0.5 mg/L) in these experiments either because of slow pyrite dissolution in anoxic conditions or because of rapid Fe(II) oxidation by oxygen, H_2O_2, or $(NH_4)_2S_2O_8$ followed by $Fe(OH)_3$ precipitation at pH 8 (Crittenden et al., 2012).

Compared with anoxic experiments, the elevated sulfate concentrations for open systems (atmospheric) and with H_2O_2 or $(NH_4)_2S_2O_8$ suggest that pyrite was oxidized when there were strong oxidants present (Figure 4.3). Anoxic conditions strongly inhibited sulfate release with 2.5 mg/L sulfate released from Sample 1 and 0.5 mg/L from Sample 2. Under atmospheric conditions (open), sulfate mobilization increased to 6.0 mg/L (Sample 1) and 1.4 mg/L (Sample 2). With the addition of 3% H_2O_2, sulfate generation further increased to 88.8 mg/L (Sample 1) and 11.9 mg/L (Sample 2). As the H_2O_2 concentration was in significant excess of the calculated theoretical oxidant demand from the observed TOC and pyrite concentrations, these sulfate concentrations represent a maximum that could be produced for these conditions at pH 8 within 120 hours.

The acidity generated from complete pyrite oxidation by oxygen and H_2O_2 as shown in Reactions (4.1) and (4.2) would be significant if there were no other minerals (e.g., carbonates) providing buffering capacity (Chermak and Schreiber, 2013). The mole ratio of dolomite to pyrite that represents complete neutralization is 2:1 according to Reactions (4.3) and (4.4). The

Bakken samples used in this study had dolomite to pyrite mole ratios of 0.7 (Sample 1) and 6.2 (Sample 2). Consequently, while Sample 2 suspension(s) could effectively stabilize pH of the system, Sample 1 could not upon pyrite oxidation by abundant (strong) oxidants. A control experiment with 3% H_2O_2 and no pH adjustment confirmed the above predictions: for Sample 2 the system pH stayed steadily around 7.9 whereas for Sample 1 suspension it rapidly dropped below 4 within the first few hours of reaction and stabilized at 3.3. The mobilization results for Sample 1 with and without the autotitrator were consistent with pH effect observations. Ca and Mg completely dissolved at pH 3.3 without (auto)titration, with Fe and Mn concentrations observed to be significantly higher at pH 3.3 than at pH 8.0 (Figure S4.6).

$$FeS_2 + 15/4\ O_2 + 7/2\ H_2O \rightarrow Fe(OH)_{3(s)} + 2SO_4^{2-} + 4\ H^+ \quad (4.1)$$

$$FeS_2 + 15/2\ H_2O_2 \rightarrow Fe(OH)_{3(s)} + 2SO_4^{2-} + 4\ H^+ + 4\ H_2O \quad (4.2)$$

$$FeS_2 + 2\ CaMg(CO_3)_2 + 15/4\ O_2 + 7/2\ H_2O \rightarrow Fe(OH)_{3(s)} + 2SO_4^{2-} + 2\ Ca^{2+} + 2\ Mg^{2+} + 4\ HCO_3^- \quad (4.3)$$

$$FeS_2 + 2\ CaMg(CO_3)_2 + 15/2\ H_2O_2 \rightarrow Fe(OH)_{3(s)} + 2SO_4^{2-} + 4\ H_2O + 2\ Ca^{2+} + 2\ Mg^{2+} + 4\ HCO_3^- \quad (4.4)$$

$$FeS_2 + 15/2\ S_2O_8^{2-} + 8\ H_2O \rightarrow Fe^{3+} + 17\ SO_4^{2-} + 16\ H^+ \quad (4.5)$$

The addition of $(NH_4)_2S_2O_8$ also promoted sulfate generation from pyrite oxidation, albeit to a lesser extent than did H_2O_2 (Figure 4.3). Sulfate in the presence of persulfate as shown in Figure 4.3 represents the amount of sulfate that originated from the sample rather than that contributed by persulfate. These calcluations consisted of 1) sulfate concentrations with only oxygen being the oxidant and 2) the difference between the measured sulfate with persulfate and that without scaled by a factor of 2/17 according to Reaction (4.5). While the standard redox potential is 2.1 V for $S_2O_8^{2-}$ and 1.8 V for H_2O_2 (Block et al., 2004), corresponding to numbers between 2.20 V and 2.32 V for $S_2O_8^{2-}$ and 2.15 V for H_2O_2 under the actual experimental conditions (SI), the kinetics of pyrite oxidation with $(NH_4)_2S_2O_8$ may be limited due to the considerably lower concentration of $S_2O_8^{2-}$ (5.8 meq/L) than that of H_2O_2 (1765 meq/L) used.

Additionally, sulfate produced from sulfide mineral oxidation will precipitate as barite when Ba is readily available. For example, for Sample 1 with H_2O_2 with 88.8 mg/L sulfate, a Ba concentration as low as 20 µg/L would be enough for the ion activity product $\{Ba^{2+}\}\{SO_4^{2-}\}$ to reach the barite solubility product ($10^{-9.97}$) (Nordstrom et al., 1990), leading to barite precipitation.

Dissolved As, Cr and U concentrations remained low at all oxidant levels (As up to 4.0 µg/L, Cr up to 6.0 µg/L and U up to 1.5 µg/L release observed). This may be due to their relatively low (mass) amounts in the original solid sample and potential for (re)sorption processes with solid particles in the suspension. Dissolved NPOC mobilized from Sample 1 increased slightly with H_2O_2, which is most likely due to decomposition in the presence of concentrated strong oxidant. The 12 mg/L NPOC represented only 6% of the TOC available in Sample 1, suggesting that the majority of TOC is effectively insoluble.

4.3.4 Solid:water Ratio Effect

The solid:water ratio affected the mobilization of different elements to varying degrees (Figure 4.4). The elevated sample loading promoted sulfate generation, increasing from 6.0 to 43.3 mg/L (Sample 1) and 1.4 to 6.7 mg/L (Sample 2) as the solid:water ratio increased from 1 to 10 g/L. The amount of dolomite in these samples (10 fold increase) was sufficient to neutralize the acidity produced from pyrite oxidation, stabilizing the suspension pH at 7.7 and 8.4, respectively. Ca and Mg concentrations increased with but not in proportion to the increased solid:water ratio, as they are controlled by dolomite dissolution equilibrium. Despite the large increase in sulfate generation, dissolved Fe concentrations did not scale with the solid:water ratio. At pH 8 Fe(II) will be rapidly oxidized to Fe(III) by oxygen and precipitate as indicated in Reaction (1). Ba and As concentrations from both samples, as well as U concentrations from

Sample 1 were slightly higher for the higher solid:water ratio, but overall, remained relatively low. Mn and Cr concentrations actually decreased for the elevated solid:water ratio as their concentrations are limited by Mn and Cr solubility and subject to subsequent adsorption reactions. Chloride, originating from sedimentary evaporation processes common for shale formation processes, scaled up proportionally to the solid:water ratio (Pettijohn, 1975). While Sodium (Na) concentrations were lower than (Sample 1) or comparable to (Sample 2) Ca and Mg concentrations at 1 g/L solid loading, they increased significantly at 10 g/L solid loading (Table S4.4), indicating that Na contribution to TDS may increase with increasing solid:water ratios.

4.3.5 Temperature Effect

The elevated temperature had a strong impact on pyrite oxidation rate with sulfate concentrations increasing from 6.0 to 59.3 mg/L (Sample 1) and from 1.4 to 6.6 mg/L (Sample 2) when temperature was raised from 22 to 80 ℃ (Figure 4.5). Except for sulfate, the temperature had little influence on most other elements. Interestingly, chemical additives at 80 ℃ (Experiment 13) did affect mobilization results to much greater extent that did just increasing the temperature. (Figure 4.5). Concentrations of Fe, Mn, As, U and Cr increased due to the low pH resulting from HCl. In particular, As and Cr mobilized from Sample 1 were as high as 97% (108.0 μg/L) and 70% (18.2 μg/L) of the theoretical maximum. Sulfate concentrations for all three chemical additives at 80 ℃ (Figure 4.5) are the difference between measured sulfate (714.4 mg/L in Sample 1 and 618.4 mg/L in Sample 2) and sulfate contributed by persulfate (560.1 mg/L); the persulfate at the concentration selected (2.9 mM) would decompose completely within 120 hours at 80 ℃ (Kolthoff and Miller, 1951).

4.3.6 Salt Effect

The addition of 10 g/L NaCl (0.17 M) increased the concentrations of Ca, Mg and Mn (Figure 4.6), but to a much less extent than lowering the pH. This is consistent with conclusions from a previous study that the dolomite dissolution rate is relatively independent of the ionic strengths between 0.1 and1.0 M (Pokrovsky et al., 2005). Within the experimental uncertainty, dissolution of most trace elements was not affected by the elevated salinity (Figure 4.6).

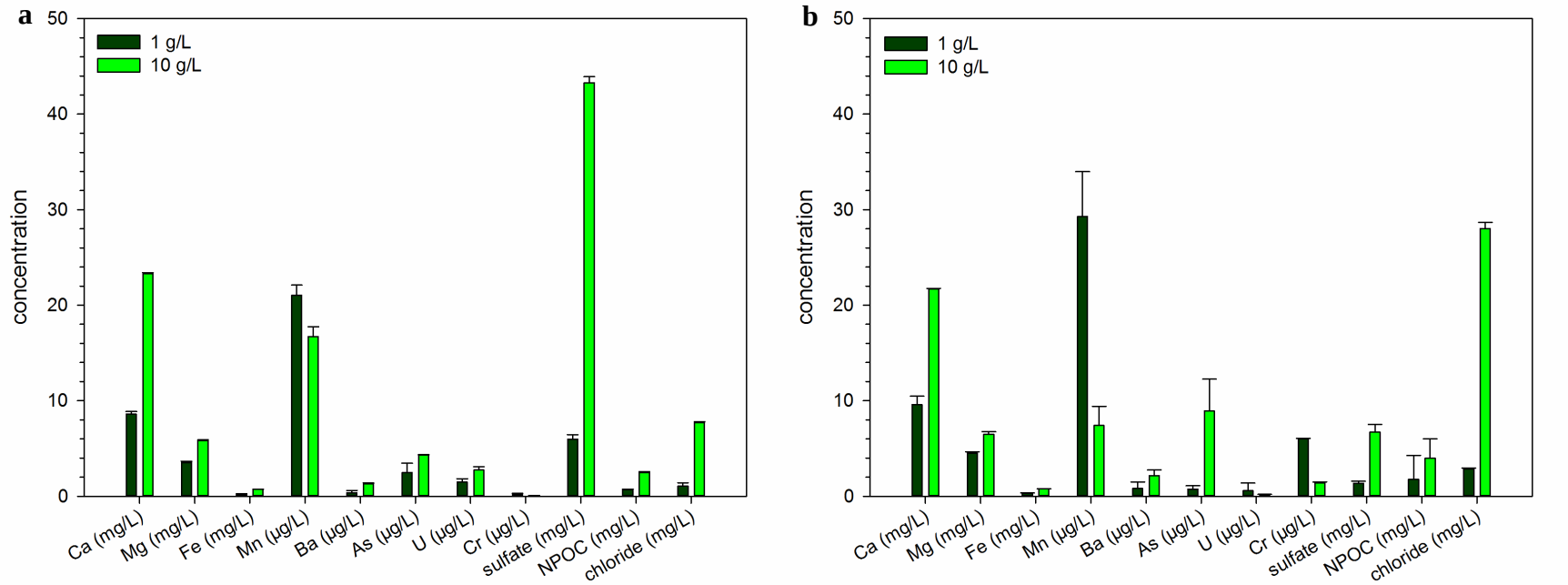

Figure 4.4 Metal, NPOC and anion concentrations with different solid:water ratios (Experiments 5 and 8) after 120 hours of reaction with (a) Sample 1 and (b) Sample 2. Experiments were performed at room temperature (22℃), without pH adjustment and open to the atmosphere. Data are shown as the average of the duplicates with error bars being the standard deviations.

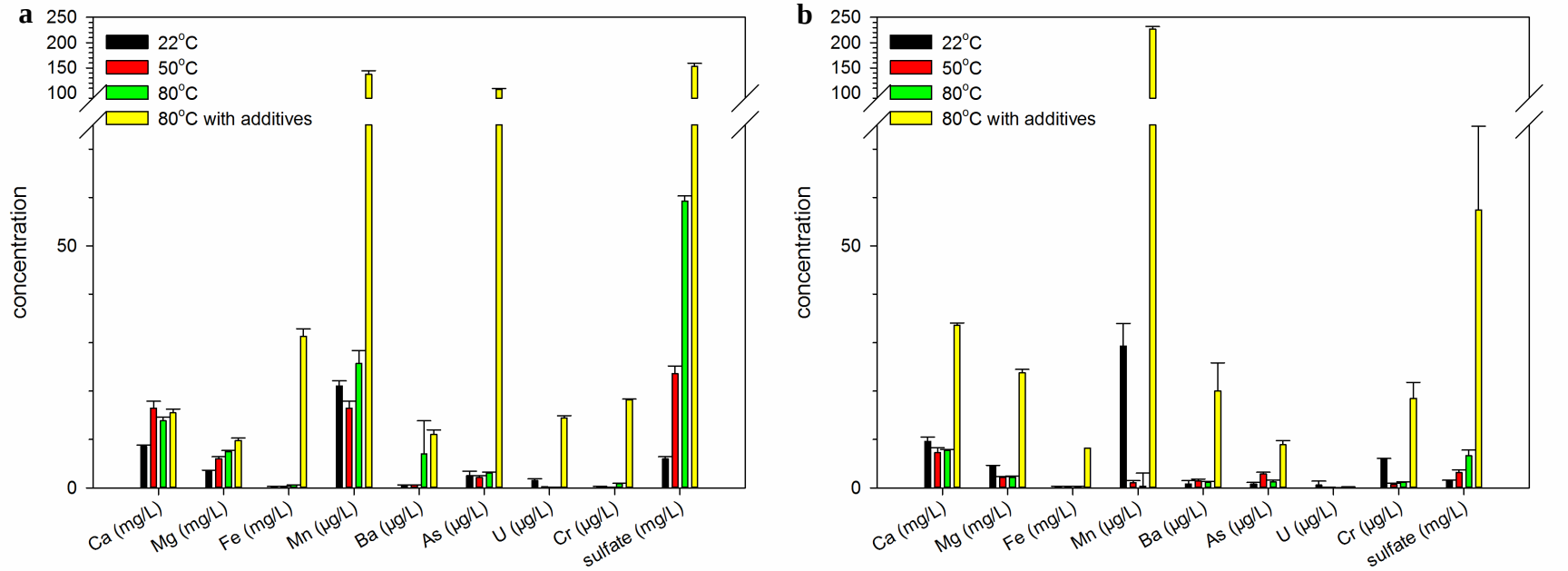

Figure 4.5 Metal, NPOC and sulfate concentrations at different temperatures (Experiments 5-7 and 13) after 120 hours of reaction with (a) Sample 1 and (b) Sample 2. Experiments were performed without pH adjustment and open to the atmosphere. Data are shown as the average of the duplicates with error bars being the standard deviations.

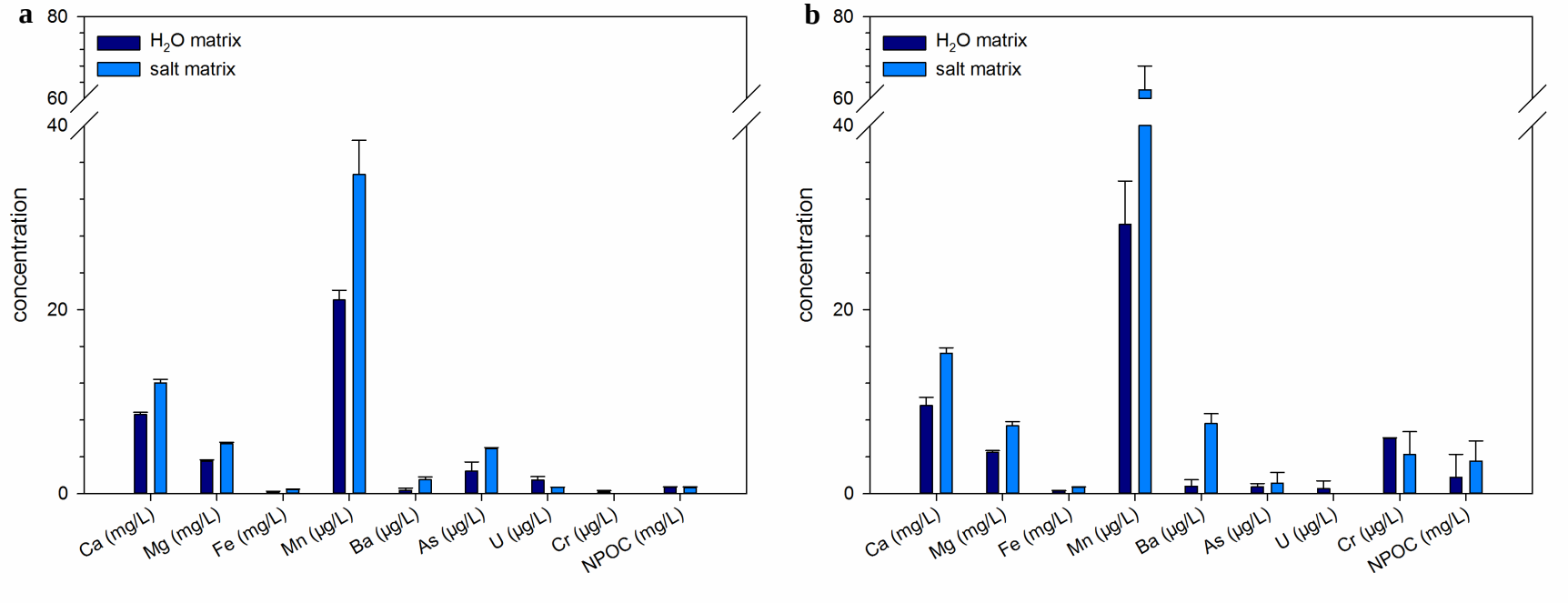

Figure 4.6 Metal and NPOC concentrations with and without salt (Experiments 5 and 9) after 120 hours of reaction with (a) Sample 1 and (b) Sample 2. Experiments were performed at room temperature (22℃), without pH adjustment and open to the atmosphere. Data are shown as the average of the duplicates with error bars being the standard deviations. A concentration of 10 g/L NaCl was used as the salt matrix.

4.4 Environmental Implications

Quantifying element release under varied hydraulic fracturing conditions, including varied water chemistries, will help in evaluating the potential environmental impacts of extraction operations and associated wastewater management issues. For these samples, pH is the most influential parameter affecting the mobility of most elements. Consequently, the use of strong acids to initiate and propagate fractures may lead to substantial element release. For shale formations rich in sulfide minerals, the introduction of oxygen and other oxidants can significantly increase the amount of produced sulfate over time. Further, if the formation has limited buffering capacity, sulfide mineral oxidation will lower the fluid pH, potentially leading to elevated concentrations of some regulated trace elements (such as As and Cr). For formations that contain Ba, potential precipitation of $BaSO_4$ upon sulfate generation could result in unwanted scale formation.

The release of elements from shale-fluid interactions will depend on the geochemistry of the shale, the constituents of formation water, and the overall composition of the fracking fluids. The degree to which the findings from this study can be related to actual flowback at the Bakken formation will be a function of the parameters used in actual operations. For example, the shale-fluid contact times at real hydrofracking sites will be longer than those selected in this study as the flowback water return usually occurs for several weeks (Vidic et al., 2013). The observation in this study that chloride concentrations scaled up linearly with sample loadings suggests a likely high TDS in the actual flowback waters with much higher solid:water ratios.

Acknowledgement

This study was supported by research funding from the McDonnell Academy Global Energy and Environmental Partnership. The authors thank the USGS Core Research Center for providing the samples from the Bakken Formation.

Chapter 4. Supporting Information

This supporting information includes 6 figures, 5 tables and text that facilitate the interpretation of the results in Chapter 4.

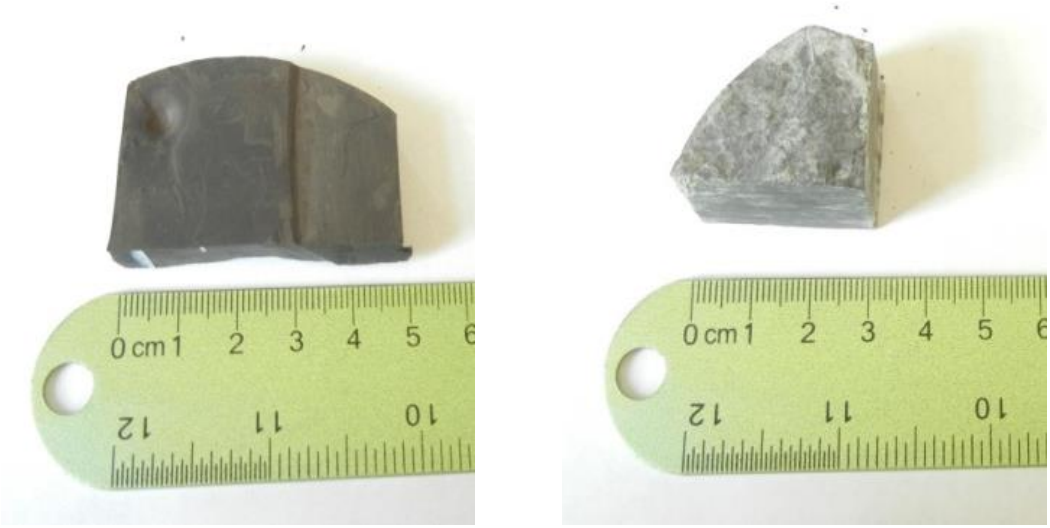

Figure S4.1 Images of core samples from Bakken Formation: (left) Sample 1 from 7454 ft (2272 m) and (right) Sample 2 from 7407 ft (2258 m)

Strong acid digestion procedure

Experiments were performed in triplicate. Three portions of 200 mg sample powders were weighed and introduced into digestion tubes, and 8 mL concentrated HNO_3 and 2 mL concentrated HCl were added. The resulting suspensions were heated in a digestion block for 4 hours at 100±0.5 °C and cooled overnight. Ultrapure water was added to the digestate to give a total volume of 50 mL. Aliquots of 10 mL supernatant were then taken by syringes and filtered through 0.22 μm PES membranes. Serial dilution was performed for the filtrate before analysis by ICP-MS (Agilent 7500ce). By design this acid digestion method will dissolve almost all elements except for those bound in silicate structures. Complete dissolution of silicates would have required the use of hydrofluoric acid. However, based on comparison with extractions of reference shale materials, the acid digestion method mobilizes essentially all of the elements of interest in this study. If a total digestion is necessary, then EPA Method 3052 that uses concentrated nitric acid and hydrofluoric acid should be used.

The extraction results with this method of two standard reference shale materials from USGS are listed in Table S4.1. The certificates of analysis of these two reference materials can be found at http://crustal.usgs.gov/geochemical_reference_standards/

Table S4.1 Recovery of standard reference materials from strong acid digestion

	SGR-1b			SBC-1		
	Experiment [a]	Standard [b]	Extractable (%) [c]	Experiment [a]	Standard [b]	Extractable (%) [c]
Major elements (%)						
Ca	7.63 ±0.06	8.38 ±0.17	91.0	2.76 ±0.03	2.95 ±0.01	93.6
Mg	4.36 ±0.03	4.44 ±0.2	98.1	1.89 ±0.03	2.6 ±0.01	72.6
Fe	2.87 ±0.03	3.03 ±0.14	94.6	7.81 ±0.10	9.71 ±0.02	80.4
Na	0.512 ±0.004	2.99 ±0.13	17.1	0.052 ±0.001	0.15	34.8
K	0.223 ±0.003	1.66 ±0.1	13.4	0.48 ±0.01	3.45 ±0.01	14.0
Al	4.34 ±0.05	6.52 ±0.21	66.5	50.12 ±1.06	21 ±0.04	238
Trace elements (mg/kg)						
As	57.74 ±0.51	67 ±5	86.2	26.23 ±0.19	25.7 ±0.7	102.1
Ba	223.16 ±2.01	290 ±40	77.0	381.22 ±6.16	788 ±7.7	48.4
Cd	0.56 ±0.01	0.9	62.8	0.18 ±0.01	0.4 ±0.02	45.4
Co	10.08 ±0.06	12 ±1.5	84.0	18.97 ±.30	22.7 ±0.3	83.6
Cr	27.54 ±0.40	30 ±3	91.8	45.25 ±0.78	109 ±1	41.5
Cu	62.15 ±0.69	66 ±9	94.2	28.10 ±1.40	31 ±0.6	90.7
Mn	228.50 ±1.53	267 ±34	85.6	1072.30 ±5.16	1162 ±7.7	92.3
Mo	31.60 ±0.29	35 ±0.9	90.3	2.48 ±0.45	2.4 ±0.07	103.5
Ni	30.46 ±0.20	29	105.0	75.67 ±1.20	82.8 ±0.8	91.4
Pb	41.28 ±1.37	38 ±4	108.6	27.24 ±0.66	35 ±0.3	77.8
Sb	2.27 ±0.05	3.4 ±.5	66.6	0.499 ±0.005	1.01 ±0.03	49.4
Se	3.52 ±0.19	3.5	100.5	1.71 ±0.34	NA	NA
U	3.88 ±0.09	5.4 ±0.4	71.9	2.22 ±0.03	5.76 ±0.11	38.6
V	104.58 ±0.59	130 ±6	80.4	81.17 ±1.24	220 ±1.4	36.9
Zn	125.42 ±1.94	74 ±9	169.5	234.03 ±6.22	186 ±1.7	125.8

[a] Values from the strong acid digestion described in this study.

[b] Values from USGS Certificates of Analysis determined by cooperating laboratories using a variety of analytical methods.

[c] Extractable (%) = Experiment / Standard

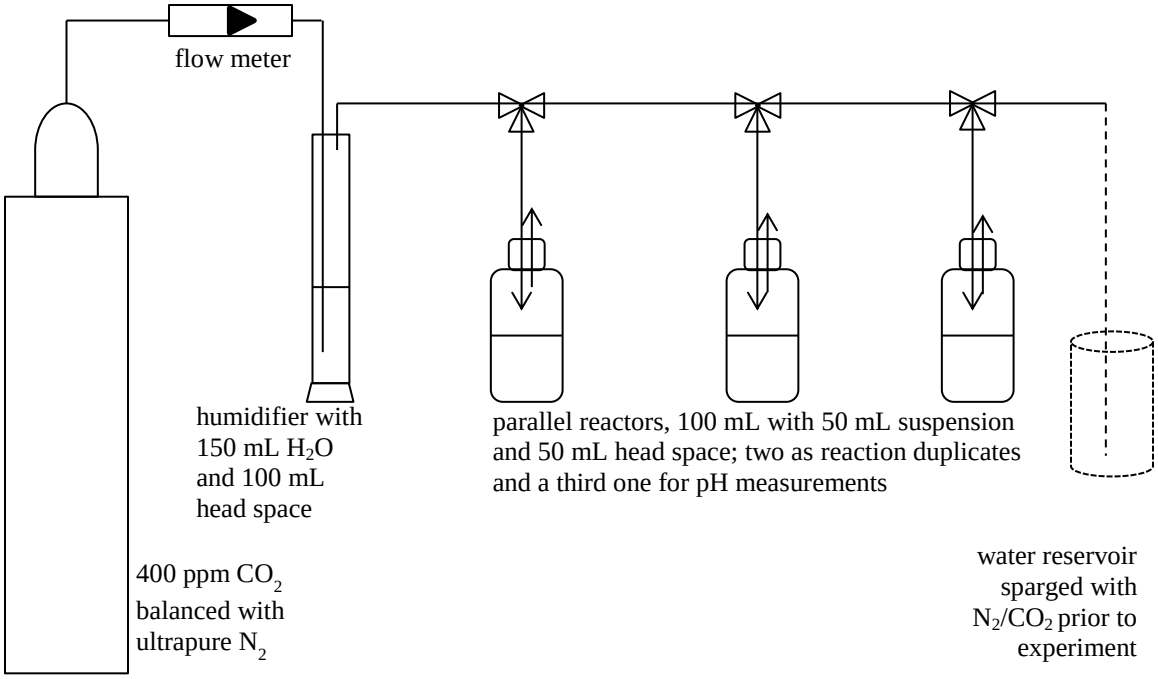

Figure S4.2 Illustration of experiment setup in anoxic conditions

Table S4.2 Detection limits of aqueous analysis

	detection limit [a]	unit
ICP-MS		
Ca	0.05	mg/L
Mg	0.01	mg/L
Fe	0.05	mg/L
K	0.01	mg/L
Na	0.04	mg/L
Al	0.004	mg/L
Mn	0.15	µg/L
As	[b] 0.50	µg/L
Ba	0.05	µg/L
Cd	0.05	µg/L
Co	0.07	µg/L
Cr	[b] 0.20	µg/L
Cu	1.90	µg/L
Mo	1.20	µg/L
Ni	2.50	µg/L
Pb	0.03	µg/L
Sb	0.04	µg/L
Se	0.40	µg/L
U	0.03	µg/L
V	0.08	µg/L
Zn	0.30	µg/L
ICP-OES		
As	3.0	µg/L
Cr	1.0	µg/L
IC		
chloride	0.1	mg/L
sulfate	0.2	mg/L
TOC		
NPOC	0.1	mg/L

[a] All detection limits are based on a 98% confidence level (3 standard deviations).

[b] These are detection limits for samples without high chloride concentrations. ICP-OES was used for Cr and As analysis for samples that were interfered by high chloride (2300 mg/L) on ICP-MS.

Table S4.3 Quantitative XRD analysis of core samples compared with reported ranges of Bakken sample properties

Mineral	Chemical formula	Mass fraction [a]		Reported [c]	
		Sample 1	Sample 2	Upper Bakken	Lower Bakken
quartz	SiO_2	0.2588	0.3393	0.34	0.51
dolomite	$CaMg(CO_3)_2$	0.0955	0.2115	0.09	0.05
illite	$(K,H_3O)(Al,Mg,Fe)_2(Si,Al)_4O_{10}[(OH)_2,(H_2O)]$	0.1390	0.1136	0.44 [d]	0.34 [d]
microcline	$KAlSi_3O_8$	0.4410	0.3217	0.03 [e]	0.04 [e]
pyrite	FeS_2	0.0657	0.0184	0.03	0.02
SUM		1.00	1.00		
Criteria of fit [b]	R_{wp}	19.00	21.36		
	R_p	13.99	16.03		
	GOF	4.18	4.59		

[a] These values were from quantitative XRD analysis by the Bruker Topas program. The sum represents only the crystalline phases of the samples.

[b] Criteria of fitting used here include: "R-weighted pattern", R_{wp}; "R-pattern", R_p; "Goodness of fit", GOF.

[c] Data from Mba and Prasad, 2010. Six samples from Upper Bakken Formation and five samples from Lower Bakken Formation were used.

[d] Minerals categorized as clays in Mba and Prasad, 2010.

[e] Minerals categorized as K-feldspar in Mba and Prasad, 2010.

Table S4.4 Mobilization results for all detectable elements

Part A. Sample 1 (7454 ft, organic-rich)

time (h)	Ca	Mg	Fe	Na	K	Al	As	Ba	Cd	Co	Cr	Cu	Mn	Mo	Ni	Pb	Sb	Se	U	V	Zn
	(mg/L)						(μg/L)														
Experiment 1: solid:water ratio=1 g/L, pH 4, 22 ℃, atmospheric																					
1	6.48	2.68	0.39	-	-	0.06	1.26	0.39	0.21	1.97	BDL	2.51	33.04	28.91	26.83	1.05	1.31	0.93	0.91	5.48	2.18
4	10.39	4.60	0.67	-	-	0.10	2.16	1.03	0.27	3.41	0.35	4.41	53.87	36.52	41.60	2.39	2.01	1.64	1.63	6.48	2.94
24	13.13	5.77	0.99	-	-	0.17	5.64	2.85	0.41	7.45	1.63	9.69	58.68	51.78	90.06	5.32	3.43	3.59	3.08	7.99	3.99
48	12.89	5.82	1.21	-	-	0.20	8.17	4.27	0.54	9.53	2.78	12.87	60.03	56.82	121.88	6.75	3.89	5.09	3.36	8.39	4.09
120	11.65	5.36	1.39	-	-	0.31	9.54	8.68	0.59	10.68	5.58	20.48	57.00	51.49	146.74	8.31	4.09	5.95	2.75	8.28	8.72
Experiment 2: solid:water ratio=1 g/L, pH 8, 22 ℃, atmospheric																					
1	1.00	0.25	BDL	-	-	0.03	0.71	0.15	0.32	0.27	BDL	BDL	1.83	40.12	6.57	0.03	0.86	0.89	0.08	2.39	1.57
4	2.14	0.62	0.11	-	-	0.07	1.35	0.85	0.49	0.95	0.46	BDL	5.39	60.29	19.53	0.27	1.58	1.85	0.17	3.72	5.11
24	4.14	1.46	0.13	-	-	0.07	2.51	1.85	0.78	2.56	1.41	BDL	11.75	92.58	46.20	0.17	2.50	2.34	0.28	4.36	0.88
48	5.25	1.99	0.15	-	-	0.07	2.96	2.63	0.96	2.90	2.60	BDL	15.74	111.30	54.94	0.11	2.95	3.25	0.39	4.42	1.67
120	7.35	3.10	0.22	-	-	0.08	4.06	4.58	1.29	2.65	5.24	BDL	23.00	144.99	53.69	0.09	3.55	5.09	0.60	5.83	0.71
Experiment 3: solid:water ratio=1 g/L, unadjusted pH, 22 ℃, anoxic																					
120	7.92	3.15	0.20	1.09	0.79	1.29	4.03	20.05	0.78	2.33	0.21	2.70	24.22	165.41	40.48	0.28	5.89	7.97	0.52	4.21	3.76
Experiment 4: solid:water ratio=1 g/L, pH 8, 22 ℃, 3% H_2O_2																					
1	1.35	0.32	0.09	-	-	BDL	1.43	0.11	1.45	2.85	1.50	BDL	4.85	212.27	63.23	0.16	1.06	9.33	0.07	6.50	0.88
4	2.20	0.75	0.06	-	-	0.02	2.33	0.22	1.90	3.08	1.82	BDL	7.84	279.91	57.59	BDL	1.99	15.42	0.05	9.54	0.68
24	3.26	1.36	0.19	-	-	0.14	3.56	0.64	2.34	6.27	2.86	2.00	2.62	346.65	34.07	0.13	4.90	21.19	0.14	22.45	1.03
48	3.97	1.81	0.27	-	-	0.24	3.34	1.01	2.42	7.80	3.43	BDL	2.39	348.97	40.23	0.18	5.71	21.73	0.17	28.58	1.09
120	5.92	3.00	0.45	-	-	0.37	3.88	2.48	2.47	10.51	4.50	2.22	3.06	359.08	57.67	0.28	6.37	22.39	0.35	41.03	1.20
Experiment 5: solid:water ratio=1 g/L, unadjusted pH, 22 ℃, atmospheric																					
1	0.89	0.22	BDL	0.64	0.30	0.20	0.59	0.07	0.20	0.15	BDL	BDL	0.32	39.16	4.92	BDL	0.65	0.65	0.15	1.66	1.54
4	2.02	0.61	0.06	0.69	0.39	0.39	1.05	0.13	0.26	0.73	BDL	BDL	3.64	54.14	16.34	0.06	1.23	1.17	0.23	2.51	0.70
24	4.97	1.89	0.12	0.92	0.55	0.89	1.85	0.24	0.47	2.74	BDL	BDL	14.35	93.89	52.04	0.20	2.59	3.02	0.38	3.62	1.20

time (h)	Ca	Mg	Fe	Na	K	Al	As	Ba	Cd	Co	Cr	Cu	Mn	Mo	Ni	Pb	Sb	Se	U	V	Zn
	(mg/L)						(µg/L)														
48	6.56	2.61	0.18	1.07	0.66	1.32	2.02	0.32	0.60	2.99	BDL	BDL	18.60	120.26	60.35	0.28	3.31	4.36	0.65	4.26	1.23
120	8.58	3.54	0.23	1.34	0.95	1.43	2.47	0.47	0.84	1.94	0.20	BDL	21.03	170.80	41.38	0.17	4.32	6.39	1.49	4.80	1.23
Experiment 6: solid:water ratio=1 g/L, unadjusted pH, 50 ℃, atmospheric																					
120	16.5	6.04	0.33	1.49	1.75	0.99	2.16	0.57	1.28	0.99	BDL	BDL	16.48	256.30	9.82	BDL	4.95	6.79	0.27	4.97	1.81
Experiment 7: solid:water ratio=1 g/L, unadjusted pH, 80 ℃, atmospheric																					
120	13.8	7.51	0.62	0.90	3.33	0.02	3.05	6.99	1.44	1.46	0.91	BDL	25.70	175.69	16.64	BDL	2.70	11.41	0.08	7.52	1.77
Experiment 8: solid:water ratio=10 g/L, unadjusted pH, 22 ℃, atmospheric																					
1	4.23	0.64	0.11	6.80	1.88	7.60	4.92	0.27	1.95	BDL	BDL	*	BDL	468.22	*	0.17	7.98	11.27	0.14	18.07	1.38
4	7.18	1.08	0.20	7.13	2.33	8.13	5.98	0.34	2.68	0.35	BDL	*	1.35	639.76	*	0.07	13.24	17.20	0.27	13.44	3.39
24	15.5	3.23	0.45	7.78	3.19	3.13	2.29	0.64	3.88	4.20	BDL	*	15.65	955.56	*	BDL	22.75	25.23	0.71	3.53	4.39
48	18.9	4.29	0.56	8.33	3.55	2.53	2.32	0.78	4.67	3.35	BDL	*	18.08	1168.4	*	BDL	26.33	29.16	1.07	3.39	2.65
120	23.3	5.82	0.71	9.84	4.77	2.58	4.33	1.30	6.90	1.77	BDL	*	16.72	1726.1	*	1.06	34.30	38.05	2.75	9.26	1.96
Experiment 9: solid:water ratio=1 g/L, unadjusted pH, 22 ℃, atmospheric, 10 g/L NaCl																					
1	1.44	0.45	0.07	-	0.63	BDL	2.73	14.37	0.33	0.97	0.33	47.67	3.01	49.94	16.64	BDL	0.80	1.39	BDL	2.16	BDL
4	3.17	1.11	0.13	-	0.73	0.12	3.97	31.73	0.51	1.10	1.02	51.41	8.83	79.38	31.14	BDL	1.51	2.82	0.07	3.10	BDL
24	7.15	3.00	0.27	-	0.83	0.83	4.59	71.53	0.78	3.54	BDL	56.25	22.88	123.68	74.47	0.08	2.90	5.19	0.25	3.44	BDL
48	9.34	4.04	0.37	-	0.94	0.49	4.72	93.45	1.00	4.18	BDL	55.12	29.22	159.46	92.62	BDL	3.91	6.41	0.39	4.10	0.69
120	12.0	5.43	0.46	-	1.10	1.35	4.91	120.35	1.39	3.57	BDL	57.32	34.68	216.12	87.77	BDL	5.03	8.40	0.69	5.23	BDL
Experiment 10: solid:water ratio=1 g/L, pH 1.5, 22 ℃, atmospheric, 66 mM HCl																					
1	16.0	6.89	1.34	0.60	6.89	0.21	9.49	1.82	0.55	4.28	4.72	11.50	72.15	66.01	47.99	16.42	5.95	4.13	4.41	13.79	17.45
4	17.6	7.65	1.70	0.65	7.65	0.30	13.28	2.27	0.83	7.50	3.88	19.55	79.91	90.89	76.42	21.62	8.59	6.29	5.57	16.59	19.53
24	18.3	8.08	3.07	0.78	8.08	0.60	24.67	3.68	1.21	16.51	3.44	37.58	84.50	140.60	200.62	35.06	11.83	11.22	6.97	24.75	21.68
48	18.5	8.19	4.36	0.88	8.19	0.80	31.82	4.46	1.40	19.29	3.20	45.22	86.70	156.77	253.43	40.37	12.40	14.26	7.33	29.34	24.32
120	18.6	8.42	7.07	0.99	8.42	1.26	44.02	5.73	1.60	21.52	3.24	56.66	91.88	172.53	299.24	46.89	12.16	17.32	7.67	37.23	27.66
Experiment 11: solid:water ratio=1 g/L, pH 4, 22 ℃, atmospheric, 1 mM citrate																					
1	7.9	3.29	0.68	-	-	0.13	2.89	1.04	0.38	2.21	0.35	BDL	36.73	41.28	29.58	6.81	2.39	1.74	2.63	7.74	3.98
4	11.5	4.94	0.96	-	-	0.17	4.69	1.59	0.51	3.87	0.64	1.91	52.39	58.13	45.12	13.05	3.88	2.60	4.17	9.72	4.35

time (h)	Ca	Mg	Fe	Na	K	Al	As	Ba	Cd	Co	Cr	Cu	Mn	Mo	Ni	Pb	Sb	Se	U	V	Zn
	(mg/L)						(µg/L)														
24	14.0	5.96	1.58	-	-	0.25	11.85	2.82	0.85	8.99	1.90	8.10	63.10	95.30	102.83	24.23	7.83	5.63	6.16	13.64	5.28
48	14.2	6.04	2.01	-	-	0.30	17.06	3.37	1.01	11.73	2.97	11.10	64.58	112.01	144.68	28.30	9.65	8.18	6.48	15.61	5.74
120	14.0	5.97	2.97	-	-	0.34	25.67	4.56	1.26	14.45	5.30	16.23	64.61	132.81	196.51	34.54	11.81	11.27	6.59	17.77	6.13
Experiment 12: solid:water ratio=1 g/L, pH 8, 22 ℃, atmospheric, 2.9 mM persulfate																					
1	6.13	2.20	0.21	-	-	0.03	1.26	1.52	0.29	0.49	BDL	BDL	20.44	45.61	12.47	0.07	0.79	4.90	0.32	3.03	5.16
4	7.54	2.83	0.25	-	-	0.03	1.81	1.42	0.44	1.04	BDL	BDL	5.85	70.17	21.64	BDL	1.27	5.37	0.21	4.02	4.93
24	10.7	4.44	0.36	-	-	0.04	2.73	1.48	0.77	2.23	BDL	BDL	14.94	127.45	46.89	BDL	2.22	7.59	0.27	4.31	4.88
48	12.8	5.56	0.43	-	-	0.05	2.70	1.56	0.98	2.35	0.24	BDL	21.78	158.36	54.81	BDL	2.65	8.64	0.25	4.26	5.14
120	15.9	7.28	0.52	-	-	0.03	2.15	2.00	1.21	1.85	BDL	BDL	29.48	201.41	49.93	BDL	3.25	10.26	0.13	4.62	5.13
Experiment 13: solid:water ratio=1 g/L, pH 1.5, 80 ℃, atmospheric, 66 mM HCl, 1 mM citrate, 2.9 mM persulfate																					
120	15.5	9.8	31.3	1.1	10.1	7.5	108.0	11.0	2.5	32.4	18.2	119.0	137.8	335.0	438.0	61.6	19.0	24.7	14.5	208.6	81.3

Part B. Sample 2 (7407 ft, organic-poor)

time (h)	Ca	Mg	Fe	Na	K	Al	As	Ba	Cd	Co	Cr	Cu	Mn	Mo	Ni	Pb	Sb	Se	U	V	Zn
	(mg/L)						(µg/L)														
Experiment 1: solid:water ratio=1 g/L, pH 4, 22 ℃, atmospheric																					
1	16.20	8.65	1.24	-	-	0.15	BDL	1.38	BDL	2.40	0.39	3.39	102.19	BDL	5.08	0.36	BDL	BDL	0.06	1.16	8.43
4	34.94	20.74	2.06	-	-	0.23	BDL	2.55	BDL	3.38	0.84	3.79	183.25	BDL	7.46	0.91	0.04	BDL	0.08	1.25	9.40
24	39.69	24.02	2.19	-	-	0.31	0.61	5.63	0.06	4.52	1.94	4.78	202.02	BDL	10.01	1.60	0.06	BDL	0.09	1.29	11.01
48	38.20	22.91	2.03	-	-	0.50	0.79	12.06	0.08	4.84	2.96	4.68	193.68	BDL	10.65	1.79	0.08	BDL	0.09	1.51	10.90
120	41.97	25.04	2.44	-	-	0.80	2.23	35.53	0.21	6.41	7.10	5.41	211.04	BDL	15.86	2.18	0.11	5.50	0.11	2.71	11.87
Experiment 2: solid:water ratio=1 g/L, pH 8, 22 ℃, atmospheric																					
1	1.53	0.56	BDL	-	-	0.03	0.53	0.12	BDL	0.45	0.28	2.31	6.32	BDL	2.84	0.52	0.07	4.67	BDL	0.51	5.84
4	2.68	1.08	0.08	-	-	0.04	0.61	0.73	BDL	0.75	0.40	2.42	12.62	BDL	3.25	0.71	0.09	4.88	BDL	0.55	7.47
24	5.55	2.44	0.18	-	-	0.04	0.77	5.84	0.08	1.38	1.38	2.54	29.07	BDL	4.27	0.98	0.14	4.69	BDL	0.92	7.03
48	6.39	2.98	0.21	-	-	0.05	0.85	11.08	0.13	1.48	2.30	2.58	33.27	BDL	4.66	1.04	0.14	4.68	BDL	1.27	6.92

time (h)	Ca	Mg	Fe	Na	K	Al	As	Ba	Cd	Co	Cr	Cu	Mn	Mo	Ni	Pb	Sb	Se	U	V	Zn
	(mg/L)						(µg/L)														
120	9.51	4.87	0.33	-	-	0.04	1.39	28.61	0.22	1.61	5.39	2.70	48.72	BDL	5.23	1.12	0.20	5.01	BDL	2.21	7.18
Experiment 3: solid:water ratio=1 g/L, unadjusted pH, 22 ℃, anoxic																					
120	7.61	3.91	0.24	3.95	2.06	0.38	0.74	222.41	BDL	3.86	BDL	45.65	27.48	BDL	2.83	1.46	0.22	BDL	0.06	18.07	7.27
Experiment 4: solid:water ratio=1 g/L, pH 8, 22 ℃, 3% H_2O_2																					
1	2.76	1.19	0.11	-	-	BDL	BDL	BDL	BDL	6.01	0.90	43.29	9.84	BDL	4.53	2.74	BDL	BDL	0.06	11.08	2.90
4	5.35	2.56	0.18	-	-	0.00	BDL	0.09	BDL	12.53	1.48	43.54	20.34	BDL	6.42	2.11	0.12	BDL	0.07	14.08	2.25
24	9.41	4.85	0.30	-	-	0.10	0.75	0.21	BDL	23.16	2.10	45.15	26.77	1.59	8.29	0.99	0.36	BDL	0.06	18.66	2.63
48	11.29	5.89	0.36	-	-	0.02	0.90	0.27	BDL	24.66	2.39	43.55	24.06	1.92	8.22	0.75	0.55	BDL	0.05	20.79	2.38
120	13.78	7.21	0.43	-	-	0.07	1.09	0.57	BDL	21.50	2.92	43.19	15.42	2.36	7.46	0.96	0.76	BDL	0.04	24.24	2.57
Experiment 5: solid:water ratio=1 g/L, unadjusted pH, 22 ℃, atmospheric																					
1	1.00	0.32	BDL	3.18	1.47	0.02	BDL	BDL	BDL	0.12	BDL	BDL	0.71	BDL	BDL	BDL	BDL	BDL	0.04	0.53	BDL
4	2.24	0.88	0.06	3.27	1.60	0.04	BDL	0.06	BDL	0.18	BDL	BDL	4.18	BDL	BDL	BDL	BDL	BDL	0.09	0.57	BDL
24	6.13	2.87	0.21	3.97	1.88	0.09	BDL	0.29	BDL	0.57	0.32	BDL	21.47	BDL	BDL	BDL	0.05	BDL	0.26	0.72	BDL
48	7.64	3.62	0.26	4.85	2.04	0.13	0.51	0.46	BDL	0.61	0.43	BDL	26.33	BDL	BDL	BDL	0.07	BDL	0.38	0.85	BDL
120	9.58	4.50	0.32	6.68	2.30	0.10	0.76	0.81	BDL	0.54	0.55	BDL	29.27	BDL	BDL	BDL	0.11	BDL	0.57	1.12	BDL
Experiment 6: solid:water ratio=1 g/L, unadjusted pH, 50 ℃, atmospheric																					
120	7.28	2.16	0.28	10.29	10.05	0.49	2.86	1.38	BDL	0.15	0.69	BDL	1.06	BDL	BDL	BDL	0.26	0.29	0.12	3.20	BDL
Experiment 7: solid:water ratio=1 g/L, unadjusted pH, 80 ℃, atmospheric																					
120	7.78	2.16	0.28	2.94	3.06	0.33	1.23	1.17	0.33	BDL	1.16	BDL	0.36	4.69	BDL	BDL	0.19	BDL	BDL	2.77	BDL
Experiment 8: solid:water ratio=10 g/L, unadjusted pH, 22 ℃, atmospheric																					
1	3.51	0.77	0.13	21.72	5.73	0.15	1.35	0.06	0.06	0.08	1.17	2.62	BDL	4.25	BDL	0.32	0.11	6.90	BDL	4.21	0.94
4	5.40	1.23	0.21	22.29	6.45	0.23	2.53	0.23	0.06	0.19	1.30	2.69	0.52	4.99	BDL	0.33	0.19	6.52	BDL	6.25	1.05
24	12.98	3.51	0.48	23.97	7.88	0.17	2.71	0.81	0.07	0.55	1.42	2.72	7.88	6.02	3.08	0.31	0.35	6.84	0.03	4.67	1.18
48	16.44	4.82	0.59	26.55	8.77	0.13	3.63	1.18	0.08	0.56	1.37	2.67	10.56	6.55	3.06	0.29	0.42	6.68	0.07	5.54	1.42
120	21.69	6.48	0.78	35.35	9.85	0.13	8.95	2.16	0.08	0.45	1.37	2.55	7.40	7.40	2.65	0.31	0.59	6.61	0.18	9.61	1.04
Experiment 9: solid:water ratio=1 g/L, unadjusted pH, 22 ℃, atmospheric, 10 g/L NaCl																					
1	2.44	0.88	0.08	-	1.70	0.03	1.71	1.85	BDL	BDL	8.24	6.92	2.67	BDL	3.48	BDL	BDL	BDL	BDL	2.57	BDL

time (h)	Ca	Mg	Fe	Na	K	Al	As	Ba	Cd	Co	Cr	Cu	Mn	Mo	Ni	Pb	Sb	Se	U	V	Zn
	(mg/L)						(μg/L)														
4	4.74	1.81	0.28	-	3.65	0.04	8.97	2.57	0.06	0.25	22.90	8.29	10.15	BDL	2.61	BDL	BDL	BDL	BDL	7.19	BDL
24	9.54	4.68	0.42	-	2.42	0.03	2.30	2.93	BDL	0.89	9.08	8.42	45.69	BDL	3.85	BDL	BDL	BDL	BDL	2.68	BDL
48	12.04	6.00	0.54	-	3.29	0.04	1.37	4.44	BDL	1.02	6.00	9.50	57.14	BDL	3.84	BDL	BDL	BDL	BDL	2.08	BDL
120	15.27	7.38	0.68	-	3.95	0.14	1.14	7.62	BDL	0.81	4.25	10.70	62.17	BDL	3.71	BDL	BDL	BDL	BDL	2.28	BDL
Experiment 10: solid:water ratio=1 g/L, pH 1.5, 22 ℃, atmospheric, 66 mM HCl																					
1	35.91	20.07	2.12	1.81	21.10	0.47	BDL	2.73	BDL	5.15	BDL	19.80	152.20	BDL	11.04	3.92	0.14	0.63	BDL	5.22	21.79
4	36.50	20.50	2.21	1.90	21.56	0.57	BDL	2.99	BDL	6.03	BDL	24.69	155.18	BDL	13.12	4.69	0.14	0.85	BDL	6.70	23.56
24	36.85	20.74	2.31	2.09	21.82	0.76	0.53	3.61	BDL	7.02	BDL	29.35	157.56	BDL	15.44	5.06	0.15	0.68	BDL	8.12	24.71
48	37.38	20.98	2.46	2.34	22.08	0.94	1.29	4.22	BDL	7.55	BDL	30.22	159.88	BDL	16.71	5.37	0.19	0.77	BDL	9.06	25.77
120	38.29	21.36	2.80	3.36	22.47	1.47	2.11	6.44	BDL	8.31	1.55	31.16	162.82	BDL	18.69	5.96	0.19	0.75	BDL	10.32	26.61
Experiment 11: solid:water ratio=1 g/L, pH 4, 22 ℃, atmospheric, 1 mM citrate																					
1	19.44	10.36	1.57	-	-	0.36	0.86	2.05	0.05	3.05	0.75	3.75	115.99	BDL	8.60	1.73	0.14	5.15	0.09	2.37	36.32
4	34.22	20.12	2.27	-	-	0.38	1.18	4.04	0.07	4.09	1.26	4.07	179.04	BDL	12.34	2.64	0.15	5.78	0.11	2.93	13.20
24	38.91	23.26	2.55	-	-	0.45	1.85	8.95	0.10	5.57	2.83	4.75	195.17	BDL	16.17	3.39	0.20	5.91	0.12	3.64	14.08
48	37.41	22.45	2.48	-	-	0.46	2.13	11.97	0.13	5.84	4.07	4.54	188.29	BDL	16.82	3.49	0.20	5.89	0.12	3.95	13.64
120	42.96	25.43	2.96	-	-	0.62	3.43	24.51	0.28	7.76	8.30	5.26	214.80	1.57	24.26	4.23	0.26	8.29	0.14	5.72	16.63
Experiment 12: solid:water ratio=1 g/L, pH 8, 22 ℃, atmospheric, 2.9 mM persulfate																					
1	3.16	1.13	0.12	-	-	0.09	BDL	1.71	0.05	0.77	0.32	2.19	7.40	BDL	BDL	0.06	0.06	5.30	BDL	1.30	9.26
4	3.91	1.54	0.14	-	-	0.07	BDL	2.09	BDL	0.77	0.34	2.05	8.34	BDL	BDL	BDL	0.06	4.60	BDL	1.35	7.78
24	6.17	2.77	0.22	-	-	0.08	BDL	4.97	0.07	0.94	0.91	1.96	1.74	BDL	BDL	BDL	0.08	4.73	BDL	1.58	9.01
48	7.63	3.56	0.27	-	-	0.09	BDL	9.74	0.09	0.57	1.63	1.98	0.62	BDL	2.51	BDL	0.10	5.15	BDL	1.80	8.61
120	11.91	6.40	0.51	-	-	0.63	1.24	35.73	0.20	0.68	3.84	1.98	2.94	BDL	3.17	BDL	0.14	5.80	0.05	3.15	8.23
Experiment 13: solid:water ratio=1 g/L, pH 1.5, 80 ℃, atmospheric, 66 mM HCl, 1 mM citrate, 2.9 mM persulfate																					
120	33.60	23.78	8.25	2.91	28.57	8.09	13.44	20.05	0.07	11.81	35.13	51.06	227.41	4.54	40.55	12.65	0.30	0.69	0.21	26.62	61.60

Data are shown as average of the duplicates.

"BDL" means "below detection limit".

"-" for Na indicates the use of NaOH on the autotitrator or the addition of NaCl, for K indicates excessive K due to pH monitoring over time on the autotitrator.

"*" indicates unreliable results due to the status of the analytical instrument.

Table S5. Percentages of element mobilization after 120 hour reaction

Part A. Sample 1 (7454 ft, organic-rich)

	Ca	Mg	Fe	Na	K	Al	As	Ba	Cd	Co	Cr	Cu	Mn	Mo	Ni	Pb	Sb	Se	U	V	Zn
Experiment 1: solid:water ratio=1 g/L, pH 4, 22 ℃, atmospheric																					
	68.6	53.8	4.1	-	-	0.5	8.7	53.2	19.6	31.4	21.9	18.1	40.1	9.8	18.8	12.5	23.6	17.9	4.0	2.5	9.6
Experiment 2: solid:water ratio=1 g/L, pH 8, 22 ℃, atmospheric																					
	43.3	31.1	0.6	-	-	0.1	3.7	28.0	42.5	7.8	20.6	BDL	16.2	27.5	6.9	0.1	20.5	15.3	0.9	1.7	0.8
Experiment 3: solid:water ratio=1 g/L, unadjusted pH, 22 ℃, anoxic																					
	46.6	31.6	0.6	12.5	1.7	1.9	3.7	122.7	25.7	6.8	0.8	2.4	17.1	31.3	5.2	0.4	34.0	24.0	0.8	1.3	4.1
Experiment 4: solid:water ratio=1 g/L, pH 8, 22 ℃, 3% H_2O_2																					
	34.8	30.1	1.3	-	-	0.5	3.5	15.2	81.7	30.9	17.7	2.0	2.2	68.0	7.4	0.4	36.7	67.4	0.5	12.3	1.3
Experiment 5: solid:water ratio=1 g/L, unadjusted pH, 22 ℃, atmospheric																					
	50.5	35.5	0.7	15.4	2.1	2.1	2.3	2.9	27.7	5.7	0.8	BDL	14.8	32.3	5.3	0.3	24.9	19.2	2.2	1.4	1.4
Experiment 6: solid:water ratio=1 g/L, unadjusted pH, 50 ℃, atmospheric																					
	97.0	60.5	1.0	17.1	3.8	1.5	2.0	3.5	42.1	2.9	BDL	BDL	11.6	48.5	1.3	BDL	28.5	20.4	0.4	1.5	2.0
Experiment 7: solid:water ratio=1 g/L, unadjusted pH, 80 ℃, atmospheric																					
	81.4	75.2	1.8	10.3	7.2	0.0	2.8	42.8	47.6	4.3	3.5	BDL	18.1	33.3	2.1	BDL	15.6	34.4	0.1	2.3	2.0
Experiment 8: solid:water ratio=10 g/L, unadjusted pH, 22 ℃, atmospheric																					
	137.3	58.4	2.1	112.9	10.3	3.8	4.0	7.9	227.8	5.2	BDL	*	11.8	326.9	*	1.6	197.6	114.6	4.1	2.8	2.2
Experiment 9: solid:water ratio=1 g/L, unadjusted pH, 22 ℃, atmospheric, 10 g/L NaCl																					
	70.9	54.5	1.3	-	2.4	2.0	4.5	736.8	45.8	10.5	BDL	50.7	24.4	40.9	11.2	BDL	29.0	25.3	1.0	1.6	BDL
Experiment 10: solid:water ratio=1 g/L, pH 1.5, 22 ℃, atmospheric, 66 mM HCl																					
	109.7	84.4	20.8	11.4	18.1	1.9	40.3	35.1	52.9	63.2	12.7	50.2	64.7	32.7	38.3	70.3	70.1	52.2	11.3	11.1	30.5
Experiment 11: solid:water ratio=1 g/L, pH 4, 22 ℃, atmospheric, 1 mM citrate																					
	82.1	59.9	8.7	-	-	0.5	23.5	27.9	41.6	42.4	20.8	14.4	45.5	25.2	25.2	51.8	68.1	33.9	9.7	5.3	6.8
Experiment 12: solid:water ratio=1 g/L, pH 8, 22 ℃, atmospheric, 2.9 mM persulfate																					
	93.5	72.9	1.5	-	-	0.1	2.0	12.2	40.0	5.4	BDL	BDL	20.8	38.1	6.4	BDL	18.7	30.9	0.2	1.4	5.7
Experiment 13: solid:water ratio=1 g/L, pH 1.5, 80 ℃, atmospheric, 66 mM HCl, 1 mM citrate, 2.9 mM persulfate																					
	91.3	98.0	91.9	12.8	21.7	11.0	98.7	67.5	83.2	95.1	71.4	105.4	97.0	63.4	56.1	92.4	109.6	74.4	21.3	62.4	89.7

Part B. Sample 2 (7407 ft, organic-poor)

	Ca	Mg	Fe	Na	K	Al	As	Ba	Cd	Co	Cr	Cu	Mn	Mo	Ni	Pb	Sb	U	V	Zn
Experiment 1: solid:water ratio=1 g/L, pH 4, 22 ℃, atmospheric																				
	104.5	107.2	27.0	-	-	1.4	19.4	251.4	544.9	61.9	41.9	12.5	89.3	BDL	45.4	16.7	33.2	34.7	13.7	12.8
Experiment 2: solid:water ratio=1 g/L, pH 8, 22 ℃, atmospheric																				
	23.7	20.8	3.7	-	-	0.1	12.1	202.5	583.9	15.6	31.8	6.2	20.6	BDL	15.0	8.6	61.4	BDL	11.2	7.7
Experiment 3: solid:water ratio=1 g/L, unadjusted pH, 22 ℃, anoxic																				
	18.9	16.8	2.7	19.7	4.3	0.7	6.5	1573.6	BDL	37.3	BDL	105.6	11.6	BDL	8.1	11.1	66.6	20.5	91.6	7.8
Experiment 4: solid:water ratio=1 g/L, pH 8, 22 ℃, 3% H_2O_2																				
	34.3	30.9	4.8	-	-	0.1	9.5	4.0	BDL	207.5	17.2	99.9	6.5	37.8	21.4	7.3	231.5	12.0	122.8	2.8
Experiment 5: solid:water ratio=1 g/L, unadjusted pH, 22 ℃, atmospheric																				
	23.9	19.3	3.5	33.3	4.9	0.2	6.6	5.8	BDL	5.2	3.3	BDL	12.4	BDL	BDL	BDL	33.1	183.9	5.7	BDL
Experiment 6: solid:water ratio=1 g/L, unadjusted pH, 50 ℃, atmospheric																				
	18.1	9.3	3.1	51.2	21.2	0.9	24.9	9.8	BDL	1.4	4.0	BDL	0.4	BDL	BDL	BDL	78.7	37.4	16.2	BDL
Experiment 7: solid:water ratio=1 g/L, unadjusted pH, 80 ℃, atmospheric																				
	19.4	9.2	3.0	14.6	6.5	0.6	10.7	8.3	866.9	BDL	6.8	BDL	0.2	75.1	BDL	BDL	57.5	BDL	14.0	BDL
Experiment 8: solid:water ratio=10 g/L, unadjusted pH, 22 ℃, atmospheric																				
	54.0	27.7	8.6	175.9	20.8	0.2	77.7	15.3	221.2	4.3	8.1	5.9	3.1	118.6	7.6	2.4	177.1	59.0	48.7	1.1
Experiment 9: solid:water ratio=1 g/L, unadjusted pH, 22 ℃, atmospheric, 10 g/L NaCl																				
	38.0	31.6	7.5	-	8.3	0.2	9.9	53.9	BDL	7.9	25.1	24.8	26.3	BDL	10.6	BDL	BDL	BDL	11.6	BDL
Experiment 10: solid:water ratio=1 g/L, pH 1.5, 22 ℃, atmospheric, 66 mM HCl																				
	95.4	91.5	30.9	16.7	47.4	2.6	18.3	45.6	BDL	80.2	9.1	72.1	68.9	BDL	53.5	45.5	57.9	BDL	52.3	28.6
Experiment 11: solid:water ratio=1 g/L, pH 4, 22 ℃, atmospheric, 1 mM citrate																				
	107.0	108.9	32.7	-	-	1.1	29.8	173.4	723.7	75.0	49.0	12.2	90.8	25.1	69.4	32.3	77.9	43.8	29.0	17.9
Experiment 12: solid:water ratio=1 g/L, pH 8, 22 ℃, atmospheric, 2.9 mM persulfate																				
	29.7	27.4	5.6	-	-	1.1	10.8	252.8	526.9	6.6	22.7	4.6	1.2	BDL	9.1	BDL	42.2	15.7	16.0	8.9
Experiment 13: solid:water ratio=1 g/L, pH 1.5, 80 ℃, atmospheric, 66 mM HCl, 1 mM citrate, 2.9 mM persulfate																				
	83.7	101.8	91.0	14.5	60.3	14.4	116.8	141.9	183.9	114.0	207.3	118.1	96.2	72.7	116.0	96.5	90.8	66.2	134.9	66.3

Data are shown as average of the duplicates. Some elements were not completely extracted from the acid digestion leading to percentages well above 100%.

“BDL” means the concentration at 120 hours were “below detection limit”.
“-” for Na indicates the use of NaOH on the autotitrator or the addition of NaCl, for K indicates excessive K due to pH monitoring over time on the autotitrator.
“*” indicates unreliable results due to the status of the analytical instrument.

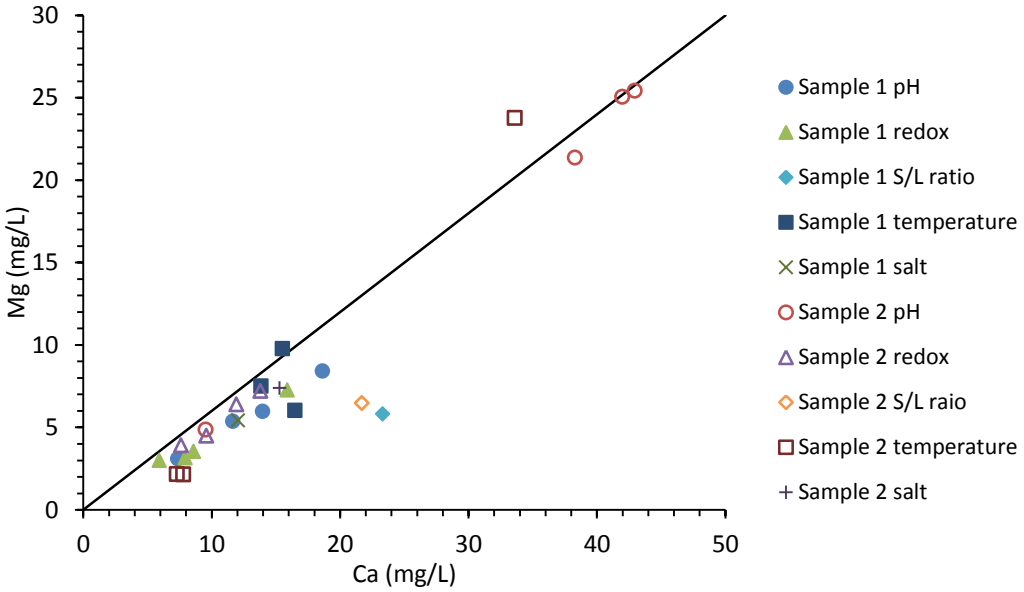

Figure S4.3 Relationship between the final Mg concentrations and the final Ca concentrations in all experiments with the two samples. The line represents the stoichiometric dissolution of Mg and Ca from dolomite.

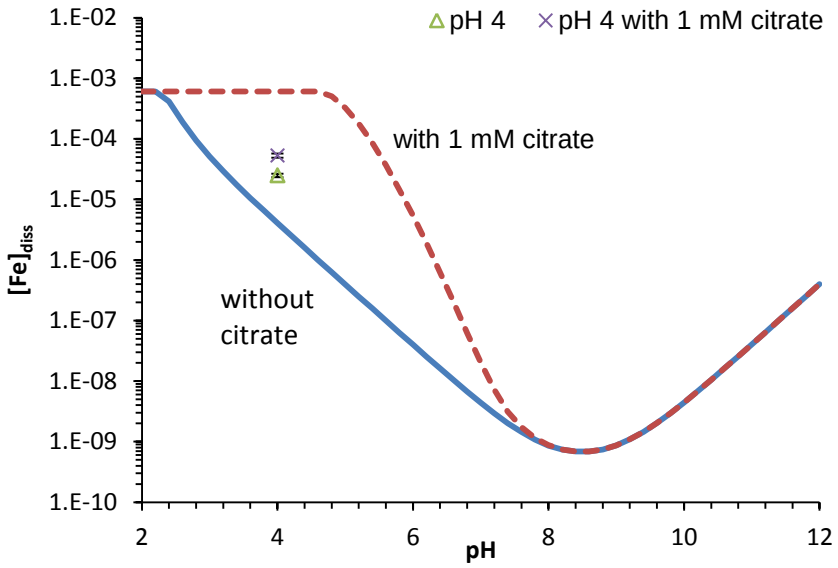

Figure S4.4 Fe(III) solubility prediction with and without citrate compared with experimental results. Lines are calculated Fe(III) solubility in equilibrium with $Fe(OH)_3$ in MINEQL+4.6 and the data points are measured Fe concentrations mobilized from Sample 1 in Experiments 1 and 11.

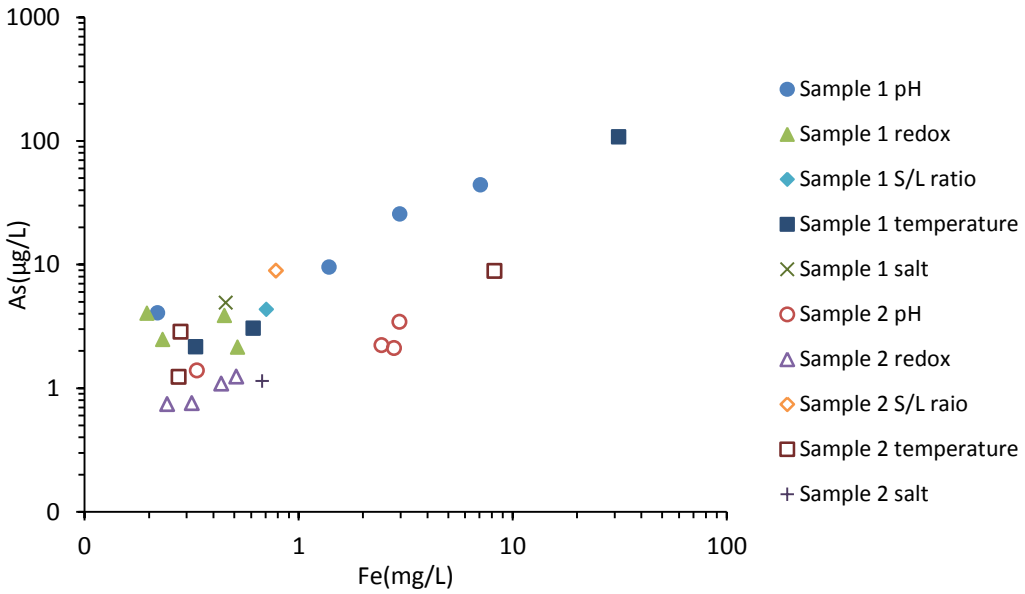

Figure S4.5 Relationship between the final As concentrations and the final Fe concentrations in all experiments with the two samples.

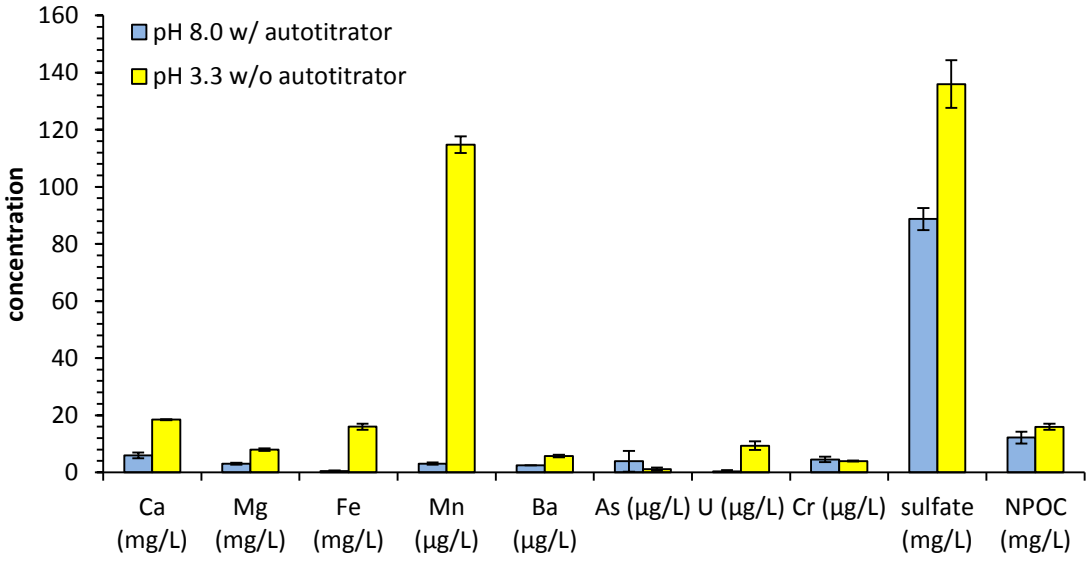

Figure S4.6 Metal, sulfate and NPOC mobilization from Sample 1 with 3% H_2O_2 after 120 hours of reaction. Experiments were performed at room temperature (22℃) with 1 g/L shale loadings. Data are shown as the average of the duplicates with error bars being the standard deviations. For the experiment without autotitrator, pH dropped to around 3.3 after 4 hours of reaction.

Calculations of redox potentials

Assume activity coefficients for all species are 1.

For H_2O_2

$\frac{1}{2}H_2O_2 + e^- \rightarrow OH^-$ $E_H°$= 1.8 V

At pH 8, $[OH^-]=10^{-6}$ M, $[H_2O_2]$=3 wt%=30 g/L=0.882 M

$$E_H = E_H^\circ - 0.059log\frac{\{OH^-\}}{\{H_2O_2\}^{1/2}} = 2.15\,V$$

For $S_2O_8^{2-}$

$\frac{1}{2}S_2O_8^{2-} + e^- \rightarrow SO_4^{2-}$ $E_H°$= 2.1 V

$[S_2O_8^{2-}]$=2.9 mM=2.9×10^{-3} M

For $[SO_4^{2-}]$ between 1 and 100 mg/L (10^{-5}-10^{-3} M), common values in our experiments

$$E_H = E_H^\circ - 0.059log\frac{\{SO_4^{2-}\}}{\{S_2O_8^{2-}\}^{1/2}} = 2.20 - 2.22\,V$$

Chapter 5: Conclusions and Recommendations for Future Work

5.1 Conclusions

5.1.1 Project 1 Conclusions

Project 1 in this thesis investigated the interfacial processes between arsenic and lepidocrocite, with a focus on adsorption and Fe(II)-mediated As(III) oxidation at the lepidocrocite surface. With both laboratory experiments and chemical reaction modeling tools, this project provided fundamental information about factors governing arsenic speciation, mobility and distribution in a system varied with regard to lepidocrocite, oxygen and Fe(II) presence. The key observations and conclusions from each subtask are described below.

Subtask 1A: Impact of water chemistry on arsenic adsorption to lepidocrocite

The adsorption of As(III) and As(V) to lepidocrocite strongly depends on water chemistry. For the arsenic concentrations and Fe loadings studied, As(V) adsorption decreases substantially with increasing pH, while As(III) adsorption is less sensitive to pH changes, characterized by a stable level of high adsorption between pH 6-9. As(III) and As(V) adsorption extents decreased in the presence of phosphate due to competitive adsorption (Appendix). For As(III), the presence of oxygen was able to promote the overall arsenic adsorption via partial As(III) oxidation, which is otherwise impossible under anoxic condition. A surface complexation model, optimized for both adsorption isotherms and adsorption edges, was able to describe the adsorption of both As(III) and As(V) to lepidocrocite over a broad range of conditions.

Subtask 1B: Fe(II)-mediated As(III) oxidation at lepidocrocite surface

The concentration and oxidation states of dissolved arsenic measured over the course of a reaction provided information on the rate and extent of As(III) oxidation. As(III) was not oxidized by the Fe(III) in lepidocrocite when dissolved oxygen and Fe(II) were not present. At both oxic and anoxic conditions, As(III) was oxidized to As(V) in systems that contained lepidocrocite together with Fe(II); this oxidation led to overall enhanced arsenic adsorption at near neutral pH. With oxygen the pH-dependent generation of oxidants from the Fenton reaction drove the As(III) oxidation. In the absence of oxygen the As(III) was probably oxidized by Fe(III) in lepidocrocite that had become more reactive upon reaction with Fe(II). These two reaction pathways could occur individually or in combination.

The findings from Project 1 are instrumental for understanding arsenic distribution and mobility in engineered water systems and are useful in manipulating the conditions under which arsenic is removed via adsorption. For example, in drinking water treatment plants where iron (oxyhydr)oxides are often used, the co-occurrence of aqueous Fe(II) and Fe(III) solids is beneficial for arsenic removal due to Fe(II)-induced As(III) oxidation to As(V) and thus altered adsorption behavior. The pH should be controlled carefully as both As(III) and As(V) adsorption to iron (oxyhydr)oxides are affected by pH. Above pH 8 As(V) may be more mobile than As(III); below pH 5 where Fenton chemistry generates hydroxyl radical, the presence of radical scavengers (such as carbonate, natural organic matters and other reducing agents) can compete with As(III) for the oxidants.

5.1.2 Project 2 Conclusions

Project 2 in this thesis investigated element release from shale materials exposed to various water chemistries and sought to identify the key chemical reaction pathways governing

release. The knowledge gained from this project will aid in understanding the factors controlling shale-bound element mobilization in geological formations similar to those examined in this thesis research.

Subtask 2A: Element mobilization from Eagle Ford samples

The Eagle Ford samples used in this study were rich in carbonates (calcite, dolomite and ankerite) and quartz with minor amounts of kaolinite, albite and pyrite. The organic carbon accounts for approximately 5 wt % of the samples, indicating their potential as a hydrocarbon source rock. The release of most elements strongly depended on pH, which was primarily controlled by carbonate dissolution. The introduction of oxygen and other oxidants (e.g. H_2O_2) significantly increased the amount of sulfate over time; the sulfate generated had a direct impact on Ba concentrations due to the formation of $BaSO_4$ as a secondary phase. For these Eagle Ford samples, the trace elements (As, U and Ba) mobilized from rock-fluid contact were low in concentration and will not likely affect the overall management strategies of the produced waters.

Subtasks 2B: Element mobilization from Bakken Formation samples

The main mineral phases in the Bakken Formation samples included quartz, K-feldspar, illite, dolomite and pyrite. In particular, one sample with total organic carbon as high as 18.7% was naturally enriched in trace elements (including some regulated ones such as As and U). Among all the water chemistry variables studied (pH, oxidant level, solid:water ratio, temperature and salinity), pH and the oxidant level were properties that most significantly affected element mobilization. The abundance of dolomite relative to pyrite, or acid-neutralizing mineral relative to sulfide minerals in general, largely determined the system pH when sufficient oxidant was present. The addition of chemical additives (HCl, citrate, and persulfate) affected

element release mainly by altering system pH or redox conditions. In the worst case scenario (with all three additives at 80 ℃), essentially all As and Cr available in the solids were mobilized into solution.

The degree to which the findings from Project 2 can be related to flowback from the Eagle Ford Formation and Bakken Formation will be affected by the parameters used in actual operations and subject to the complicated subsurface conditions. The solid:water ratio in the field will depend on the fracture network (10,000's to 100,000's g/L for overall porosities in the range of 1-10%), however, the rock-fluid interactions will occur at both fractured surfaces and the fluid-solid interfaces of particles mobilized from the formation, thus the total reactive surface area will be a more relevant property to scale up the extent of mobilization. In general, the system pH and redox conditions are the most important factors affecting shale-bound element release. The carbonate-rich formations (similar to the Eagle Ford samples) are more likely to have near neutral or even alkaline flowback even if the fluids injected are acidic. The carbonate-poor formations (similar to the Bakken Formation samples) may lead to flowback with low pH due to the lack of acid reactive (i.e. buffering) minerals to neutralize the acidity generated in oxidation reactions. The sulfide-rich formations (both Eagle Ford and Bakken Formation samples) might predict the precipitation of barite as a secondary phase and the subsequent scaling as a potential problem for well performance.

5.2 Recommendations for Future Work

5.2.1 Recommendations for Project 1

The information obtained from this research project provided insights on the chemical interactions between arsenic and lepidocrocite that could be used to control and manipulate the conditions in engineered water systems for better removal of arsenic. Recommended future work includes but is not limited to 1) analysis of arsenic speciation at the lepidocrocite mineral surface by techniques such as X-ray absorption spectroscopy, 2) *in situ* arsenic removal in an electrocoagulation reactor, and 3) arsenic adsorption to lepidocrocite in natural or synthetic groundwater.

In this thesis, the relative abundance of As(V) over As(III) on the solid phase was inferred based on dissolved arsenic speciation coupled with prediction from the surface complexation model. However, direct measurements of arsenic speciation on the lepidocrocite surface will provide precise information on the overall extent of As(III) oxidation throughout the course of reaction and allow for an more accurate evaluation on the role of Fe(II). Experimentally, efforts were made to evaluate a method that involved increasing suspension pH to desorb arsenic from the solid and removing As(V) in the filtrate via ionic exchange. However, the drastic change in pH in this process would lead to the dissolution of lepidocrocite and interfere with the effectiveness of the separation. Analytical methods that directly measure the oxidation states of arsenic on the solid surface, such as X-ray absorption near edge structure (XANES) or X-ray photoelectron spectroscopy (XPS) will be very helpful to extract results of the solid arsenic speciation as a function of time, and thus provide information about the kinetics of As(III) oxidation in the presence of Fe(II).

Previous studies have contradictory findings regarding arsenic speciation in anoxic mixed valent iron systems. While this thesis research among others (Amstaetter et al., 2010; Yan et al., 2012; Wang et al., 2014) has shown evidence of adsorbed As(III) oxidation in anoxic Fe(II)/Fe(III) (oxyhydr)oxide system, others have different observations. For example, Fe(II) has been found to significantly enhance As(V) adsorption but have no effect on As(III) adsorption onto anoxic aquifer sediment that contained goethite (Thi Hoa Mai et al., 2014), and another study has shown evidence that goethite alone (without Fe(II) or oxygen) can oxidize As(III) (Brown, 2010). Mössbauer spectra have qualitatively indicated that the newly formed goethite from electron transfer upon addition of Fe(II) is altered from the bulk goethite (Latta et al., 2012), but its role in As(III) oxidation is not yet clear. In the future, research that investigates the reaction between Fe(II) and Fe(III) (oxyhydr)oxides will be of great value to further explore the impact of iron cycling on the fate of redox sensitive trace elements.

Electrocoagulation is a convenient method for *in situ* water treatment, in particular for areas with better access to electricity than chemicals. Results from this thesis indicate the conditions for most efficient arsenic adsorption to lepidocrocite, which could be achieved in an electrocoagulation reactor by controlling the operation parameters (such as current, pH, water flow rate). The experiments of *in situ* removal of arsenic in an electrocoagulation reactor will provide information on how the batch experiment results can be related to the real treatment practices. The conclusions regarding arsenic adsorption to and redox interactions with lepidocrocite from this thesis will also aid the understanding about the chemical reactions involved in an electrocoagulation process.

Finally, it will be worthwhile to evaluate the effectiveness of arsenic adsorption to lepidocrocite (or other iron oxyhydroxides in general) with some natural or synthetic

groundwater samples, either using a batch reactor or an electrocoagulation reactor. Compared to the well-controlled system prepared in a lab, the constituents other than arsenic in natural groundwater will complicate the overall process via competitive adsorption, redox reaction or altering the interfacial properties of the lepidocrocite. It will be very helpful to investigate the strategy to manipulate the water chemistry and minimize the interference from the constituents readily available in natural waters (such as NOMs).

5.2.2 Recommendations for Project 2

This research project advanced our understanding about element mobilization from shales during rock-fluid interactions and the fluid properties dominating these reactions. The knowledge gained could be helpful in designing hydraulic fracturing fluids for sustainable energy extraction and optimizing water management options for waste streams that might contain regulated elements leached from shale formations. Recommended future work includes but is not limited to 1) evaluating element mobilization from fractured rock samples, 2) simulating rock-fluid interaction in porous and fractured media with reactive transport modeling and 3) analyzing related field samples for trace element concentrations in actual flowback waters.

First, this thesis research focused on the rate and extent of element mobilization rather than transport effects by designing experiments with a low solid:water ratio and a high surface area exposed to fluids. However, the actual shale-fluid interactions in hydraulically fractured zones are most likely to occur at the surfaces on both the fractured formation and mobilized rock particles. Experiments with fractured rock will advance our understanding in the role that transport effects might play in element release from the shales, and further relate the laboratory observations to the actual field sites.

While bench-scale experiments could provide key and rich information on reaction pathways, it is virtually impossible to test all relevant solid samples and fluid compositions experimentally. In this case, reactive transport modeling could serve as a powerful tool for the analysis of coupled physical and chemical processes. It can describe the interactions of competing processes at a range of spatial and time scales. The models couple the equations for chemical equilibrium and kinetics with advective and diffusive transport processes to predict the evolution of chemical concentrations and speciation in both time and space. It has been employed to simulate multi-component reactions in fractured media and flow and reaction in heterogeneous porous media (Steefel et al., 2005). Reactive transport modeling can be applied to the hydraulically fractured areas that are characterized by a fracture surface and porous zones.

Finally, the analysis of flowback and produced water from hydraulically fractured zones with regard to their trace element concentrations will give the most direct measure about how important the trace elements might be in affecting the wastewater management options. While current research has focused on issues including high TDS, bromide, and iodide associated with produced waters, this thesis research shows that some regulated elements could be completely leached out in conditions relevant to hydraulic fracturing fluids. It will thus be very helpful to obtain first-hand information on the trace element concentrations at actual field sites and assess the potential risks associated with regulated elements.

References

American Public Health Association (1998). 4500-P Phosphorus. Standard Methods for the Examination of Water and Wastewater. Washington DC.

Amstaetter, K., Borch, T., Larese-Casanova, P. and Kappler, A. (2010). "Redox Transformation of Arsenic by Fe(II)-Activated Goethite (α-FeOOH) " Environmental science & technology **44**(1): 102-108.

Antelo, J., Avena, M., Fiol, S., López, R. and Arce, F. (2005). "Effects of pH and ionic strength on the adsorption of phosphate and arsenate at the goethite–water interface." Journal of colloid and interface science **285**(2): 476-486.

Arai, Y. and Sparks, D. (2001). "ATR–FTIR spectroscopic investigation on phosphate adsorption mechanisms at the ferrihydrite–water interface." Journal of Colloid and Interface Science **241**(2): 317-326.

Arthur, J., Bohm, B., Coughlin, B. J., Layne, M. and Cornue, D. (2009). Evaluating the environmental implications of hydraulic fracturing in shale gas reservoirs. SPE Americas E&P Environmental and Safety Conference.

Arthur, J. D., Bohm, B. and Layne, M. (2008). Hydraulic fracturing considerations for natural gas wells of the Marcellus Shale. Groundwater Protection Council Annual Forum. Cincinnati.

Atkinson, R. J., Parfitt, R. L. and Smart, R. S. C. (1974). "Infra-red study of phosphate adsorption on goethite." Journal of the Chemical Society, Faraday Transactions 1: Physical Chemistry in Condensed Phases **70**(0): 1472-1479.

Balasubramanian, N., Kojima, T., Basha, C. A. and Srinivasakannan, C. (2009). "Removal of arsenic from aqueous solution using electrocoagulation." Journal of hazardous materials **167**(1): 966-969.

Barbot, E., Vidic, N. S., Gregory, K. B. and Vidic, R. D. (2013). "Spatial and Temporal Correlation of Water Quality Parameters of Produced Waters from Devonian-Age Shale following Hydraulic Fracturing." Environmental Science & Technology **47**(6): 2562-2569.

Benko, K. L. and Drewes, J. E. (2008). "Produced water in the Western United States: geographical distribution, occurrence, and composition." Environmental Engineering Science **25**(2): 239-246.

Berg, M., Tran, H. C., Nguyen, T. C., Pham, H. V., Schertenleib, R. and Giger, W. (2001). "Arsenic contamination of groundwater and drinking water in Vietnam: a human health threat." Environmental science & technology **35**(13): 2621-2626.

Bhandari, N., Reeder, R. J. and Strongin, D. R. (2011). "Photoinduced Oxidation of Arsenite to Arsenate on Ferrihydrite." Environmental science & technology **45**(7): 2783-2789.

Bhandari, N., Reeder, R. J. and Strongin, D. R. (2012). "Photoinduced Oxidation of Arsenite to Arsenate in the Presence of Goethite." Environmental science & technology **46**(15): 8044-8051.

Bisceglia, K. J., Rader, K. J., Carbonaro, R. F., Farley, K. J., Mahony, J. D. and Di Toro, D. M. (2005). "Iron(II)-Catalyzed Oxidation of Arsenic(III) in a Sediment Column." Environmental science & technology **39**(23): 9217-9222.

Block, P. A., Brown, R. A. and Robinson, D. (2004). Novel activation technologies for sodium persulfate in situ chemical oxidation. Proceedings of the Fourth International Conference on the remediation of chlorinated and recalcitrant compounds.

Blondes, M. S., Gans, K. D., Thordsen, J. J., Reidy, M. E., Thomas, B., Engle, M. A., Kharaka, Y. K. and Rowan, E. L. (2014). U.S. Geological Survey National Produced Waters Geochemical Database v2.1 (PROVISIONAL), USGS.

Brown, A. M. (2010). Arsenic Speciation in the Presence of Anoxic Mixed Valent Iron Systems. Master of Science, University of Iowa.

Brunauer, C., Emmett, P. and Teller, E. (1938). "Adsorption of gases in multimolecular layers." Journal of the American Chemical Society **60**: 309-319.

Busenberg, E. and Plummer, L. N. (1982). "The kinetics of dissolution of dolomite in CO_2-H_2O systems at 1.5 to 65 degrees C and O to 1 atm P_{CO2}." American Journal of Science **282**(1): 45-78.

Buxton, G. V., Greenstock, C. L., Helman, W. P. and Ross, A. B. (1988). "Critical review of rate constants for reactions of hydrated electrons, hydrogen atoms and hydroxyl radicals." Phys.Chem.Ref.Data **17**: 513-886.

Chapman, E. C., Capo, R. C., Stewart, B. W., Kirby, C. S., Hammack, R. W., Schroeder, K. T. and Edenborn, H. M. (2012). "Geochemical and Strontium Isotope Characterization of Produced Waters from Marcellus Shale Natural Gas Extraction." Environmental Science & Technology **46**(6): 3545-3553.

Chermak, J. A. and Schreiber, M. E. (2013). "Mineralogy and Trace Element Geochemistry of Gas Shales in the United States: Environmental Implications." International Journal of Coal Geology **126**: 32-44.

Chowdhury, U. K., Biswas, B. K., Chowdhury, T. R., Samanta, G., Mandal, B. K., Basu, G. C., Chanda, C. R., Lodh, D., Saha, K. C. and Mukherjee, S. K. (2000). "Groundwater arsenic contamination in Bangladesh and West Bengal, India." Environmental health perspectives **108**(5): 393.

Cluff, M. A., Hartsock, A., MacRae, J. D., Carter, K. and Mouser, P. J. (2014). "Temporal Changes in Microbial Ecology and Geochemistry in Produced Water from Hydraulically Fractured Marcellus Shale Gas Wells." Environmental Science & Technology **48**(11): 6508-6517.

Cornell, R. M. and Schwertmann, U. (2003). The iron oxides: structure, properties, reactions, occurrences and uses, Wiley-vch.

Crittenden, J. C., Trussell, R. R., Hand, D. W., Howe, K. J. and Tchobanoglous, G. (2012). Removal of Selected Constituents. MWH's Water Treatment: Principles and Design. Hoboken, NJ, USA, John Wiley & Sons, Inc.

Davis, J. A. and Kent, D. B. (1990). "Surface complexation modeling in aqueous geochemistry." Reviews in Mineralogy and Geochemistry **23**(1): 177-260.

Dixit, S. and Hering, J. G. (2003). "Comparison of Arsenic(V) and Arsenic(III) Sorption onto Iron Oxide Minerals: Implications for Arsenic Mobility." Environmental science & technology **37**(18): 4182-4189.

Dzombak, D. A. (1990). Surface complexation modeling: hydrous ferric oxide, John Wiley & Sons.

Ely, W. J. (1985). Stimulation Treatment Handbook: An Engineer's Guide to Quality Control. Tulsa, OK, USA, PennWell Corporation.

Farquhar, M. L., Charnock, J. M., Livens, F. R. and Vaughan, D. J. (2002). "Mechanisms of Arsenic Uptake from Aqueous Solution by Interaction with Goethite, Lepidocrocite, Mackinawite, and Pyrite: An X-ray Absorption Spectroscopy Study." Environmental science & technology **36**(8): 1757-1762.

Fendorf, S., Michael, H. A. and van Geen, A. (2010). "Spatial and temporal variations of groundwater arsenic in South and Southeast Asia." Science **328**(5982): 1123-1127.

Ferguson, J. F. and Gavis, J. (1972). "A review of the arsenic cycle in natural waters." Water research **6**(11): 1259-1274.

Ferrar, K. J., Michanowicz, D. R., Christen, C. L., Mulcahy, N., Malone, S. L. and Sharma, R. K. (2013). "Assessment of Effluent Contaminants from Three Facilities Discharging Marcellus Shale Wastewater to Surface Waters in Pennsylvania." Environmental Science & Technology **47**(7): 3472-3481.

Ficklin, W. H. (1983). "Separation of arsenic (III) and arsenic (V) in ground waters by ion-exchange." Talanta **30**(5): 371-373.

Field, T. B., McCourt, J. L. and McBryde, W. (1974). "Composition and stability of iron and copper citrate complexes in aqueous solution." Canadian Journal of Chemistry **52**(17): 3119-3124.

Fields, K., Chen, A. S. C., Wang, L., Sorg, T. J., Cincinnati, O. H. and Columbus, O. H. (2000). Arsenic removal from drinking water by iron removal plants, US Environmental Protection Agency, Office of Research and Development.

Fontenot, B. E., Hunt, L. R., Hildenbrand, Z. L., Carlton Jr, D. D., Oka, H., Walton, J. L., Hopkins, D., Osorio, A., Bjorndal, B., Hu, Q. H. and Schug, K. A. (2013). "An Evaluation of Water Quality in Private Drinking Water Wells Near Natural Gas

Extraction Sites in the Barnett Shale Formation." Environmental Science & Technology **47**(17): 10032-10040.

FracFocus 2.0. "FracFocus Chemical Disclosure Registry." Retrieved 09/02, 2014, from http://fracfocus.org/chemical-use/what-chemicals-are-used.

Fukushi, K. and Sverjensky, D. A. (2007). "A predictive model (ETLM) for arsenate adsorption and surface speciation on oxides consistent with spectroscopic and theoretical molecular evidence." Geochimica et Cosmochimica Acta **71**(15): 3717-3745.

Gao, Y. and Mucci, A. (2001). "Acid base reactions, phosphate and arsenate complexation, and their competitive adsorption at the surface of goethite in 0.7 M NaCl solution." Geochimica et Cosmochimica Acta **65**(14): 2361-2378.

Gomes, J. A. G., Daida, P., Kesmez, M., Weir, M., Moreno, H., Parga, J. R., Irwin, G., McWhinney, H., Grady, T. and Peterson, E. (2007). "Arsenic removal by electrocoagulation using combined Al–Fe electrode system and characterization of products." Journal of hazardous materials **139**(2): 220-231.

Gregory, K. B., Vidic, R. D. and Dzombak, D. A. (2011). "Water management challenges associated with the production of shale gas by hydraulic fracturing." Elements **7**(3): 181-186.

GWPC, ALL, NETL and U.S. DOE (2009). Modern shale gas development in the United States: A primer, Office of Fossil Energy and National Energy Technology Laboratory, United States Department of Energy.

Hagemeier, P. and Hutt, J. (2009). "Hydraulic fracturing, water use issues under congressional, public scrutiny." Oil & Gas Journal **107**(25): 18-+.

Haluszczak, L. O., Rose, A. W. and Kump, L. R. (2013). "Geochemical evaluation of flowback brine from Marcellus gas wells in Pennsylvania, USA." Applied Geochemistry **28**(0): 55-61.

Hamm, R. E., Johnson, R. L., Perkins, R. H. and Davis, R. E. (1958). "Complex Ions of Chromium. VIII. Mechanism of Reaction of Organic Acid Anions with Chromium (III) 1, 2." Journal of the american chemical society **80**(17): 4469-4471.

Han, B., Runnells, T., Zimbron, J. and Wickramasinghe, R. (2002). "Arsenic removal from drinking water by flocculation and microfiltration." Desalination **145**(1): 293-298.

Handler, R. M., Beard, B. L., Johnson, C. M. and Scherer, M. M. (2009). "Atom exchange between aqueous Fe (II) and goethite: An Fe isotope tracer study." Environmental science & technology **43**(4): 1102-1107.

Harbor, R. L. (2011). Facies Characterization and Stratigraphic Architecture of Organic-Rich Mudrocks, Upper Cretaceous Eagle Ford Formation, South Texas. Master of Science, University of Texas at Austin.

Harvey, C. F., Ashfaque, K. N., Yu, W., Badruzzaman, A. B. M., Ali, M. A., Oates, P. M., Michael, H. A., Neumann, R. B., Beckie, R. and Islam, S. (2006). "Groundwater dynamics and arsenic contamination in Bangladesh." Chemical Geology **228**(1): 112-136.

Hayes, T. (2009). Sampling and Analysis of Water Streams Associated with the Development of the Marcellus Shale Gas. Marcellus Shale Initiative Publications Database. Des Plaines, IL, Gas Technology Institute.

He, C., Li, M., Liu, W., Barbot, E. and Vidic, R. (2014). "Kinetics and Equilibrium of Barium and Strontium Sulfate Formation in Marcellus Shale Flowback Water." Journal of Environmental Engineering **140**(5): B4014001.

He, S. and Morse, J. W. (1993). "The carbonic acid system and calcite solubility in aqueous Na-K-Ca-Mg-Cl-SO4 solutions from 0 to 90 ℃." Geochimica et Cosmochimica Acta **57**(15): 3533-3554.

Hering, J. G., Chen, P.-Y., Wilkie, J. A. and Elimelech, M. (1997). "Arsenic removal from drinking water during coagulation." Journal of Environmental Engineering **123**(8): 800-807.

Hiemstra, T. and van Riemsdijk, W. H. (2007). "Adsorption and surface oxidation of Fe (II) on metal (hydr) oxides." Geochimica et Cosmochimica Acta **71**(24): 5913-5933.

Hoover, T. E. and Berkshire, D. C. (1969). "Effects of hydration on carbon dioxide exchange across an air-water interface." Journal of Geophysical Research **74**(2): 456-464.

Huang, C. P., O'Melia, C. R. and Morgan, J. J. (1995). Aquatic chemistry: interfacial and interspecies processes, An American Chemical Society Publication.

Hug, S. J. and Leupin, O. (2003). "Iron-Catalyzed Oxidation of Arsenic(III) by Oxygen and by Hydrogen Peroxide: pH-Dependent Formation of Oxidants in the Fenton Reaction." Environmental science & technology **37**(12): 2734-2742.

Izumi, Y., Masih, D., Aika, K.-i. and Seida, Y. (2005). "Characterization of Intercalated Iron(III) Nanoparticles and Oxidative Adsorption of Arsenite on Them Monitored by X-ray Absorption Fine Structure Combined with Fluorescence Spectrometry." The Journal of Physical Chemistry B **109**(8): 3227-3232.

Jain, A. and Loeppert, R. H. (2000). "Effect of competing anions on the adsorption of arsenate and arsenite by ferrihydrite." Journal of environmental quality **29**(5): 1422-1430.

Jain, C. and Singh, R. (2012). "Technological options for the removal of arsenic with special reference to South East Asia." Journal of environmental management **107**: 1-18.

Jain, C. K. and Ali, I. (2000). "Arsenic: occurrence, toxicity and speciation techniques." Water research **34**(17): 4304-4312.

Jekel, M. R. (1994). Removal of arsenic in drinking water treatment. New York, JOHN WILEY & SONS LTD.

Johnson, D. L. (1971). "Simultaneous determination of arsenate and phosphate in natural waters." Environmental Science & Technology **5**(5): 411-414.

Jönsson, J. and Sherman, D. M. (2008). "Sorption of As(III) and As(V) to siderite, green rust (fougerite) and magnetite: Implications for arsenic release in anoxic groundwaters." Chemical Geology **255**(1–2): 173-181.

Kanematsu, M., Young, T. M., Fukushi, K., Green, P. G. and Darby, J. L. (2013). "Arsenic(III, V) adsorption on a goethite-based adsorbent in the presence of major co-existing ions: Modeling competitive adsorption consistent with spectroscopic and molecular evidence." Geochimica et Cosmochimica Acta **106**(0): 404-428.

Katsoyiannis, I. A., Ruettimann, T. and Hug, S. J. (2008). "pH dependence of fenton reagent generation and As (III) oxidation and removal by corrosion of zero valent iron in aerated water." Environmental science & technology **42**(19): 7424-7430.

Kearns, T. J. (2012). Chemostratigraphy of the Eagle Ford formation. Master of Science, University of Texas at Arlington.

Kim, K.-W., Chanpiwat, P., Hanh, H. T., Phan, K. and Sthiannopkao, S. (2011). "Arsenic geochemistry of groundwater in Southeast Asia." Frontiers of medicine **5**(4): 420-433.

Kimball, R. (2012). Key Considerations for the Frac Flowback/Produced Water Reuse and Treatment. NJWEA Annual Conference. Atlantic City, NJ, USA.

King, G. E. (2012). Hydraulic Fracturing 101: What Every Representative, Environmentalist, Regulator, Reporter, Investor, University Researcher, Neighbor and Engineer Should Know About Estimating Frac Risk and Improving Frac Performance in Unconventional Gas and Oil Wells. SPE Hydraulic Fracturing Technology Conference. The Woodlands, Texas, USA, Society of Petroleum Engineers.

Kinniburgh, D. G. and Smedley, P. L. (2001). Arsenic contamination of groundwater in Bangladesh, British Geological Survey.

Kirk, M. F., Martini, A. M., Breecker, D. O., Colman, D. R., Takacs-Vesbach, C. and Petsch, S. T. (2012). "Impact of commercial natural gas production on geochemistry and microbiology in a shale-gas reservoir." Chemical Geology **332–333**(0): 15-25.

Kolthoff, I. and Miller, I. (1951). "The chemistry of persulfate. I. The kinetics and mechanism of the decomposition of the persulfate ion in aqueous medium1." Journal of the American Chemical Society **73**(7): 3055-3059.

Kondash, A. J., Warner, N. R., Lahav, O. and Vengosh, A. (2013). "Radium and Barium Removal through Blending Hydraulic Fracturing Fluids with Acid Mine Drainage." Environmental Science & Technology **48**(2): 1334-1342.

Kourgiantakis, M., Matzapetakis, M., Raptopoulou, C., Terzis, A. and Salifoglou, A. (2000). "Lead–citrate chemistry. Synthesis, spectroscopic and structural studies of a novel lead (II)–citrate aqueous complex." Inorganica Chimica Acta **297**(1): 134-138.

Kuhn, P., Di Primio, R. and Horsfield, B. (2010). Bulk composition and phase behaviour of petroleum sourced by the Bakken Formation of the Williston Basin. Geological Society, London, Petroleum Geology Conference series, Geological Society of London.

Kuuskraa, V., Stevens, S., Leeuwen, T. V. and Moodhe, K. (2011). World shale gas resources: an initial assessment of 14 regions outside the United States, US Department of Energy.

Lakshmanan, D., Clifford, D. A. and Samanta, G. (2009). "Ferrous and ferric ion generation during iron electrocoagulation." Environmental science & technology **43**(10): 3853-3859.

Lakshmanan, D., Clifford, D. A. and Samanta, G. (2010). "Comparative study of arsenic removal by iron using electrocoagulation and chemical coagulation." Water research **44**(19): 5641-5652.

Larese-Casanova, P. and Scherer, M. M. (2007). "Fe (II) sorption on hematite: New insights based on spectroscopic measurements." Environmental science & technology **41**(2): 471-477.

Latta, D. E., Bachman, J. E. and Scherer, M. M. (2012). "Fe Electron Transfer and Atom Exchange in Goethite: Influence of Al-Substitution and Anion Sorption." Environmental Science & Technology **46**(19): 10614-10623.

Li, L., van Genuchten, C. M., Addy, S. E. A., Yao, J., Gao, N. and Gadgil, A. J. (2012). "Modeling As(III) Oxidation and Removal with Iron Electrocoagulation in Groundwater." Environmental science & technology **46**(21): 12038-12045.

Madsen, I. C., Scarlett, N. V., Cranswick, L. M. and Lwin, T. (2001). "Outcomes of the International Union of Crystallography Commission on powder diffraction round robin on quantitative phase analysis: samples 1a to 1h." Journal of Applied Crystallography **34**(4): 409-426.

Manning, B. A., Fendorf, S. E. and Goldberg, S. (1998). "Surface structures and stability of arsenic (III) on goethite: spectroscopic evidence for inner-sphere complexes." Environmental Science & Technology **32**(16): 2383-2388.

Manning, B. A. and Goldberg, S. (1996). "Modeling Competitive Adsorption of Arsenate with Phosphate and Molybdate on Oxide Minerals." Soil Sci. Soc. Am. J. **60**(1): 121-131.

Manning, B. A., Hunt, M. L., Amrhein, C. and Yarmoff, J. A. (2002). "Arsenic(III) and Arsenic(V) Reactions with Zerovalent Iron Corrosion Products." Environmental science & technology **36**(24): 5455-5461.

Mba, K. and Prasad, M. (2010). Mineralogy and its contribution to anisotropy and kerogen stiffness variations with maturity in the Bakken shales. 2010 SEG Annual Meeting, Denver, CO, Society of Exploration Geophysicists.

Mohan, D. and Pittman, C. U. (2007). "Arsenic removal from water/wastewater using adsorbents—a critical review." Journal of hazardous materials **142**(1): 1-53.

Moniz, E. J., Jacoby, H. D., Meggs, A. J. M., Armtrong, R. C., Cohn, D. R., Deutch, J. M., Kaufman, G. M., Kenderdine, M. A., O'Sullivan, F., Paltsev, S., Parsons, J. E., Perez-Arrizga, I., Reilly, J. M., Seto, C., Webster, M. D., Yang, Y., Mcrae, G. S. and Ruppel, C. (2010). The future of natural gas: an interdisciplinary MIT study. Cambridge, MA, MIT Energy Initiative.

Montgomery, C. (2013). Fracturing Fluid Components. Effective and Sustainable Hydraulic Fracturing. A. Bunger, J. McLennan and R. Jeffrey, InTech.

Mullen, J. (2010). Petrophysical characterization of the Eagle Ford Shale in south Texas. Canadian Unconventional Resources and International Petroleum Conference. Calgary, Alberta, Canada, Curran Associates, Inc.

Murali Mohan, A., Hartsock, A., Bibby, K. J., Hammack, R. W., Vidic, R. D. and Gregory, K. B. (2013). "Microbial Community Changes in Hydraulic Fracturing Fluids and Produced

Water from Shale Gas Extraction." Environmental Science & Technology **47**(22): 13141-13150.

Nandy, D., Sonnenberg, S. and Humphrey, J. D. (2014). Application of Inorganic Geochemical Studies for Characterization of Bakken Shales, Williston Basin, North Dakota and Montana. Unconventional Resources Technology Conference (URTeC). Denver, Colorado, USA.

Nanzyo, M. and Watanabe, Y. (1982). "Diffuse reflectance infra red spectra and ion-adsorption properties of the phosphate surface complex on goethite." Soil Science and Plant Nutrition **28**(3): 359-368.

Neumann, A., Kaegi, R., Voegelin, A., Hussam, A., Munir, A. K. and Hug, S. J. (2013). "Arsenic removal with composite iron matrix filters in Bangladesh: a field and laboratory study." Environmental science & technology **47**(9): 4544-4554.

Nicot, J.-P. and Scanlon, B. R. (2012). "Water use for shale-gas production in Texas, US." Environmental science & technology **46**(6): 3580-3586.

Nicot, J.-P., Scanlon, B. R., Reedy, R. C. and Costley, R. A. (2014). "Source and Fate of Hydraulic Fracturing Water in the Barnett Shale: A Historical Perspective." Environmental Science & Technology **48**(4): 2464-2471.

Nordstrom, D. K., Plummer, L. N., Langmuir, D., Busenberg, E., May, H. M., Jones, B. F. and Parkhurst, D. L. (1990). "Revised chemical equilibrium data for major water-mineral reactions and their limitations." Chemical modeling of aqueous systems II **416**: 398-413.

Olesen, N. L. (2010). Bakken Oil Resource Play –Williston Basin (US) - Overview and Historical Perspective. New Perspectives on Shales. Norman, OK, Oklahoma Geological Survey.

Olmstead, S. M., Muehlenbachs, L. A., Shih, J.-S., Chu, Z. and Krupnick, A. J. (2013). "Shale gas development impacts on surface water quality in Pennsylvania." Proceedings of the National Academy of Sciences **110**(13): 4962-4967.

Ona-Nguema, G., Morin, G., Juillot, F., Calas, G. and Brown, G. E. (2005). "EXAFS Analysis of Arsenite Adsorption onto Two-Line Ferrihydrite, Hematite, Goethite, and Lepidocrocite." Environmental science & technology **39**(23): 9147-9155.

Ona-Nguema, G., Morin, G., Wang, Y., Foster, A. L., Juillot, F., Calas, G. and Brown, G. E. (2010). "XANES Evidence for Rapid Arsenic(III) Oxidation at Magnetite and Ferrihydrite Surfaces by Dissolved O2 via Fe2+-Mediated Reactions." Environmental science & technology **44**(14): 5416-5422.

Parfitt, R. L., Atkinson, R. J. and Smart, R. S. C. (1975). "The Mechanism of Phosphate Fixation by Iron Oxides." Soil Sci. Soc. Am. J. **39**(5): 837-841.

Parfitt, R. L., Russell, J. D. and Farmer, V. C. (1976). "Confirmation of the surface structures of goethite ([small alpha]-FeOOH) and phosphated goethite by infrared spectroscopy." Journal of the Chemical Society, Faraday Transactions 1: Physical Chemistry in Condensed Phases **72**(0): 1082-1087.

Parga, J. R., Cocke, D. L., Valenzuela, J. L., Gomes, J. A., Kesmez, M., Irwin, G., Moreno, H. and Weir, M. (2005). "Arsenic removal via electrocoagulation from heavy metal contaminated groundwater in La Comarca Lagunera Mexico." Journal of hazardous materials **124**(1): 247-254.

Pasilis, S. P. and Pemberton, J. E. (2003). "Speciation and coordination chemistry of uranyl (VI)-citrate complexes in aqueous solution." Inorganic chemistry **42**(21): 6793-6800.

Peacock, C. L. and Sherman, D. M. (2004). "Copper (II) sorption onto goethite, hematite and lepidocrocite: a surface complexation model based on ab initio molecular geometries and EXAFS spectroscopy." Geochimica et Cosmochimica Acta **68**(12): 2623-2637.

Pedersen, H. D., Postma, D. and Jakobsen, R. (2006). "Release of arsenic associated with the reduction and transformation of iron oxides." Geochimica et Cosmochimica Acta **70**(16): 4116-4129.

Pedersen, H. D., Postma, D., Jakobsen, R. and Larsen, O. (2005). "Fast transformation of iron oxyhydroxides by the catalytic action of aqueous Fe (II)." Geochimica et Cosmochimica Acta **69**(16): 3967-3977.

Pettijohn, F. J. (1975). Sedimentary Rocks. New York, NY, Harper & Row, Publishers, Inc.

Plummer, L. N. and Busenberg, E. (1982). "The solubilities of calcite, aragonite and vaterite in CO2-H2O solutions between 0 and 90 ℃, and an evaluation of the aqueous model for the system CaCO3-CO2-H2O." Geochimica et Cosmochimica Acta **46**(6): 1011-1040.

Pokrovsky, O. S., Golubev, S. V. and Schott, J. (2005). "Dissolution kinetics of calcite, dolomite and magnesite at 25 °C and 0 to 50 atm p_{CO2}." Chemical Geology **217**(3): 239-255.

Pokrovsky, O. S. and Schott, J. (2001). "Kinetics and mechanism of dolomite dissolution in neutral to alkaline solutions revisited." American Journal of Science **301**(7): 597-626.

Pokrovsky, O. S., Schott, J. and Thomas, F. (1999). "Dolomite surface speciation and reactivity in aquatic systems." Geochimica et Cosmochimica Acta **63**(19): 3133-3143.

Rai, D., Eary, L. and Zachara, J. (1989). "Environmental chemistry of chromium." Science of the total environment **86**(1): 15-23.

Ratna Kumar, P., Chaudhari, S., Khilar, K. C. and Mahajan, S. P. (2004). "Removal of arsenic from water by electrocoagulation." Chemosphere **55**(9): 1245-1252.

Reeder, R. J. (1983). "Crystal chemistry of the rhombohedral carbonates." Reviews in Mineralogy and Geochemistry **11**(1): 1-47.

Remucal, C. K. and Sedlak, D. L. (2011). "The role of iron coordination in the production of reactive oxidants from ferrous iron oxidation by oxygen and hydrogen peroxide." Aquatic redox chemistry **1071**: 177-197.

Sahai, N., Lee, Y. J., Xu, H., Ciardelli, M. and Gaillard, J. F. (2007). "Role of Fe (II) and phosphate in arsenic uptake by coprecipitation." Geochimica et Cosmochimica Acta **71**(13): 3193-3210.

Sarg, J. F. (2012). The Bakken - An Unconventional Petroleum and Reservoir System, United States Department of Energy, National Energy Technology Laboratory.

Scanlon, B. R., Reedy, R. C. and Nicot, J. P. (2014). "Comparison of Water Use for Hydraulic Fracturing for Unconventional Oil and Gas versus Conventional Oil." Environmental Science & Technology **48**(20): 12386-12393.

Schecher, W. and McAvoy, D. (2007). MINEQL+ 4.6. Environmental Research Software. Hallowell, ME.

Schmidt, K. K. (2008). "What Is Hydraulic Fracturing?" Retrieved 02-06, 2015, from http://www.propublica.org/about/frequently-asked-questions/.

Sherman, D. M. and Randall, S. R. (2003). "Surface complexation of arsenic(V) to iron(III) (hydr)oxides: structural mechanism from ab initio molecular geometries and EXAFS spectroscopy." Geochimica et Cosmochimica Acta **67**(22): 4223-4230.

Smedley, P. L. and Kinniburgh, D. G. (2002). "A review of the source, behaviour and distribution of arsenic in natural waters." Applied Geochemistry **17**(5): 517-568.

Sondhi, N. (2011). Petrophysical Characterization of Eagle Ford Shale. Master of Science, University of Oklahoma.

Stephen, D. J., Shockey, R. E., Kurz, B. A., Kalenze, N. S., Cowan, R. M., Ziman, J. J. and Harju, J. A. (2010). Bakken Water Opportunities Assessment - Phase 1. Grand Forks, ND, Energy & Environmental Research Center, University if North Dakota.

Stookey, L. L. (1970). "Ferrozine---a new spectrophotometric reagent for iron." Analytical Chemistry **42**(7): 779-781.

Sverjensky, D. A. (2003). "Standard states for the activities of mineral surface sites and species." Geochimica et Cosmochimica Acta **67**(1): 17-28.

Taylor, S. R. (1964). "Abundance of chemical elements in the continental crust: a new table." Geochimica et Cosmochimica Acta **28**(8): 1273-1285.

Tchobanoglous, G. and Schroeder, E. (1985). Water quality: characteristics, modeling, modification, Prentice Hall.

Thella, K., Verma, B., Srivastava, V. C. and Srivastava, K. K. (2008). "Electrocoagulation study for the removal of arsenic and chromium from aqueous solution." Journal of Environmental Science and Health Part A **43**(5): 554-562.

Thi Hoa Mai, N., Postma, D., Thi Kim Trang, P., Jessen, S., Hung Viet, P. and Larsen, F. (2014). "Adsorption and desorption of arsenic to aquifer sediment on the Red River floodplain at Nam Du, Vietnam." Geochimica et Cosmochimica Acta **142**(0): 587-600.

Tverberg, G. (2008). "The Bakken Formation: How Much Will It Help?" Retrieved 02-19, 2015, from http://www.theoildrum.com/node/3868.

U.S. EIA (2011). Review of emerging resources: US Shale gas and shale oil plays. Government. US Energy Information Administration. http://205.254. **135**.

U.S. EIA (2013). Annual Energy Outlook 2013, AEO 2013 Early Release Overview. Department of Energy, Washington DC.

U.S. EIA (2013). Technically Recoverable Shale Oil and Shale Gas Resources: An Assessment of 137 Shale Formations in 41 Countries Outside the United States. Washington DC, US Department of Energy.

U.S. EIA (2014). Annual Energy Outlook 2014 with Projections to 2040. US Energy Information Administration, Department of Energy. Washington DC, US Energy Information Administration, Department of Energy.

U.S. EIA (2014). June 2014 Monthly Energy Review. Washington DC.

U.S. EIA (2014). U.S. Crude Oil and Natural Gas Proved Reserves, 2012. Washington DC.

U.S. EPA (2004). Evaluation of Impacts to Underground Sources of Drinking Water by Hydraulic Fracturing of Coalbed Methane Reservoirs. Washington DC.

U.S. EPA (2009). National Primary Drinking Water Regulations.

U.S. EPA. (2010). "Toxicity Profiles, Ecological Risk Assessment." Retrieved 09-08, 2014, from http://web.archive.org/web/20100110125521/http://www.epa.gov/region5/superfund/ecology/html/toxprofiles.htm.

U.S. EPA (2011). Proceedings of the Technical Workshops for the Hydraulic Fracture Study: Chemical and Analytical Methods Washington DC.

U.S. HHS (2003). Toxicological Profile for Uranium. Atlanta, GA, Agency for Toxic Substances and Disease Registry (ATSDR).

USGS (2013). Assessment of Undiscovered Oil Resources in the Bakken and Three Forks Formations, Williston Basin Province, Montana, North Dakota, and South Dakota, 2013. USGS Fact Sheet.

van Genuchten, C. M., Addy, S. E. A., Peña, J. and Gadgil, A. J. (2012). "Removing Arsenic from Synthetic Groundwater with Iron Electrocoagulation: An Fe and As K-Edge EXAFS Study." Environmental science & technology **46**(2): 986-994.

Vengosh, A., Jackson, R. B., Warner, N., Darrah, T. H. and Kondash, A. (2014). "A Critical Review of the Risks to Water Resources from Unconventional Shale Gas Development and Hydraulic Fracturing in the United States." Environmental Science & Technology **48**(15): 8334-8348.

Vidic, R., Brantley, S., Vandenbossche, J., Yoxtheimer, D. and Abad, J. (2013). "Impact of Shale Gas Development on Regional Water Quality." Science **340**(6134).

Villalobos, M., Cheney, M. A. and Alcaraz-Cienfuegos, J. (2009). "Goethite surface reactivity: II. A microscopic site-density model that describes its surface area-normalized variability." Journal of colloid and interface science **336**(2): 412-422.

Wan, W., Pepping, T. J., Banerji, T., Chaudhari, S. and Giammar, D. E. (2011). "Effects of water chemistry on arsenic removal from drinking water by electrocoagulation." Water research **45**(1): 384-392.

Wang, L., Fortner, J. D. and Giammar, D. E. (2014). "Impact of Water Chemistry on Element Mobilization from Eagle Ford Shale." Environmental Engineering Science **[online early access]**.

Wang, X.-Q., Liu, C.-P., Yuan, Y. and Li, F.-b. (2014). "Arsenite oxidation and removal driven by a bio-electro-Fenton process under neutral pH conditions." Journal of Hazardous Materials **275**: 200-209.

Warner, N. R., Christie, C. A., Jackson, R. B. and Vengosh, A. (2013). "Impacts of Shale Gas Wastewater Disposal on Water Quality in Western Pennsylvania." Environmental Science & Technology **47**(20): 11849-11857.

Waxman, H. A., Markey, E. J. and DeGette, D. (2011). Chemicals used in hydraulic fracturing. Minority Staff. Washington D.C., United States House of Representatives Committee on Energy and Commerce.

Wenk, C. B., Kaegi, R. and Hug, S. J. (2014). "Factors affecting arsenic and uranium removal with zero-valent iron: laboratory tests with Kanchan-type iron nail filter columns with different groundwaters." Environmental Chemistry **11**(5): 547-557.

WHO (2011). Guidelines for drinking-water quality. Geneva.

Wickramasinghe, S. R., Han, B., Zimbron, J., Shen, Z. and Karim, M. N. (2004). "Arsenic removal by coagulation and filtration: comparison of groundwaters from the United States and Bangladesh." Desalination **169**(3): 231-244.

Wilkie, J. A. and Hering, J. G. (1996). "Adsorption of arsenic onto hydrous ferric oxide: effects of adsorbate/adsorbent ratios and co-occurring solutes." Colloids and Surfaces A: Physicochemical and Engineering Aspects **107**: 97-110.

Wilkie, J. A. and Hering, J. G. (1998). "Rapid oxidation of geothermal arsenic (III) in streamwaters of the eastern Sierra Nevada." Environmental science & technology **32**(5): 657-662.

Wilson, J. M. and Van Briesen, J. M. (2013). "Source Water Changes and Energy Extraction Activities in the Monongahela River, 2009–2012." Environmental Science & Technology **47**(21): 12575-12582.

Wilson, J. M. and VanBriesen, J. M. (2012). "Oil and Gas Produced Water Management and Surface Drinking Water Sources in Pennsylvania." Environmental Practice **14**(04): 288-300.

Wu, W.-M., Carley, J., Luo, J., Ginder-Vogel, M. A., Cardenas, E., Leigh, M. B., Hwang, C., Kelly, S. D., Ruan, C., Wu, L., Van Nostrand, J., Gentry, T., Lowe, K., Carroll, S., Luo, W., Fields, M. W., Gu, B., Watson, D., Kemner, K. M., Marsh, T., Tiedje, J., Zhou, J., Fendorf, S., Kitanidis, P. K., Jardine, P. M. and Criddle, C. S. (2007). "In Situ Bioreduction of Uranium (VI) to Submicromolar Levels and Reoxidation by Dissolved Oxygen." Environmental Science & Technology **41**(16): 5716-5723.

Yan, W., Ramos, M. A. V., Koel, B. E. and Zhang, W.-x. (2012). "As(III) Sequestration by Iron Nanoparticles: Study of Solid-Phase Redox Transformations with X-ray Photoelectron Spectroscopy." The Journal of Physical Chemistry C **116**(9): 5303-5311.

Zeng, H., Arashiro, M. and Giammar, D. E. (2008). "Effects of water chemistry and flow rate on arsenate removal by adsorption to an iron oxide-based sorbent." Water research **42**(18): 4629-4636.

Zeng, H., Fisher, B. and Giammar, D. E. (2007). "Individual and competitive adsorption of arsenate and phosphate to a high-surface-area iron oxide-based sorbent." Environmental science & technology **42**(1): 147-152.

Zhao, Z., Jia, Y., Xu, L. and Zhao, S. (2011). "Adsorption and heterogeneous oxidation of As(III) on ferrihydrite." Water research **45**(19): 6496-6504.

Appendix A: Competitive Adsorption of Arsenic and Phosphate

The batch experiment setup and procedures that were used to investigate the competitive adsorption of arsenic and phosphate were the same as described in Chapter 2 for arsenic-only adsorption experiments. Arsenic and phosphate were added to the reactors simultaneously to initiate the experiments. For As(V), a total As concentration of 1.33 μM (100 μg/L) and a total concentration of 0.03 mM (1 mg/L) or 0.13 mM (4 mg/L) phosphate-P were used with 79 mg/L lepidocrocite. Reactors were equilibrated for 24 h with a background electrolyte of 1 mM $NaHCO_3$. Experiments with As(III) were performed in a glove box filled with N_2/H_2 circulated over heated Pd catalyst. A total As concentration of 6.67 μM (500 μg/L) and a total concentration of 0.13 mM (4 mg/L) or 0.32 mM (10 mg/L) phosphate-P were used with 190 mg/L lepidocrocite. A reaction time of 48 h and a background electrolyte of 0.01 M $NaNO_3$were adopted. The pH was monitored throughout the course of reaction with adjustment by 0.1 M NaOH and 0.1 M HNO_3. The reactors for both As(V) and As(III) adsorption with phosphate were closed to keep constant dissolved inorganic carbon. Dissolved arsenic was analyzed by ICP-MS and phosphate was measured by the ascorbic acid method (Johnson, 1971; American Public Health Association, 1998).

The presence of 0.03-0.13 mM (1-4 mg/L) PO_4^{3-}-P inhibited As(V) adsorption (Figure A.1). The extent of decrease was most significant at pH 7-9. At pH 8, all 1.33 μM (100 μg/L) As(V) was bound to lepidocrocite; the addition of 0.03 mM (1 mg/L) PO_4^{3-}-P decreased As(V) adsorption by more than 60%, and 0.13 mM (4 mg/L) PO_4^{3-}-P decreased As(V) adsorption by nearly 90%.

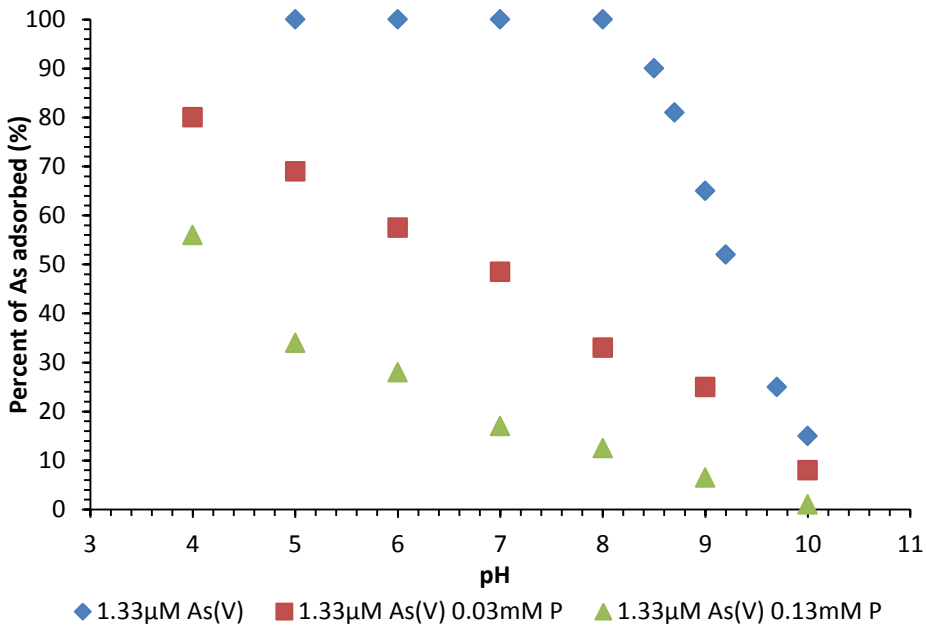

Figure A.1 As(V) adsorption on lepidocrocite as a function of pH with total As(V) concentration of 1.33 µM, with and without phosphate.

The fraction of As(III) adsorbed to lepidocrocite was also reduced substantially in the presence of phosphate (Figure A.2). This competitive effect of phosphate was more evident at pH below 8 than above. With 0.13 mM (4 mg/L) PO_4^{3-}P, As(III) adsorption was decreased by 30-40% at pH 4-8 and less than 20% at pH 8-10. The increase of phosphate concentration to 0.32 mM (10 mg/L) PO_4^{3-}P further reduced As(III) adsorption, but to a much lesser extent.

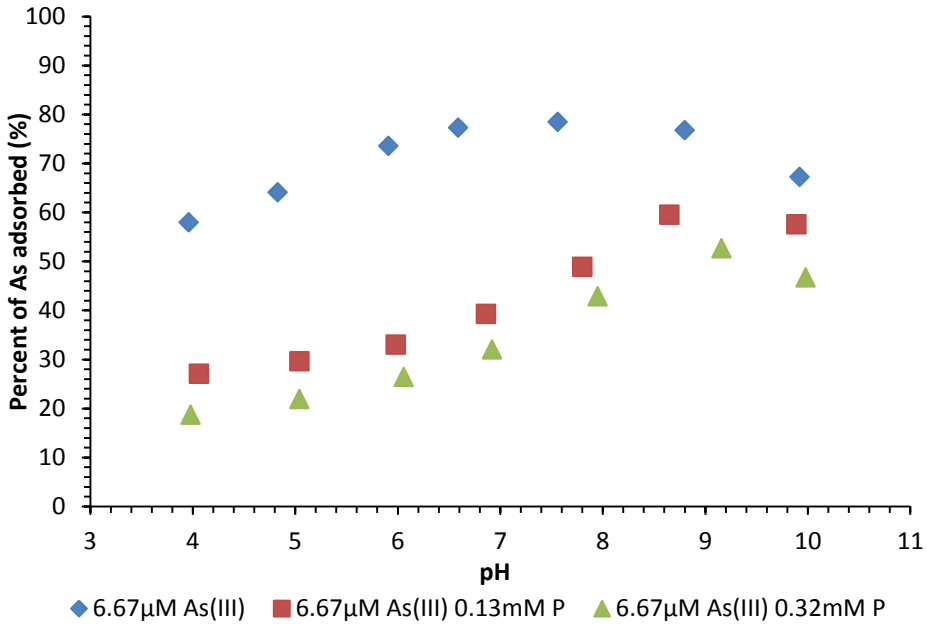

Figure A.2 As(III) adsorption on lepidocrocite as a function of pH with total As(III) concentration of 6.77 µM, with and without phosphate.

Phosphate adsorbs strongly onto iron oxide minerals and can therefore compete with arsenic for surface sites (Jain and Loeppert, 2000; Gao and Mucci, 2001; Dixit and Hering, 2003; Kanematsu et al., 2013). The overall inhibitory effect of phosphate on arsenic adsorption is weaker for lepidocrocite than other iron (oxyhydr)oxides, such as 2-line ferrihydrite and goethite at comparable arsenic to phosphate ratios (Jain and Loeppert, 2000; Dixit and Hering, 2003).

Adsorption of phosphate onto lepidocrocite also decreased with increasing pH (Figure A.3). Previous studies have suggested that phosphate primarily forms bidentate binuclear surface complexes on ferrihydrite, goethite, lepidocrocite, and hematite surfaces (Atkinson et al., 1974; Parfitt et al., 1975; Parfitt et al., 1976; Nanzyo and Watanabe, 1982; Arai and Sparks, 2001). Phosphate is usually postulated to form the same surface complexes with As(V) due to their similar chemical structure and analogous adsorption properties (Manning and Goldberg, 1996; Jain and Loeppert, 2000; Sverjensky, 2003; Kanematsu et al., 2013). Consequently the presence

of As(V) had little influence on phosphate adsorption (Figure A.3a) at the high phosphate-to-arsenic molar ratios (30 and 100) used in this study. However, As(III) had a strong inhibitory effect on phosphate adsorption at phosphate-to-arsenic ratios of 50 and 100 (Figure A.3b). This suggests that even a small amount of As(III) could alter the lepidocrocite surface properties with regard to phosphate association. This effect has not been observed for the other iron (oxyhydr)oxides.

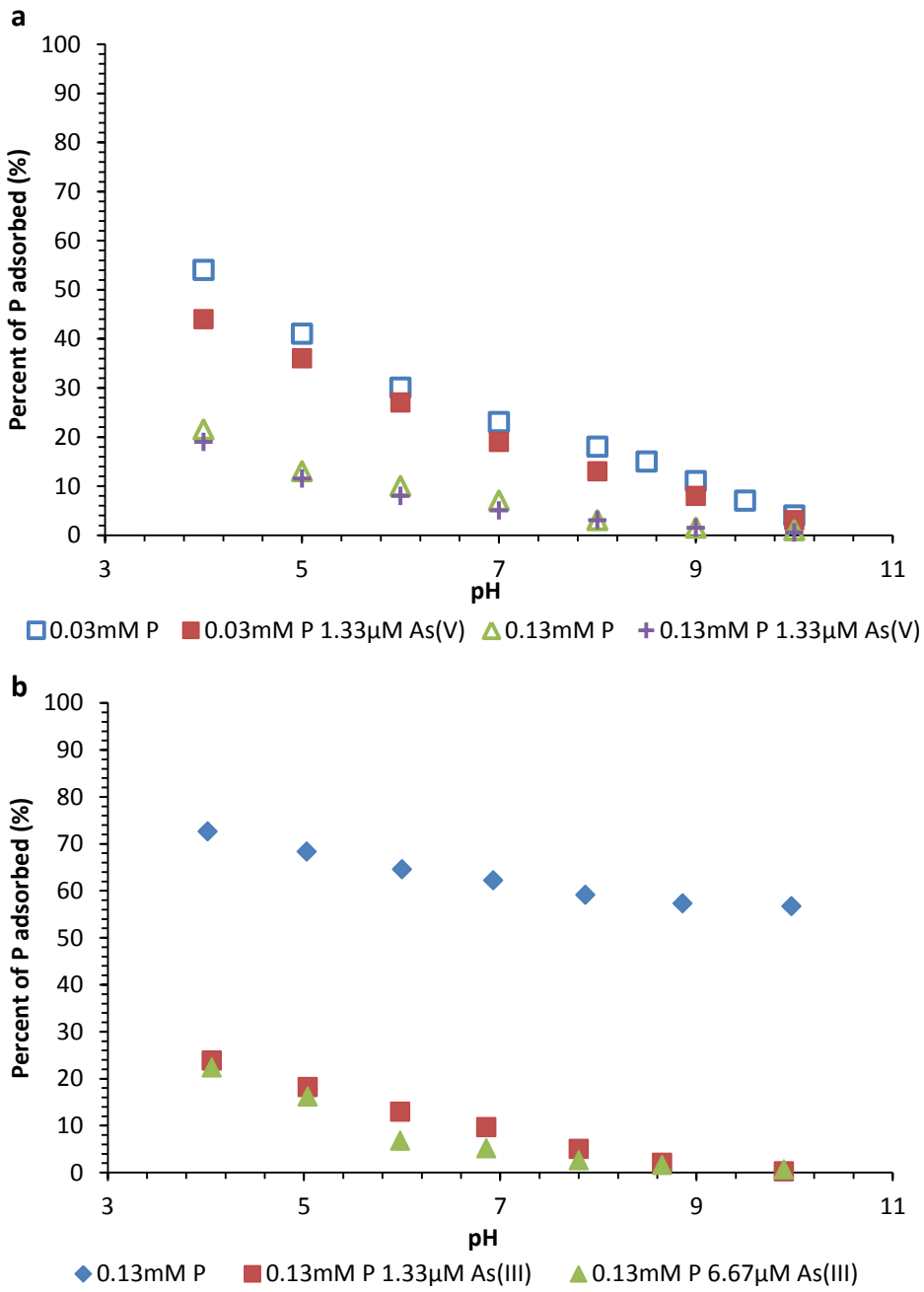

Figure A.3 Phosphate adsorption on lepidocrocite as a function of pH (a) with and without As(V) and (b) with and without As(III). The lepidocrocite concentrations were 79 mg/L in (a) and 190 mg/L in (b).

Appendix B: Effect of 2-Propanol on Lepidocrocite Colloidal Stability

In Chapter 2, 2-propanol was added to the adsorption experiments as a radical scavenger. The overall arsenic adsorption to lepidocrocite was higher with 15 mM 2-propanol than that without, in the presence or absence of the direct addition of 90 μM ferrous ion. An additional experiment was performed to probe the effect of 2-propanol on the lepidocrocite colloidal stability.

B.1 Experiment

The experiment was initiated by preparation of four portions of 50 mL120 mg Fe/L (190 mg γ-FeOOH/L) suspension with a background electrolyte of 0.01 M $NaNO_3$. The suspensions were contained in 50 mL plastic digestion tubes and stirred continuously at 300 rpm. Two of the reactors (Samples c and d) were spiked with 60 μL of 2-propanol to reach a concentration of 15 mM while the other two (Samples a and b) were not. After 48 hours, the suspension was sampled and diluted 20 times for size distribution analysis with a dynamic light scattering (DLS) system (Zetasizer Nano ZS (ZEN3600), Malvern Instruments). For DLS analysis, each of the four samples was measured ten times in a single run. The concentrations of lepidocrocite (120 mg Fe/L) and 2-propanol (15 mM), ionic strength (0.01 M), stirring speed (300 rpm) and reaction time (48 h) were identical to those used in the equilibrium As(III) adsorption experiments described in Chapter 2. After sampling for DLS measurement, the suspensions were left stirring for another ten days for qualitative observations.

B.2 Results

B.2.1 DLS Analysis

The addition of 2-propanol had somewhat an inhibitive effect on the aggregation of lepidocrocite colloids (Figures B.1-B.3). This effect was more evident in particle size distribution by intensity (Figure B.1) and volume (Figure B.3) than that by number (Figure B.2). The average particle size for all four samples was in the range of 500 – 700 nm. Based on the size distribution by intensity and volume, two or three (Samples a and b) out of ten measurements on particles without 2-propanol exhibited a peak at particles size above 1000 nm, indicating the formation of large aggregates. With 2-propanol, there was no large aggregation formation throughout the ten measurements for Sample c, and two out of the ten measurements for Sample d showed an additional peak at particle size below 150 nm. The lower frequency of aggregation formation observed for lepidocrocite particles with 2-propanol may suggest a larger surface area and thus enhanced arsenic adsorption.

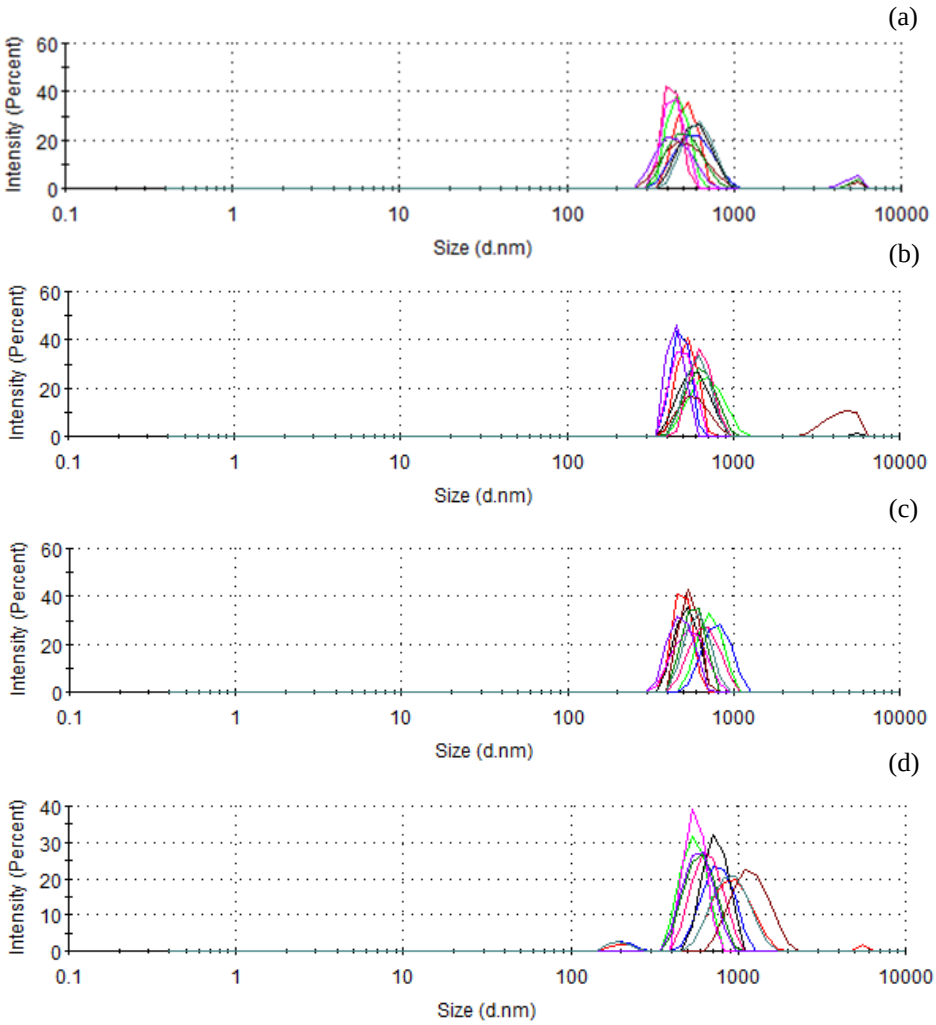

Figure B.1 Lepidocrocite particle size distribution by intensity: (a) and (b) without 2-propanol; (c) and (d) with 15 mM 2-propanol.

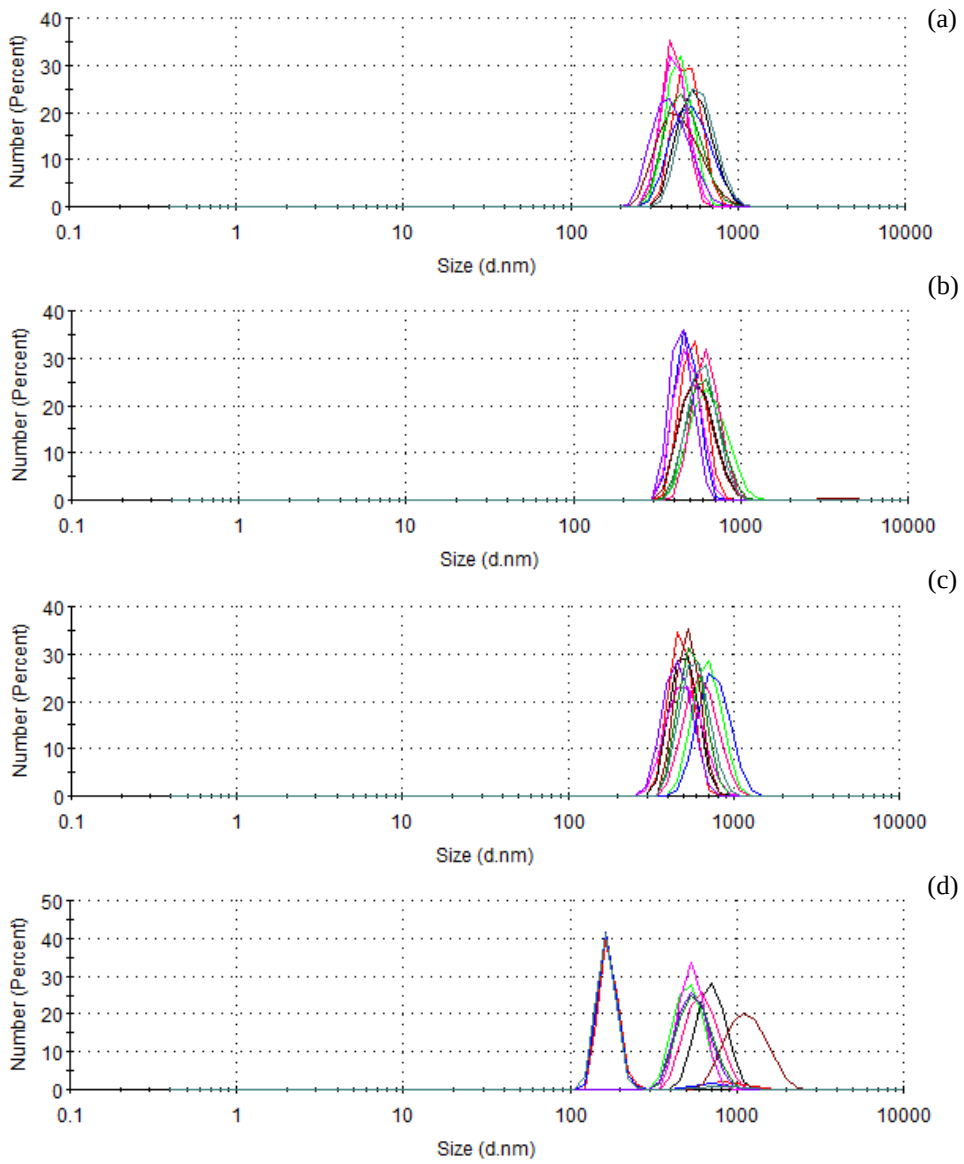

Figure B.2 Lepidocrocite particle size distribution by number: (a) and (b) without 2-propanol; (c) and (d) with 15 mM 2-propanol.

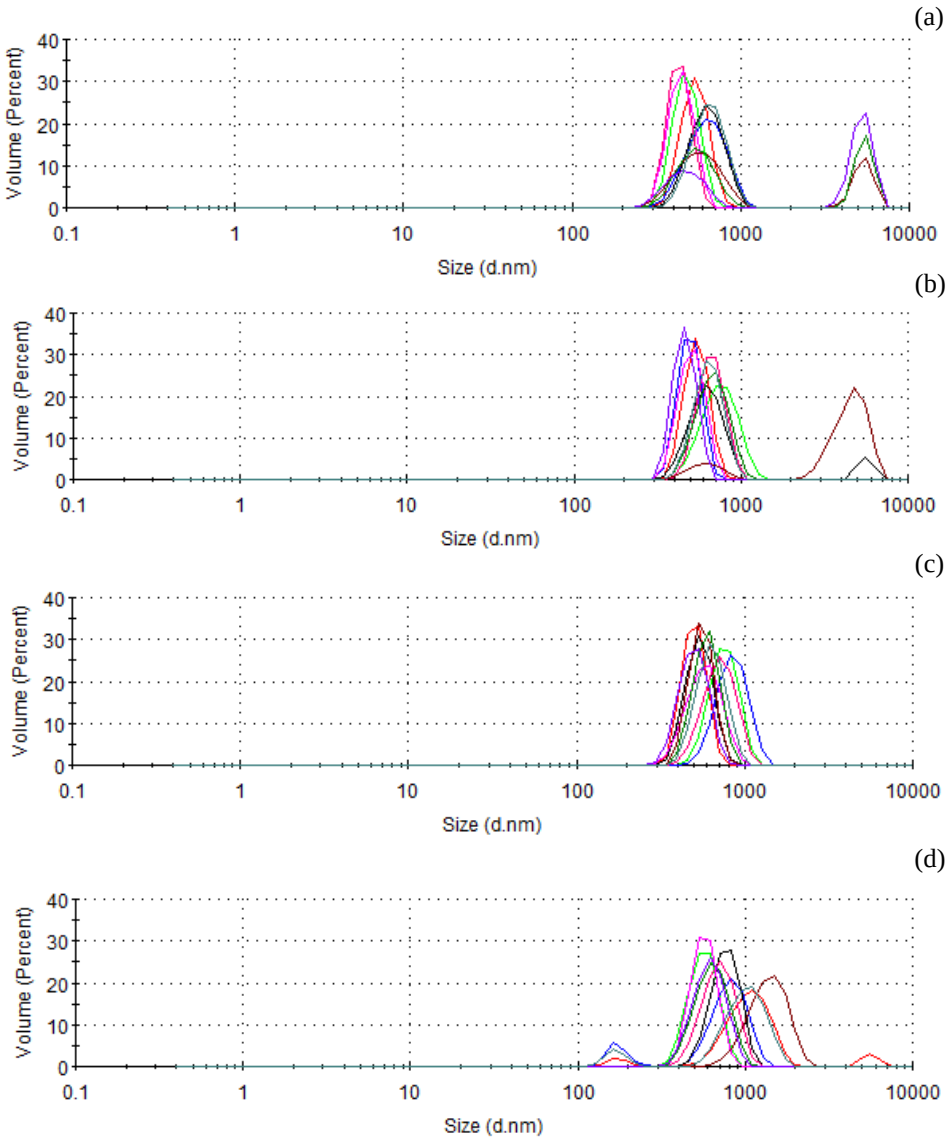

Figure B.3 Lepidocrocite particle size distribution by volume: (a) and (b) without 2-propanol; (c) and (d) with 15 mM 2-propanol.

B.2.2 Qualitative Comparison

After 10 days reaction, particle aggregation was observed to form at the air-water interface for lepidocrocite suspension without 2-propanol (Reactors a and b in Figure B.4). The type of aggregation was absent for experiments with 2-propanol addition (Reactors c and d in Figure B.4). The formation of lepidocrocite aggregation at the air-water interface without 2-

propanol is only visible to the naked eye after one week, however, this is clear indication that 2-propanol increased the stability of lepidocrocite colloids, which could probably account for the enhanced arsenic adsorption onto the solids.

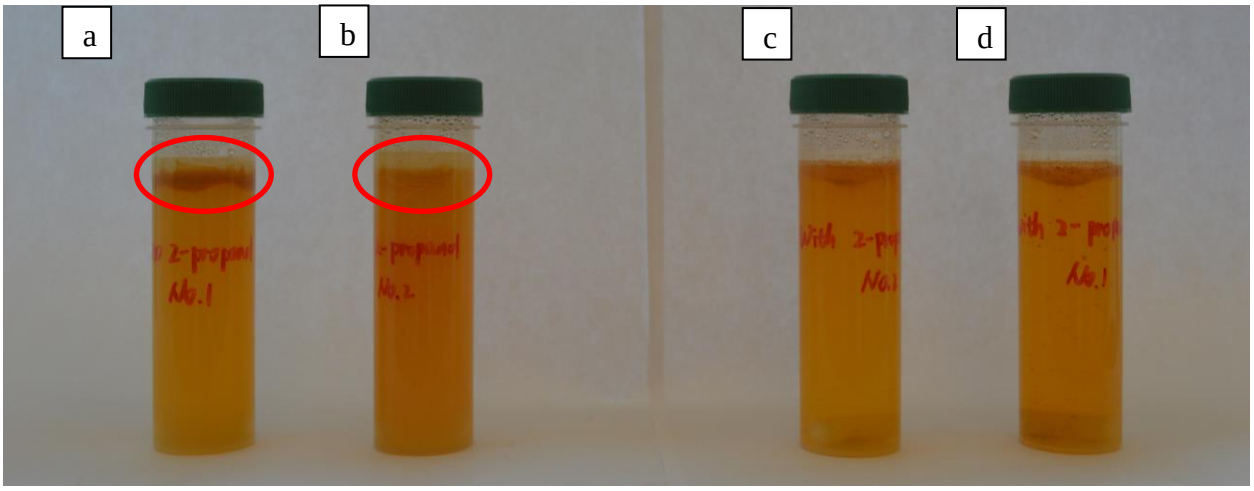

Figure B.4 Images of the four reactors after 10 days of experiments: (a) and (b) without 2-propanol; (c) and (d) with 15 mM 2-propanol. The ovals show where the large aggregates are forming in Reactor (a) and (b).